

TURBULENCE-INDUCED RELATIVE VELOCITY OF DUST PARTICLES I: IDENTICAL PARTICLES

LIUBIN PAN

Harvard-Smithsonian Center for Astrophysics, 60 Garden St., Cambridge, MA 02138; lpan@cfa.harvard.edu

AND

PAOLO PADOAN

ICREA & ICC, University of Barcelona, Martí i Franquès 1, E-08028 Barcelona, Spain; ppadoan@icc.ub.edu

Draft version May 3, 2013

ABSTRACT

We study the relative velocity of inertial particles suspended in turbulent flows and discuss implications of our results for dust particle collisions in protoplanetary disks. We carry out a 512^3 simulation of a weakly compressible turbulent flow, evolving 14 species of particles with friction timescale, τ_p , covering the entire scale range of the flow. The Stokes number, St , of the smallest particles is $\simeq 0.1$, where St is the ratio of τ_p to the Kolmogorov timescale, while the largest particles have $\tau_p \simeq 54T_L$, where T_L is the Lagrangian correlation timescale of the simulated flow. A comparison with the results of the simulation shows that the theoretical model by Pan & Padoan (hereafter PP10) gives satisfactory predictions for the rms relative velocity between identical particles. The model reveals an insightful physical picture. It shows that the relative velocity of two same-size particles is determined by the particle memory of the flow velocity difference along their trajectories, and hence has a crucial dependence on the particle pair separation backward in time. Using the simulation data, we compute the collision kernel accounting for the effect of turbulent clustering. The collision kernel per unit cross section shows an abrupt rise as St increases toward $\simeq 1$, which may be viewed as an activation process corresponding the rapid formation of caustics. At $St \gtrsim 1$, the collision kernel first increases slightly, reaches a maximum at $\tau_p \simeq 2T_L$, and finally decreases as $\tau_p^{-1/2}$ for $\tau_p \gg T_L$. Coagulation models of dust particle growth in protoplanetary disks should account for the new features of the collision kernel found in this study. Furthermore, we show that the probability distribution function (PDF) of the particle relative velocity is highly non-Gaussian, exhibiting extremely fat tails. Using the physical picture of PP10, we identify two sources of non-Gaussianity: the imprint of the turbulent flow intermittency and an intrinsic contribution from the particle dynamics. The shape of the PDF is fattest for particles with $St \simeq 1$. The PDF tails for particles with $\tau_p \simeq 1 - 2T_L$ are well described by a $4/3$ stretched exponential function, consistent with a prediction based on the physical picture of PP10. The PDF approaches Gaussian only in the extreme large-particle limit with $\tau_p \gtrsim 54T_L$. The high non-Gaussianity in the relative velocity is expected to have important implications for the growth and evolution of dust particles in protoplanetary disks, as it determines the fractions of collisions leading to sticking, bouncing or fragmentation.

1. INTRODUCTION

The dynamics of particles of finite inertia suspended in turbulent flows is a fundamental problem with applications ranging from industrial processes (e.g. spray combustion engines) to geophysical flows (e.g., atmospheric clouds). The interaction between turbulence and particles has been studied to understand rain initiation in warm terrestrial clouds (e.g., Pinsky & Khain 1997; Falkovich, Fouxon, & Stepanov 2002; Shaw 2003), cloud evolution in the atmospheres of planets, cool stars and brown dwarfs (e.g., Rossow 1978; Pruppacher & Klett 1997; Freytag et al. 2010; Helling et al. 2011), collisions and growth of dust particles in protoplanetary disks (e.g., Dullemond & Dominik 2005; Zsom et al. 2010, 2011; Birnstiel et al. 2011) and in the interstellar medium (e.g., Ormel et al. 2009).

The evolution of the particle size depends on the particle collision rate which may be significantly enhanced by turbulent motions in the carrier flow, as illustrated by recent numerical and theoretical advances in this field (e.g., Wang et al. 2000; Zhou et al. 2001; Falkovich et al. 2002; Zaichik & Alipchenkov 2003, 2009; Zaichik et

al. 2003, 2006; Wilkinson et al. 2005, 2006; Falkovich & Pumir 2007; Gustavsson & Mehlig 2011; Gustavsson et al. 2012). It is now understood that an accurate evaluation of the collision rates requires the modeling of two enhancement mechanisms: the preferential concentration or clustering of inertial particles (e.g., Maxey 1987 and Squires & Eaton 1991) and the turbulence-induced collision velocity. In this work, we will focus on the statistics of turbulence-induced relative velocities, and briefly discuss the contribution to the collision rate by turbulent clustering (see Pan et al. 2011 for a detailed discussion of turbulent clustering in the context of planetesimal formation). We restrict our discussion to the collision velocity between same-size particles, usually referred to as the monodisperse case, and will address the general bidisperse case (collisions between particles of different sizes) in a follow-up paper.

The main motivation of our study is to improve the modeling of the evolution of dust particles in protoplanetary disks, which sets the stage for the formation of planetesimals, the likely precursors to fully-fledged planets. For example, the planetesimal formation model

by Johansen et al. (2007, 2009, 2011) requires particle growth up to decimeter to meter size, in order to achieve good frictional coupling to the disk rotation and hence the maximum clustering effect by the streaming instability. Cuzzi et al. (2008, 2010) and Chambers (2010) proposed an alternative model of planetesimal formation based on the strong turbulent clustering of chondrule-size particles. Other studies (e.g. Lee et al. 2010) focus on the possibility that small particles settle to the disk midplane, where gravitational instability can result in planetesimal formation (e.g. Goldreich & Ward 1973; Youdin 2011), despite the turbulence stirring caused by the Kelvin-Helmholtz instability induced by the vertical settling of the particles (e.g. Weidenschilling 1980; Chiang 2008).

The evolution of the size distribution of dust particles is controlled by collisions. Small particles tend to stick together when colliding, and thus their size grows by coagulation. As the size increases, the particles become less sticky (Blum & Wurm 2010), and, depending on the collision velocity, the collisions may result in bouncing or fragmentation. A detailed summary of experimental results for the dependence of the collision outcome on the particle properties (such as the particle size and porosity) and on the collision velocity can be found in Guttler et al. (2010). The coagulation, bouncing and fragmentation processes may lead to a quasi-equilibrium distribution of particle sizes (e.g., Birnstiel et al. 2011; Zsom et al. 2010, 2011). Due to the dependence of the collision outcome on the collision velocity, an accurate evaluation of the turbulence-induced relative velocity is important for modeling the size distribution of dust particles.

Saffman and Turner (1956) studied the relative velocity in the limit of small particles with the particle friction or stopping time, τ_p , much smaller than the Kolmogorov timescale, τ_η , of the turbulent flow. This limit, known as the Saffman-Turner limit, is usually expressed as $St \ll 1$, where the Stokes number is defined as $St \equiv \tau_p/\tau_\eta$. Saffman and Turner (1956) predicted that, at a given particle distance, r , the relative velocity of identical particles is independent of St , and, at a given St , it scales linearly with r for small r . In the opposite limit of large particles with τ_p larger than the largest timescale of the turbulent flow, Abrahamson (1975) showed that the relative velocity scales with the friction time as $\tau_p^{-1/2}$. A variety of models have been developed to bridge the two limits and predict the relative velocity for particles of any size, i.e., with τ_p covering the entire scale range of the carrier flow (Williams & Crane 1983, Yuu 1984, Kruis & Kusters 1997, & Alipchenkov 2003, Zaichik et al. 2006, Ayala et al. 2008). Among these models, the formulation of Zaichik and collaborators is particularly impressive, as it examines both turbulent clustering and turbulence-induced relative velocity simultaneously. The model prediction for the relative velocity agrees well with simulation results at low resolutions. However, the model lacks a transparent physical picture.

Pan & Padoan (2010) developed a new model for the relative velocity of inertial particles of any size that provides an insightful physical picture of the problem. Their formulation illustrates that the relative velocity of identical particles is determined by the memory of the flow velocity difference along their trajectories in the past.

The model also shows that the separation of inertial particle pairs backward in time plays an important role in the relative velocity of nearby particles. The model can correctly reproduce the scaling behaviors of the relative speed in the extreme limits of small and large particles (see above), and its prediction was found to successfully match the simulation data of Wang et al. (2000). In this paper, we will further test the model against numerical simulations of considerably higher resolution.

Falkovich et al. (2002) discovered an interesting effect, named the sling effect, which provides an important contribution to the collision rate. The basic physical picture of this effect is that inertial particles may be shot out of fluid streamlines with high curvature, causing their trajectories to cross with those of other particles (Falkovich & Pumir 2007). In particular, in flow regions with large negative velocity gradients, fast particles can catch up with the slower ones from behind. For small particles with $St \ll 1$, the sling events correspond to high-order statistics of the flow velocity gradient, and the effect is not reflected in the prediction of Saffman and Turner (1956). The trajectory crossing causes the particle velocity to be multi-valued at a given point, leading to the formation of caustics in the momentum-position phase space of the particles (Wilkinson et al. 2006). The slings or caustics increase the local particle density, and give rise to a finite and significant collision velocity for particles even at an infinitesimal distance (Falkovich et al. 2002, Wilkinson et al. 2006). Both effects tend to enhance the particle collision rate. It has been shown that, as St approaches 1, the effect of slings or caustics causes a rapid rise in the collision rate, which has been proposed to be responsible for the initiation of rain shower in terrestrial clouds (Wilkinson et al. 2006). Applying this effect to dust particle collisions in protoplanetary disks, one may expect that the collision rate greatly accelerates as the particle grows past sub-mm to mm size, corresponding to $St \simeq 1$ for typical protoplanetary turbulence conditions.

The recent developments mentioned above have not been considered in coagulation models for dust particles in circumstellar disks. We find that, in the astrophysical literature, the general formulation of the collision kernel of dust coagulation models is inaccurate. In particular, the formulation significantly underestimates the collision rate for particles with $St \simeq 1$, because it ignores the effect of turbulent clustering. Furthermore, the dust coagulation models usually adopt collision velocities from the work of Volk et al. (1980) and its later extensions (e.g., Markiewicz, Mizuno & Volk 1991, Cuzzi and Hogan 2003, and Ormel & Cuzzi 2007), which has a number of severe limitations. First, Pan & Padoan (2010) pointed out a weakness in the physical picture of these models. Roughly speaking, these models assume the velocities of two particles induced by turbulent eddies with turnover time significantly smaller (larger) than τ_p are independent (correlated). As shown by Pan & Padoan (2010), whether the particle velocities contributed by turbulent eddies of a given size are correlated or not also depends on how the eddy size compares to the separation of the particles at the time the eddies were encountered, so the eddy turnover time is not the only factor that determines the degree of correlation. The role of the particle separation relative to the eddy size is not captured by the ap-

proach of Volk et al. Second, the models do not account for the dependence of the relative velocity on the particle distance, r , and, as a result, they cannot reproduce the Saffman-Turner regime for small particles. We will show that the relative velocity does have a r -dependence for $St \lesssim 6$ particles, which, together with the scale dependence of turbulent clustering, is crucial for the evaluation for the collision kernel of these particles. Finally, the model of Volk et al. is found to overestimate, by a factor of 2, the relative velocity of particles with τ_p of the order of the large eddy turnover time.

In this paper, we use numerical simulations to study inertial particle dynamics in turbulent flows. With the simulation data, we test the model of Pan & Padoan (2010) and compute the collision kernel as a function of St . We also explore the probability distribution function (PDF) of the relative velocity, which is expected to have important effects on the particle size distribution. As mentioned earlier, the outcome of dust particle collisions depends on the collision velocity, and thus, due to the stochastic nature of turbulence-induced relative velocity, collisions between particles of the same properties may lead to different outcomes. The PDF of the collision velocity is needed to estimate the fractions of collisions leading to sticking, bouncing or fragmentation. The PDF of the particle relative velocity has been shown to be highly non-Gaussian by various numerical, experimental and theoretical studies (e.g., Sundaram and Collins 1997, Wang et al. 2000, Gustavsson et al. 2008, Bec et al. 2009, de Jong et al. 2010, Gustavsson & Mehlig 2011, Hubbard 2012). This highly non-Gaussian nature of the relative velocity should be incorporated into coagulation models for the size distribution of dust particles in protoplanetary disks.

In this work, we will investigate the particle dynamics only in statistically homogeneous and isotropic turbulence. This is clearly an idealized situation, considering various complexities in protoplanetary disks. For example, the disk rotation induces large-scale anisotropy, which may have significant effects on the prediction for particles with friction time close to the rotation period. Nevertheless, the idealized problem is a very useful tool to understand the fundamental physics, and it provides the first step toward accurately modeling the dust particle collision velocity in protoplanetary turbulence. We also neglect the vertical settling and radial drift. These processes do not directly affect the relative velocity between identical particles, although they probably provide important contributions for particles of different sizes that we address in a follow-up work.

The paper is organized as follows. In §2, we present a simple model for the rms velocity of a single particle, which provides an illustration for our formulation of the particle relative velocity. In §3, we introduce the model of Pan & Padoan (2010) for the relative velocity of nearby particles, review the physical picture of the model, and discuss the qualitative behavior of the model predictions. Our simulation setup and the statistical properties of the simulated turbulent flow are described in §4. §5 presents simulation results for the particle rms velocity. In §6, we test the model of Pan & Padoan (2010) with respect to the rms relative velocity of particles found in the simulation, compute the collision kernel accounting for the effects of both turbulent clustering and turbulence-induced

collision velocities, and present in detail the probability distribution of the relative velocity as a function of the particle inertia. The conclusions of our study are summarized in §7.

2. THE VELOCITY OF INERTIAL PARTICLES

The dynamics of inertial particles depends crucially on its friction or stopping timescale, τ_p . To evaluate of the friction timescale, we first need to compare the particle size, a_p , with the mean free path of the gas particles in the carrying flow. If the particle size is larger than the mean free path, the friction timescale is given by the Stokes law $\tau_p = \frac{2}{9} \left(\frac{\rho_d}{\rho} \right) \left(\frac{a_p^2}{\nu} \right)$, where ρ_d ($\simeq 1 \text{ g cm}^{-3}$) is the density of the dust material, ρ is the gas density, and ν is the kinematic viscosity of the flow. On the other hand, if a_p is smaller than the gas mean free path, the particle is in the Epstein regime and $\tau_p = \left(\frac{\rho_d}{\rho} \right) \left(\frac{a_p}{C_s} \right)$, where C_s is the sound speed in the flow. For example, for a typical value of the gas density in protoplanetary discs, $\rho \simeq 10^{-9} \text{ g cm}^{-3}$ at a radius of 1 AU, the mean free path of the gas particles is about 1 cm, and thus particles with a_p larger (smaller) than 1 cm are in the Stokes (Epstein) regime.

The velocity, $\mathbf{v}(t)$, of an inertial particle suspended in a turbulent velocity field, $\mathbf{u}(\mathbf{x}, t)$, obeys the equation

$$\frac{d\mathbf{v}}{dt} = \frac{\mathbf{u}(\mathbf{X}(t), t) - \mathbf{v}}{\tau_p}, \quad (1)$$

where $\mathbf{X}(t)$ is the position of the particle at time t , and $\mathbf{u}(\mathbf{X}(t), t)$ corresponds to the flow velocity “seen” by the particle. Eq. (1) has a formal solution,

$$\mathbf{v}(t) = \frac{1}{\tau_p} \int_{t_0}^t \mathbf{u}(\mathbf{X}(\tau), \tau) \exp\left(-\frac{t-\tau}{\tau_p}\right) d\tau, \quad (2)$$

where it is assumed that $t - t_0 \gg \tau_p$ and the particle has already lost the memory of its initial velocity at t_0 . The formal solution indicates that the velocity of an inertial particle is determined by the memory of the flow velocity along its trajectory within a timescale of $\simeq \tau_p$ in the past.

Although the aim of the present work is the collision velocity of inertial particle pairs, we start with a discussion of the single-particle (or “1-particle”) velocity induced by turbulent motions. We provide a simple model for the 1-particle rms velocity as a function of the particle friction time. The derivation of this model helps to illustrate our formulation for the collision velocity between two nearby particles.

The 1-particle rms velocity can be calculated using the formal solution of eq. (2). We assume the turbulent flow is statistically stationary, and the particle statistics eventually relax to a steady state. We consider a time when the steady state is already reached and, without loss of generality, we denote this time as time 0. Using eq. (2) at $t = 0$, we have,

$$\langle v_i v_j \rangle = \int_{-\infty}^0 \frac{d\tau}{\tau_p} \int_{-\infty}^0 \frac{d\tau'}{\tau_p} B_{Tij}(\tau, \tau') \exp\left(\frac{\tau}{\tau_p}\right) \exp\left(\frac{\tau'}{\tau_p}\right), \quad (3)$$

where $B_{Tij}(\tau, \tau') \equiv \langle u_i(\mathbf{X}(\tau), \tau) u_j(\mathbf{X}(\tau'), \tau') \rangle$ is the temporal correlation tensor of the flow velocity along the trajectory, $\mathbf{X}(\tau)$, of the inertial particle. The subscript

“T” stands for “trajectory”. We have also changed the lower integration limit (t_0) in eq. (2) to $-\infty$, based on the assumption that the particle dynamics has been fully relaxed at time 0 (i.e., $t_0 \ll -\tau_p$).

With statistical stationarity and isotropy, the trajectory correlation tensor can be written as $B_{Tij}(\tau, \tau') = u'^2 \Phi_1(\tau' - \tau) \delta_{ij}$, where u' is the 1D rms velocity of the turbulent flow and the correlation coefficient Φ_1 is a function of the time lag only. The subscript “1” is used to indicate that the correlation is along the trajectory of *one* particle. The correlation coefficient, Φ_1 , is unknown, and a common assumption is to approximate it with the Lagrangian correlation function, Φ_L , of tracer particles (or fluid elements), which has been extensively studied in the literature. The assumption is likely valid for small particles, but cannot be justified for large particles on a theoretical basis. We will validate the assumption *a posteriori* using simulation results.

The simplest choice for the form of Φ_L is an exponential function, $\Phi_L(\Delta\tau) = \exp(-|\Delta\tau|/T_L)$, where $\Delta\tau = \tau' - \tau$ is the time lag and T_L the Lagrangian correlation timescale. Setting $B_{Tij} = u'^2 \exp(-|\tau' - \tau|/T_L) \delta_{ij}$ in eq. (3), we have $\langle v_i v_j \rangle = v'^2 \delta_{ij}$, where the 1D rms particle velocity, v' , is given by,

$$v' = u' \left(\frac{T_L}{T_L + \tau_p} \right)^{1/2}. \quad (4)$$

This result shows that the particle rms velocity approaches the flow velocity for $\tau_p \ll T_L$ and decreases as $(T_L/\tau_p)^{1/2}$ for $\tau_p \gg T_L$ (e.g., Abrahamson 1975). In the large particle limit, $\tau_p \gg T_L$, the action of even the largest turbulent eddies on the particle would appear to be random kicks when viewed on a timescale of τ_p . In that case, eq. (1) is essentially a Langevin equation, and the particle motions are similar to Brownian motions. The $\tau_p^{-1/2}$ scaling corresponds to an “equilibrium” between the velocity of these large particles and the turbulent motions of the flow.

Numerical simulations have shown that the Lagrangian correlation function, $\Phi_L(\Delta\tau)$, is better fit by a bi-exponential form (e.g., Sawford 1991). A single-exponential form does not reflect the smooth part of the correlation function for time lag $\Delta\tau$ smaller than the Taylor micro timescale, τ_T . The Taylor timescale is defined as $(2u'^2/a^2)^{1/2}$, where a is the rms acceleration of the turbulent velocity field. The bi-exponential form for $\Phi_L(\Delta\tau)$ is,

$$\Phi_L(\Delta\tau) = \frac{1}{2\sqrt{1-2z^2}} \left\{ (1 + \sqrt{1-2z^2}) \times \exp \left[-\frac{2|\Delta\tau|}{(1 + \sqrt{1-2z^2})T_L} \right] - (1 - \sqrt{1-2z^2}) \times \exp \left[-\frac{2|\Delta\tau|}{(1 - \sqrt{1-2z^2})T_L} \right] \right\}, \quad (5)$$

where the parameter z is defined as the ratio, $z = \tau_T/T_L$. From the above equation, it is easy to show that $T_L = \int \Phi_L(\Delta\tau) d\Delta\tau$, and the bi-exponential function is

smooth, $\simeq 1 - (\Delta\tau/\tau_T)^2$, at $\Delta\tau \ll \tau_T$. In the limit $z \rightarrow 0$, eq. (5) reduces to the single exponential with a timescale of T_L .

Adopting the bi-exponential form, eq. (5), for the trajectory correlation coefficient, Φ_1 , we find that the one-particle rms velocity is given by,

$$v' = u' \left(\frac{\Omega + z^2/2}{\Omega + \Omega^2 + z^2/2} \right)^{1/2}, \quad (6)$$

where Ω is defined as $\Omega \equiv \tau_p/T_L$. In the limits $\Omega \ll 1$ and $\Omega \gg 1$, eq. (6) has the same behavior as eq. (4) from the single exponential correlation. In fact, the two predictions, eqs. (4) and (6), are close to each other at all values of Ω , differing only by a few percent at $\Omega \simeq 1$. This suggests that, for a given correlation timescale, $T_L (\equiv \int \Phi_L(\Delta\tau) d\Delta\tau)$, the integral in eq. (3) is insensitive to the exact function form of the correlation, $\Phi_1(\Delta\tau)$. We will measure the parameters, z and T_L , using Lagrangian tracer particles in our simulated turbulent flow, and test the predictions, eqs. (4) and (6), for the 1-particle rms velocity against the simulation data.

3. TURBULENCE-INDUCED RELATIVE VELOCITY OF INERTIAL PARTICLES

We briefly review the 2-point Eulerian statistics of the velocity field in fully-developed turbulence, which is crucial to understand the relative velocity of two inertial particles. We consider the 2nd-order structure tensor, defined as $S_{ij}(\ell) = \langle \Delta u_i \Delta u_j \rangle$ where $\Delta u_i = u_i(\mathbf{x} + \ell, t) - u_i(\mathbf{x}, t)$ is the velocity increment across a separation ℓ and $\langle \dots \rangle$ denotes the ensemble average. The statistics of Δu_i is independent of \mathbf{x} and t from the assumption of homogeneity and stationarity. With statistical isotropy, the velocity structure tensor takes the form (e.g., Monin and Yaglom 1975),

$$S_{ij}(\ell) = S_{nn}(\ell) \delta_{ij} + [S_{ll}(\ell) - S_{nn}(\ell)] \frac{\ell_i \ell_j}{\ell^2} \quad (7)$$

where the longitudinal and transverse structure functions, S_{ll} and S_{nn} , are functions of the amplitude, ℓ , of the separation, ℓ , but not of its direction, ℓ/ℓ . From eq. (7), we see $S_{ll} = S_{ij}(\ell) \ell_i \ell_j / \ell^2 = \langle \Delta u_r^2 \rangle$, where $\Delta u_r = \Delta u_i \ell_i / \ell$ is the radial component of the flow velocity increment. Similarly, the transverse structure function S_{nn} can be written as $S_{nn} = \langle (\Delta u_t)^2 \rangle$ with Δu_t being one of the two components of Δu_i on the tangential/transverse plane perpendicular to ℓ . The statistical isotropy indicates that the probability distribution of Δu_t is invariant under any rotation about the direction ℓ/ℓ . In incompressible turbulence, which is approximately the case for gas flows in protoplanetary disks, we have the relation $S_{nn} = S_{ll} + \frac{1}{2} \ell dS_{ll}/d\ell$, which can be derived from the incompressibility condition: $\partial_j S_{ij}(\ell) = 0$ (Monin and Yaglom 1975).

The structure functions exhibit different scaling behaviors in different scale ranges. There are three subranges divided by two length scales, the Kolmogorov length scale, η , and the integral length scale L . The Kolmogorov scale, η , is defined as $\eta = (\nu^3/\bar{\epsilon})^{1/4}$, where ν and $\bar{\epsilon}$ are, respectively, the kinematic viscosity and the average energy dissipation rate in the turbulent flow. It essentially corresponds to the size of the smallest eddies.

Scales below η are called the viscous or dissipation range, where the velocity field is laminar and differentiable due to the smoothing effect of the viscosity. In the dissipation range ($\ell \lesssim \eta$), the velocity difference scales linearly with ℓ , and the longitudinal structure function is $S_{\parallel} = \frac{\bar{\epsilon}}{15\nu}\ell^2$. S_{nn} is twice larger, i.e., $S_{\text{nn}} = \frac{2\bar{\epsilon}}{15\nu}\ell^2$, as required by the incompressibility constraint. In the inertial range, $\eta \lesssim \ell \lesssim L$, S_{\parallel} follows the Kolmogorov scaling, $S_{\parallel} = C_K(\bar{\epsilon}\ell)^{2/3}$, where the coefficient C_K is known as the Kolmogorov constant. The typical value of C_K is $\simeq 2$. The incompressibility condition gives $S_{\text{nn}} = 4S_{\parallel}/3$ in the inertial range. The integral scale, L , is essentially the correlation length scale of the velocity field. At $\ell \gg L$, the velocity field is statistically uncorrelated, and both $S_{\parallel}(\ell)$ and $S_{\text{nn}}(\ell)$ are constant and equal to $2u'^2$ with u' the 1D rms velocity of the flow.

To bridge the scalings of S_{\parallel} in the three scale ranges, we adopt a connecting formula (Zaichik et al. 2006),

$$S_{\parallel} = 2u'^2 \left[1 - \exp\left(-\frac{(\ell/\eta)}{(15C_K)^{3/4}}\right) \right]^{4/3} \times \left[\frac{(\ell/\eta)^4}{(\ell/\eta)^4 + (2u'^2/C_K u_\eta^2)^6} \right]^{1/6}, \quad (8)$$

where u_η is the Kolmogorov velocity scale defined as $(\nu\bar{\epsilon})^{1/4}$. With eq. (8) for S_{\parallel} , we can obtain S_{nn} using the incompressibility condition (see above). Alternatively, one may adopt a separate connecting formula for S_{nn} . In §4.3, we will measure the structure functions in our simulated flow, and fit them with connecting formulas.

The goal of this work is to understand and predict the velocity at which two nearby inertial particles collide. The collision speed of two particles is essentially their relative velocity as they cross, i.e., as their distance, r , becomes equal to the sum of the particle radii (Saffman and Turner 1956). For applications to dust particles in protoplanetary disks, the particle size is typically much smaller than the Kolmogorov length scale, η . In the following, we therefore explore the relative speed of particles at small distances, $r \lesssim \eta$.

We label two particles coming together with superscripts (1) and (2). For example, we denote their positions as $\mathbf{X}^{(1)}(t)$ and $\mathbf{X}^{(2)}(t)$, and their velocities as $\mathbf{v}^{(1)}(t)$ and $\mathbf{v}^{(2)}(t)$ (see Fig. 1 for illustration). When the superscripts (1) and (2) are not used, the discussion is general and not referring to a specific particle. At a given time t , we consider the relative velocity $\mathbf{w} \equiv \mathbf{v}^{(2)}(t) - \mathbf{v}^{(1)}(t)$, of particle pairs at a given separation, \mathbf{r} , which corresponds to a constraint $\mathbf{X}^{(2)}(t) - \mathbf{X}^{(1)}(t) = \mathbf{r}$ for the particle positions. We first present a theoretical model for the second-order moment of \mathbf{w} , and then use numerical simulations to explore its full statistics, including the probability distribution function (PDF), as a function of τ_p .

Similar to the structure tensor of the flow velocity, we characterize the second-order statistics of the particle relative velocity \mathbf{w} by a structure tensor,

$$S_{p_{ij}} \equiv \langle w_i w_j \rangle = \left\langle \left(v_i^{(2)} - v_i^{(1)} \right) \left(v_j^{(2)} - v_j^{(1)} \right) \right\rangle, \quad (9)$$

which was referred to as the particle velocity structure tensor by Pan and Padoan (2010). The tensor $S_{p_{ij}}$ can

be evaluated using the formal solution, eq. (2), of the particle velocity and the statistical properties of the carrier flow (see Pan and Padoan 2010 and §3.2).

Once the particle dynamics is fully relaxed, the particle velocity is expected to possess the same statistical symmetries as the flow, including stationarity, homogeneity and isotropy. With these symmetries, the particle structure tensor $S_{p_{ij}}$ can be written in a similar form as the structure tensor of the flow (eq. 7),

$$S_{p_{ij}}(\mathbf{r}) = \langle w_t^2 \rangle \delta_{ij} + (\langle w_r^2 \rangle - \langle w_t^2 \rangle) \frac{r_i r_j}{r^2}, \quad (10)$$

where $\langle w_r^2 \rangle$ and $\langle w_t^2 \rangle$ are the variances of the radial/longitudinal component, $w_r \equiv w_i r_i / r$, and a tangential/transverse component, w_t , of the relative velocity, respectively. For particle collisions, we are only interested in $S_{p_{ij}}$ at $r \lesssim \eta$. Under the assumption of isotropy, the tangential component, w_t , is expected to be statistically invariant for any rotations about the axis \mathbf{r} . We can thus measure the statistics of the tangential relative velocity by projecting \mathbf{w} into an arbitrary direction on the plane perpendicular to \mathbf{r} .

The radial relative speed, w_r , is of particular interest for the estimate of the particle collision frequency (Wang et al. 2000; see §6.2), and its variance is related to the particle structure tensor as $\langle w_r^2 \rangle = S_{p_{ij}} r_i r_j / r^2$. The total collisional energy of a particle pair plays a crucial role in the outcome of the collision (e.g., Blum and Wurm 2008). The average collisional energy can be computed from the 3D variance, $\langle w^2 \rangle$, of the relative velocity, which is the contraction of the particle structure tensor, i.e., $S_{p_{ii}} = \langle w_r^2 \rangle + 2\langle w_t^2 \rangle$. In the rest of this section, we consider theoretical models for the variances of the relative velocity. As mentioned earlier, we focus on the monodisperse case with equal-size particles.

3.1. The Limits of Small and Large Particles

We first consider small particles in the Saffman-Turner limit (hereafter the S-T limit). In this limit, the friction timescale, τ_p , is much smaller than the Kolmogorov timescale, τ_η , of the carried flow, which is defined as $\tau_\eta \equiv (\nu/\bar{\epsilon})^{1/2}$. The Kolmogorov timescale is the smallest timescale in a turbulent flow, corresponding to the turnover time of the smallest eddies. Therefore, the velocity of particles with $\tau_p \ll \tau_\eta$ can be approximated by a Taylor expansion of eq. (1), $\mathbf{v}(t) \simeq \mathbf{u}(\mathbf{X}, t) + \tau_p \mathbf{a}(\mathbf{X}, t)$, where $\mathbf{a} = D\mathbf{u}/Dt$ is the acceleration of the local fluid element. Applying the approximation to both particles (1) and (2), we have $\mathbf{w} = (\mathbf{u}^{(2)} - \mathbf{u}^{(1)}) + (\mathbf{a}^{(2)} - \mathbf{a}^{(1)}) \tau_p$, where $\mathbf{u}^{(1,2)} \equiv \mathbf{u}(\mathbf{X}^{(1,2)}, t)$ and $\mathbf{a}^{(1,2)} \equiv \mathbf{a}(\mathbf{X}^{(1,2)}, t)$ are the flow velocity and acceleration at the positions of particles (1) and (2), respectively. Saffman and Turner (1956) assumed that the correlation coefficient of the flow accelerations, $\mathbf{a}^{(1)}$, and $\mathbf{a}^{(2)}$, across a small distance, r , is unity, which is equivalent to assuming $\mathbf{a}^{(1)} \simeq \mathbf{a}^{(2)}$. The acceleration terms then cancel out for identical particles, and the particle structure tensor, $S_{p_{ij}}$, is simply equal to the flow structure tensor, S_{ij} , defined in eq. (7). Using the flow structure functions S_{\parallel} and S_{nn} at $r \ll \eta$ in incompressible turbulence, we have the Saffman-Turner formula,

$$\langle w_r^2 \rangle = \frac{1}{15} \frac{\bar{\epsilon}}{\nu} r^2, \quad \langle w_t^2 \rangle = \frac{2}{15} \frac{\bar{\epsilon}}{\nu} r^2, \quad (11)$$

for identical particles with $St \ll 1$. The equation shows that in the S-T limit the relative speed is caused by the flow velocity difference across the particle separation. The effect is usually referred to as the shear contribution¹. From eq. (11), the 3D variance of the relative velocity is given by $\langle w^2(r) \rangle = \frac{\bar{\epsilon}}{3\nu} r^2$.

The S-T formula predicts that the tangential variance of the relative velocity, $\langle w_t^2 \rangle$, is twice larger than that in the radial direction. Eq. (11) also indicates a constant relative speed at a given separation, r , and a linear scaling with r at a given $St \ll 1$. The accuracy of the Saffman-Turner formula has been questioned, which neglects the effect of slings and caustic formation (e.g., Falkovich et al. 2002, Wilkinson et al. 2006). We will test the S-T prediction against our simulation data. In the S-T limit, the particle memory is short and the relative speed is determined largely by the local flow velocity at small scales. The memory effect becomes important for larger particles with $\tau_p > \tau_\eta$ (see §3.2).

We next consider the other extreme limit, i.e., large particles with τ_p much larger than the Lagrangian correlation time, T_L , of the flow. As discussed in §2, the motions of these particles are similar to Brownian motions, and the velocities of any two particles are statistically independent. This is because the velocity of a large particle has a significant contribution from its memory of the flow velocity long time ago, and the flow velocities “seen” by the two particles at that time were uncorrelated because the particle separation was likely larger than the flow integral length scale, L . With the independence of $\mathbf{v}^{(1)}$ and $\mathbf{v}^{(2)}$, the particle structure tensor defined in eq. (9) can be written as $S_{pij} = \left[(v^{(1)})^2 + (v^{(2)})^2 \right] \delta_{ij}$, where $v^{(1)}$ and $v^{(2)}$ are the (1D) rms velocities of particles (1) and (2), respectively. As shown in §2, for particles with $\tau_p \gg T_L$, the rms velocity is given by $\simeq u' (T_L/\tau_p)^{1/2}$. We therefore have (e.g., Abrahamson 1975),

$$\langle w_r^2 \rangle = \langle w_t^2 \rangle = 2u'^2 \frac{T_L}{\tau_p} \quad (12)$$

for identical particles with $\tau_p \gg T_L$. The equation suggests that the particle relative speed decreases with the Stokes number as $St^{-1/2}$. The physical picture for the relative velocity in the large particle limit is clear, and the result, eq. (12), is robust.

In between the two extreme limits are particles in the inertial range, i.e., particles with friction timescale $\tau_\eta \lesssim \tau_p \lesssim T_L$, corresponding to inertial-range scales in the turbulent flow. The physics for the relative velocity of inertial-range particles is more complicated. For example, in the two extreme limits the velocity correlation of two nearby particles is relatively easy to estimate: The velocities are either highly correlated (for small particles) or essentially independent (for large particles). On the other hand, for inertial-range particles, the velocity correlation is at an intermediate level. We will show that the key physics for the relative velocity of inertial-range

particles is the particles’ memory of the flow velocity difference in the past and the separation of the particle pair backward in time.

As mentioned in the Introduction, a variety of models for the particle relative velocity covering the whole range of particle sizes have been developed (e.g., Volk et al. 1980, Ormel & Cuzzi 2007, Zaichik & Alipchenkov 2003, Zaichik et al. 2006, and Pan & Padoan 2010). The models listed here all predict a $St^{1/2}$ scaling for inertial-range particles in turbulent flows with an extended inertial range. The models of Zaichik and collaborators and Pan and Padoan (2010) can reproduce both the S-T limit (eq. (11)) and the large particle limit (eq. (12)). We will focus on the model of Pan and Padoan (2010), which provides a clearer physical picture than that of Zaichik et al. The physical differences between various models have been summarized in Pan and Padoan (2010).

3.2. The Model of Pan and Padoan (2010)

We first review the formulation and the physical picture of the model by Pan & Padoan (2010; hereafter PP10) for the relative velocity of identical particles. The main idea of the PP10 model was to evaluate the particle velocity structure tensor, $S_{pij}(\mathbf{r})$, using the formal solution (eq. (2)) for the particle velocity. Applying eq. (2) to the velocities of particles (1) and (2) at $t = 0$, we have,

$$\mathbf{v}_i^{(2)} - \mathbf{v}_i^{(1)} = \frac{1}{\tau_p} \int_{-\infty}^0 \left[\mathbf{u}_i^{(2)}(\tau) - \mathbf{u}_i^{(1)}(\tau) \right] \exp\left(\frac{\tau}{\tau_p}\right) d\tau, \quad (13)$$

where $\mathbf{u}^{(1,2)}(\tau) (\equiv \mathbf{u}(\mathbf{X}^{(1,2)}(\tau), \tau))$ are the flow velocities “seen” by the two particles at time τ . Again we have changed the lower integration limit in the formal solution, eq. (2), to $-\infty$.

Inserting eq. (13) into the definition, eq. (9), of S_{pij} , it is straightforward to find that,

$$S_{pij}(\mathbf{r}) = \int_{-\infty}^0 \frac{d\tau}{\tau_p} \int_{-\infty}^0 \frac{d\tau'}{\tau_p} S_{Tij}(\mathbf{r}; \tau, \tau') \times \exp\left(\frac{\tau}{\tau_p}\right) \exp\left(\frac{\tau'}{\tau_p}\right), \quad (14)$$

where S_{Tij} , named the trajectory structure tensor by PP10, is defined as,

$$S_{Tij}(\mathbf{r}, \tau, \tau') = \left\langle \left[\mathbf{u}_i^{(2)}(\tau) - \mathbf{u}_i^{(1)}(\tau) \right] \left[\mathbf{u}_j^{(2)}(\tau') - \mathbf{u}_j^{(1)}(\tau') \right] \right\rangle. \quad (15)$$

Clearly, this tensor corresponds to the correlation of the flow velocity differences along the trajectories of the two particles at two times τ and τ' . The trajectory structure tensor, S_{Tij} , depends on the separation, \mathbf{r} , through the constraint that $\mathbf{X}^{(2)}(0) - \mathbf{X}^{(1)}(0) = \mathbf{r}$. Note that eq. (14) is in close analogy with eq. (3) for the 1-particle velocity. Here the trajectory structure tensor, S_{Tij} , replaces the trajectory correlation tensor, B_{Tij} , in eq. (3).

The physical meaning of eqs. (13) and (14) is clear: the relative velocity of two identical inertial particles is controlled by the particles’ memory of the flow velocity difference within a friction timescale, $\sim \tau_p$, in the past. The physical picture is illustrated in Fig. 1. The trajectory structure tensor, S_{Tij} , is unknown, and we next

² The term “shear contribution” is as opposed to the “acceleration contribution” from the acceleration terms mentioned above, which do not vanish for particles of different sizes. The acceleration contribution in the bidisperse case will be discussed in a separate paper.

model it using the approach of PP10.

Since the flow velocity difference scales with the distance, the trajectory structure tensor, S_{Tij} , has an indirect dependence on the particle separation at τ and τ' . We denote the particle separation at τ as $\mathbf{d}(\tau)$ ($\equiv \mathbf{X}^{(2)}(\tau) - \mathbf{X}^{(1)}(\tau)$). The separation vector \mathbf{d} is stochastic because of the random dispersion of the particle pair by turbulent motions. S_{Tij} also has a dependence on the time lag $(\tau' - \tau)$. This dependence is associated with the temporal correlation of turbulent structures or eddies encountered by the two particles between τ and τ' , and the correlation time is essentially the turnover time of these eddies. To estimate S_{Tij} , we consider the (indirect) spatial dependence on the particle separation and the temporal dependence on the time lag separately.

We use a typical particle separation $\mathbf{R}(\tau, \tau')$ between τ and τ' to model the spatial dependence. Clearly, $\mathbf{R}(\tau, \tau')$ is a random vector because of the stochasticity of $\mathbf{d}(\tau)$ and $\mathbf{d}(\tau')$. We approximate the dependence on the separation by the Eulerian structure tensor of the flow velocity, $S_{ij}(\mathbf{R})$, defined in eq. (7). We denote as $\Phi_2(\tau' - \tau, R)$ the temporal correlation of the flow structure at the scale R . The correlation, Φ_2 , is expected to be an even function of the time lag and is normalized to unity, $\Phi_2(0, R) = 1$, at zero time lag. To distinguish from the temporal correlation, $\Phi_1(\tau' - \tau)$, along the trajectory of a single particle (see §2), we have used a subscript “2” here for the two-particle case. The function form of Φ_2 will be specified in §3.2.1. The trajectory structure tensor is then modeled as the product of the two dependences (PP10),

$$S_{Tij}(\mathbf{r}; \tau, \tau') \simeq \langle S_{ij}(\mathbf{R}) \Phi_2(\tau' - \tau, R) \rangle_{\mathbf{R}} \quad (16)$$

where $\langle \cdots \rangle_{\mathbf{R}}$ denotes the average over the statistics of the random vector, \mathbf{R} . The average is over the probability distributions of both the amplitude, R , and the direction of \mathbf{R} . Eq. (16) implicitly assumes the statistical independence of the velocity difference, $\Delta \mathbf{u}$, seen by the two particles from their separation, \mathbf{R} . Rigorously, the amplitudes of $\Delta \mathbf{u}$ and \mathbf{R} may have a correlation. If the particle pair encounters an eddy with a larger velocity, the particle separation tends to be larger. For example, if R is in the inertial range of the flow, $\Delta u \simeq \epsilon_R^{1/3} R^{1/3}$ from the refined similarity hypothesis (Kolmogorov 1962), where ϵ_R is the average dissipation rate over the scale R as seen by the particle pair. A positive correlation is expected between ϵ_R and R . Eq. (16) neglects this correlation and may underestimate S_{Tij} and hence the particle relative velocity.

The Φ_2 term in eq. (16) does not depend on the direction of \mathbf{R} , so one can first take the angular average of $S_{ij}(\mathbf{R})$ and then average the entire term over the PDF of the amplitude, R . The latter cannot be exactly performed because the PDF of R is unknown. With some simple estimates, PP10 argued that simply using the rms of R to evaluate S_{Tij} instead of averaging over the PDF of R only causes a small difference ($\simeq 10\%$) in the model prediction. Following PP10, we ignore the PDF of R and insert the rms of R to evaluate S_{Tij} . For the simplicity of notations, we use R to denote the rms of the particle distance in between τ and τ' in the rest of the paper. A similar notation is adopted for $d(\tau)$ and $d(\tau')$, which will denote the rms particle separations at τ and τ' , respec-

tively. We approximate R by the geometric average of $d(\tau)$ and $d(\tau')$,

$$R(\tau, \tau') = [d(\tau)d(\tau')]^{1/2}. \quad (17)$$

The rms separation $d(\tau)$ as a function of time τ will be discussed in §3.2.3.

With the above assumptions, the trajectory structure tensor is modeled as,

$$S_{Tij}(\mathbf{r}; \tau, \tau') \simeq \langle S_{ij}(\mathbf{R}) \rangle_{\text{ang}} \Phi_2(\tau' - \tau, R). \quad (18)$$

The angular average over the direction of \mathbf{R} will be carried out in §3.2.2. In eq. (18), the dependence of S_{Tij} on \mathbf{r} is through the dependence of the particle separations, $d(\tau)$, $d(\tau')$ and R , on \mathbf{r} . We will refer to \mathbf{r} as the “initial” separation, although it actually corresponds to the current or final separation of the two particles. Clearly, our formulation indicates that the separation of particle pairs backward in time is crucial for the prediction of the particle relative speed.

Inserting eq. (18) into eq. (14) gives the PP10 model for the particle structure tensor,

$$S_{prij}(\mathbf{r}) = \int_{-\infty}^0 \frac{d\tau}{\tau_p} \int_{-\infty}^0 \frac{d\tau'}{\tau_p} \langle S_{ij}(\mathbf{R}) \rangle_{\text{ang}} \times \Phi_2(\tau' - \tau, R) \exp\left(\frac{\tau}{\tau_p}\right) \exp\left(\frac{\tau'}{\tau_p}\right). \quad (19)$$

We will numerically compute this double integral after evaluating or modeling the angular average, the temporal correlation function and the particle separation backward in time.

A simplification of the PP10 model is to set \mathbf{R} to one of two distances, $\mathbf{d}(\tau)$ or $\mathbf{d}(\tau')$, instead of their geometric average. We find that replacing \mathbf{R} in eq. (19) by either $\mathbf{d}(\tau)$ or $\mathbf{d}(\tau')$ leads to equivalent model prediction for the particle relative speed. This is because the temporal correlation Φ_2 in eq. (19) is an even function of $\Delta\tau$ ($\equiv \tau' - \tau$), and the product of the two exponential cutoffs are invariant under the exchange of τ and τ' . If one sets $\mathbf{R} = \mathbf{d}(\tau)$ in eq. (19), the integral over τ' can be isolated, yielding,

$$S_{prij} = \frac{1}{\tau_p} \int_{-\infty}^0 \langle S_{ij}(\mathbf{d}(\tau)) \rangle_{\text{ang}} F(\tau) \exp\left(\frac{\tau}{\tau_p}\right) d\tau, \quad (20)$$

where the angular average is over the direction of $\mathbf{d}(\tau)$ and the function $F(\tau)$ is defined as,

$$F(\tau) = \frac{1}{\tau_p} \int_{-\infty}^0 \Phi_2(\tau' - \tau, d(\tau)) \exp\left(\frac{\tau'}{\tau_p}\right) d\tau'. \quad (21)$$

The factor $F(\tau)$ may be roughly viewed as a response function of the particle pair to turbulent eddies at the scale $d(\tau)$. Although not indicated explicitly, the factor $F(\tau)$ also depends on the initial particle separation, r , through its dependence on $d(\tau)$. We will refer to eqs. (20) and (21) as the simplified model. The advantage of the simplified model is that the response function $F(\tau)$ can be integrated analytically using assumed function forms of Φ_2 in §3.2.1, and one only needs to numerically solve a single integral in eq. (20). On the other hand, for the original PP10 model, one must numerically evaluate the double integral in eq. (19).

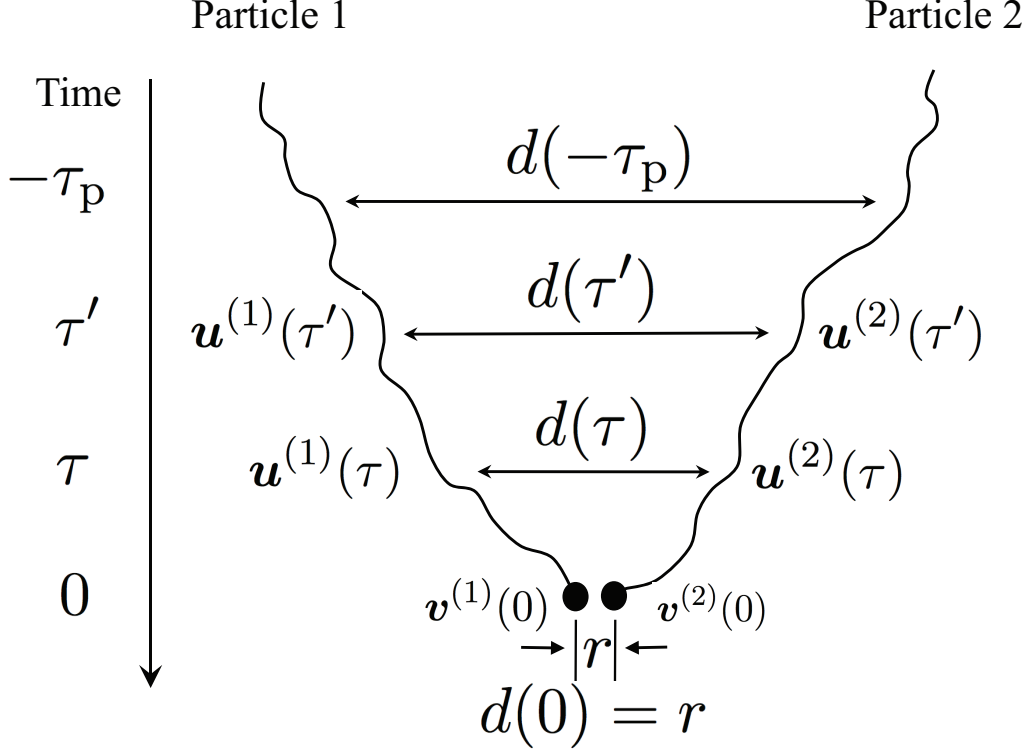


FIG. 1.— Schematic figure illustrating the physical picture of the PP10 model for the relative velocity of inertial particles of equal size. At time 0, the separation of the two inertial particles, (1) and (2), is r . The velocity, $\mathbf{v}(0)$, of each particle at $t = 0$, is determined by its memory of the flow velocity, $\mathbf{u}(\tau)$, along the particle trajectory in the past. The relative velocity of the two particles depends on the flow velocity difference, $\mathbf{u}^{(2)}(\tau) - \mathbf{u}^{(1)}(\tau)$, they “saw” within about a friction timescale τ_p in the past, i.e., $-\tau_p \lesssim \tau \leq 0$. The flow velocity difference at a given time τ is related to the particle separation, $d(\tau)$. The separation of the two particles satisfies the “initial” constraint $d(0) = r$ and increases backward in time. Due to particle inertia, a roughly ballistic separation is expected within a particle friction timescale. The trajectories plot here reflect a more-or-less linear separation of the two particles. The temporal correlation of the flow velocity differences the two particles “saw” at different times, say τ and τ' , is another important effect. The correlation timescale is associated with the turnover time for turbulent eddies encountered by the two particles between τ and τ' .

3.2.1. The temporal correlation Φ_2

To estimate the temporal correlation in the trajectory structure tensor, S_{Tij} , we first consider a special case where the typical particle separation, R , is much larger than the integral length scale, L , of the flow. In this case, the flow velocities, $\mathbf{u}^{(1)}$ and $\mathbf{u}^{(2)}$, “seen” by the two particles are independent, and S_{Tij} can be written as $\langle u_i^{(1)}(\tau) u_j^{(1)}(\tau') \rangle + \langle u_i^{(2)}(\tau) u_j^{(2)}(\tau') \rangle$ (see eq. (9)). Both terms correspond to the trajectory correlation tensor B_{Tij} defined below eq. (3) in §2, and for identical particles the two terms are equal. Therefore, for $R \gg L$, the correlation function $\Phi_2(\Delta\tau, R)$ is the same as the temporal correlation coefficient, $\Phi_1(\Delta\tau)$, along the trajectory of one particle.

In §2, we approximated Φ_1 by the Lagrangian correlation function, Φ_L . Using the approximation again, we have $\Phi_2(\Delta\tau, \ell) = \Phi_1(\Delta\tau) \simeq \Phi_L(\Delta\tau)$ for $\ell \gg L$. Two function forms, single- and bi-exponential, were adopted for Φ_L in §2. With the single-exponential form, we set $\Phi_2(\Delta\tau, \ell) = \exp(-|\Delta\tau|/T_L)$ for $\ell \gg L$. An extension of this function to smaller scales gives,

$$\Phi_2(\Delta\tau, \ell) = \exp\left(-\frac{|\Delta\tau|}{T(\ell)}\right), \quad (22)$$

where $T(\ell)$ is essentially the correlation timescale or lifetime of turbulent eddies of size ℓ . For $\ell \gg L$, we set

$$T(\ell) = T_L.$$

At smaller ℓ , $T(\ell)$ can be estimated using the velocity scalings in the turbulent flow. For ℓ in the inertial range, we obtain $T(\ell)$ by dividing ℓ by the amplitude of the turbulent velocity fluctuations at this scale, which is $(S_{11}(\ell) + 2S_{nn}(\ell))^{1/2}$. Using the Kolmogorov scaling, we have $T(\ell) = C_T \bar{\epsilon}^{-1/3} \ell^{2/3}$, where $C_T = (11C_K/3)^{-1/2} = 0.52C_K^{-1/2}$ with C_K being the Kolmogorov constant. The factor, $11/3$, is from the incompressibility relation $S_{nn} = 4S_{11}/3$ in the inertial range. Since C_K is $\simeq 2$, we set $C_T \simeq 0.4$. A similar value of C_T was adopted by Zaichik & Alipchenkov (2003). In the viscous range with $\ell \ll \eta$, the flow velocity difference goes linearly ℓ , and $T(\ell)$ is expected to be constant. Lundgren (1981) predicted that $T(\ell) = \sqrt{5}\tau_\eta$, which was later confirmed by numerical simulations of Girimaji & Pope (1990). We thus take $T(\ell) = \sqrt{5}\tau_\eta$ for $\ell \ll \eta$ in our model. We will use the bridging formula for $T(\ell)$ from Zaichik et al. (2006),

$$T(\ell) = T_L \left[1 - \exp\left(-\left(\frac{C_T}{\sqrt{5}}\right)^{3/2} (\ell/\eta)\right) \right]^{-2/3} \times \left[\frac{(\ell/\eta)^4}{(\ell/\eta)^4 + (T_L/(C_T\tau_\eta))^6} \right]^{1/6}, \quad (23)$$

which satisfies the scalings of $T(\ell)$ in different scale ranges.

One may also adopt a bi-exponential form for $\Phi_2(\Delta\tau, \ell)$ based on eq. (5) for the Lagrangian correlation function Φ_L (see §2). Replacing T_L in eq. (5) by $T(\ell)$ gives,

$$\Phi_2(\Delta\tau, \ell) = \frac{1}{2\sqrt{1-2z^2}} \left\{ (1 + \sqrt{1-2z^2}) \times \exp \left[-\frac{2|\Delta\tau|}{(1 + \sqrt{1-2z^2})T(\ell)} \right] - (1 - \sqrt{1-2z^2}) \times \exp \left[-\frac{2|\Delta\tau|}{(1 - \sqrt{1-2z^2})T(\ell)} \right] \right\}. \quad (24)$$

This bi-exponential form for $\Phi_2(\Delta\tau, \ell)$ was used in all the calculations in PP10. We will compute the predictions of the PP10 model using both the single- and bi-exponential correlation functions. We find the results from the two cases are close to each other, suggesting that the integral, eq. (19), is insensitive to the function form of $\Phi_2(\Delta\tau, \ell)$. After the integration, the dependence on $\Phi_2(\Delta\tau, \ell)$ is essentially condensed to a dependence on the correlation timescale $T(\ell)$. This is similar to the case of the one-particle velocity, which is insensitive to the form of $\Phi_1(\Delta\tau)$ (see §2). PP10 also considered the possible dependence of the parameter z on the length scale ℓ . It was found that including a reasonable length scale dependence of z barely changes the model prediction. We will set z to be constant in this study.

We next consider the simplified version of the PP10 model represented by eqs. (20) and (21). With the single-exponential form, eq. (22), for Φ_2 , the response factor, eq. (21), can be integrated,

$$F(\tau) = \frac{T(d)}{T(d) - \tau_p} \exp \left(\frac{\tau}{T(d)} \right) + \frac{2\tau_p T(d)}{\tau_p^2 - T^2(d)} \exp \left(\frac{\tau}{\tau_p} \right). \quad (25)$$

Since τ is negative, the response factor, $F(\tau)$, is dominated by the first term if $T(d) \gg \tau_p$, and it approaches $\exp(\tau/T(d))$ in that limit. On the other hand, for $T(d) \ll \tau_p$, the leading term is $\frac{2T(d)}{\tau_p} \exp(\tau/\tau_p)$. Note that eq. (25) does not diverge at $T(d) = \tau_p$. Applying the L'Hospital's rule shows that it converges to $(\frac{1}{2} - \frac{\tau}{\tau_p}) \exp(\tau/\tau_p)$, as $T(d) \rightarrow \tau_p$. Therefore, when numerically integrating eq. (20), we set $F(\tau) = (\frac{1}{2} - \frac{\tau}{\tau_p}) \exp(\tau/\tau_p)$ for $T(d)$ around τ_p .

With the bi-exponential temporal correlation, eq. (24), the response factor, $F(\tau)$, can also be integrated analytically. The integration is straightforward, but the resulting function for $F(\tau)$ is complicated and is thus omitted here. The predictions of the simplified model with single- and bi-exponential $\Phi_2(\Delta\tau, \ell)$ are also close to each other.

3.2.2. Averaging over the direction of \mathbf{R}

We evaluate the angular average of $S_{ij}(\mathbf{R})$ over the direction of \mathbf{R} . It follows from eq. (7) that $S_{ij}(\mathbf{R}) = S_{nn}(R)\delta_{ij} + [S_{ll}(R) - S_{nn}(R)]R_iR_j/R^2$. The contraction of the tensor is $S_{ii}(\mathbf{R}) = S_{ll}(R) + 2S_{nn}(R)$, and it does not have a direct dependence on the direction of \mathbf{R} . Therefore, for the prediction of the 3D rms relative speed, we

do not need to perform the angular average. However, for the radial and tangential components of the relative velocity, one must make an assumption for the direction of \mathbf{R} and compute the angular average of the term $\propto R_iR_j/R^2$.

In PP10, we assumed that the direction of the separation change, $\Delta\mathbf{R} \equiv \mathbf{R} - \mathbf{r}$, caused by turbulent dispersion is completely random and isotropic. One can then insert $\mathbf{R} = \Delta\mathbf{R} + \mathbf{r}$ into the above expression of $S_{ij}(\mathbf{R})$ and take the average over the direction of $\Delta\mathbf{R}$. From the assumed isotropy of $\Delta\mathbf{R}$, we have $\langle r_i\Delta R_j \rangle = 0$ and $\langle \Delta R_i\Delta R_j \rangle_{\text{ang}} = \frac{1}{3}(R^2 - r^2)\delta_{ij}$, and hence $\langle R_iR_j \rangle_{\text{ang}} \simeq r_ir_j + \frac{1}{3}(R^2 - r^2)\delta_{ij}$ (see PP10). The angular average $\langle S_{ij}(\mathbf{R}) \rangle_{\text{ang}}$ is then given by³,

$$\langle S_{ij}(\mathbf{R}) \rangle_{\text{ang}} = \delta_{ij} \left[\left(\frac{1}{3} - \frac{r^2}{3R^2} \right) S_{ll}(R) + \left(\frac{2}{3} + \frac{r^2}{3R^2} \right) \times S_{nn}(R) \right] + \left[S_{ll}(R) - S_{nn}(R) \right] \frac{r_ir_j}{R^2}. \quad (26)$$

Clearly, the equation approaches $S_{ij}(\mathbf{r})$ in the limit $R \rightarrow r$. PP10 showed that eq. (26) reproduces the Saffman-Turner formula for the radial and tangential relative speeds. In the limit with $R \gg r$, we have $\langle S_{ij}(\mathbf{R}) \rangle_{\text{ang}} \simeq \frac{1}{3}[S_{ll}(R) + 2S_{nn}(R)]$.

Here we make a simpler assumption than PP10: we take the direction of \mathbf{R} (rather than $\Delta\mathbf{R}$) to be isotropic. This means $\langle R_iR_j/R^2 \rangle_{\text{ang}} = \frac{1}{3}\delta_{ij}$, and we have,

$$\langle S_{ij}(\mathbf{R}) \rangle_{\text{ang}} = \frac{1}{3}[S_{ll}(R) + 2S_{nn}(R)]\delta_{ij}, \quad (27)$$

which suggests that the particle structure tensor $S_{pij} \propto \delta_{ij}$ (see eq. (19)), and hence $\langle w_r^2 \rangle = \langle w_t^2 \rangle$ (see eq. (10)) for particles of any size. A comparison of the two assumptions, eqs. (26) and (27), shows that they differ only at $R \lesssim r$.

As expected, the contraction, $\langle S_{ii}(\mathbf{R}) \rangle_{\text{ang}}$, of both eq. (26) and eq. (27), is equal to $[S_{ll}(R) + 2S_{nn}(R)]$, indicating that the two assumptions give the same prediction for the 3D rms relative velocity. The only difference between the two assumptions is the prediction for the radial and tangential components of the relative velocity in the small particle limit $St \ll 1$. In §3.2.4, we will compare the model predictions in this limit with both assumptions. The angular average $\langle S_{ij}(\mathbf{d}) \rangle_{\text{ang}}$ in the simplified model (eq. (20)) can be evaluated in a similar way, and the resulting expressions are the same as eqs. (26) and (27) with $d(\tau)$ replacing $R(\tau, \tau')$.

3.2.3. The backward dispersion of particle pairs

To complete the model, we finally specify the (rms) particle separation, $d(\tau)$, as a function of τ . The separation of inertial particle pairs backward in time has not been explored in the literature. Fortunately, Bec et al. (2010) carried out a detailed numerical study of the forward-in-time pair dispersion of inertial particles.

³ Rigorously, the amplitude, R , of \mathbf{R} and hence $S_{ll}(R)$ and $S_{nn}(R)$ have a dependence on the direction of $\Delta\mathbf{R}$. However, the average of these quantities over the direction of $\Delta\mathbf{R}$ is complicated and cannot be done analytically. For simplicity, we kept R , S_{ll} and S_{nn} fixed, and only accounted for the angular average of R_iR_j .

Following PP10, we use their results to guide the assumption for the backward dispersion. We first consider the separation behavior of inertial-range particles with $\tau_\eta \lesssim \tau_p \lesssim T_L$, and then discuss other particles at the end of this subsection.

Bec et al. (2010) found that the separation of inertial particles shows different behaviors at early and late times. At early times, a clear ballistic phase is observed for particles with $St \gtrsim 1$. In this phase, the separation increases linearly with time, and the phase lasts for about a friction timescale. The ballistic behavior is easy to understand: The particle velocity tends to be roughly constant for a memory timescale, τ_p . The reasoning also applies to the dispersion backward in time. We thus assume that, for particle pairs at an “initial” distance of r , the separation $d(\tau)$ in the time range $-\tau_p \lesssim \tau \leq 0$ is given by,

$$d^2(\tau) = r^2 + \langle w^2 \rangle \tau^2 \quad (28)$$

where $\langle w^2 \rangle$ is the 3D variance of the particle relative velocity at time 0. Note that the particle relative speed is actually what our model aims to predict. Therefore, the dependence of $d(\tau)$ on $\langle w^2 \rangle$ in the ballistic phase leads to an implicit equation for the particle relative velocity (see §3.2.4).

Bec et al. (2010) also showed that, after a friction timescale, the dispersion of inertial particles with $\tau_p \lesssim T_L$ makes a transition to a tracer-like phase. In this phase, the particle distance is in the inertial range of the flow, and, like tracer particles, the separation variance increases as time cubed, a behavior known as the Richardson’s law. The Richardson behavior was found in the pair dispersion of tracer particles both forward and backward in time (Berg et al. 2006; see Appendix A). It is thus likely to exist also in the backward separation of inertial particles, and we expect it to connect to the ballistic phase at $\tau \simeq -\tau_p$. We therefore apply the Richardson’s law for $\tau \lesssim -\tau_p$,

$$d^2(\tau) \simeq g\bar{\epsilon}|\tau|^3 \quad (29)$$

where g is called the Richardson constant and $\bar{\epsilon}$ is the average dissipation rate of the flow. Bec et al. (2010) did not report the value of g in the Richardson phase of inertial particle pair dispersion. As in PP10, we will take g as a parameter. We will measure g for the backward dispersion of tracer particles in our simulated flow (see Appendix A), and take the measured value as a reference. In our model, we will use a combined separation behavior that connects a ballistic phase and a Richardson phase at $\tau \simeq -\tau_p$.

The Richardson behavior would end when the separation becomes much larger than the integral length scale, L , of the turbulent flow. At such a large distance, the flow velocities “seen” by the two particles is uncorrelated, and the separation of the particle pair is expected to be diffusive like in a random walk. It is thus appropriate to switch the Richardson behavior to a diffusive phase with $d^2(\tau) \propto |\tau|$ at a separation $d \gtrsim L$. However, we find that the exact separation behavior at $d \gg L$ (or $R \gg L$) does not affect the prediction of our model. This is because at these large scales both the structure functions, S_{11} and S_{22} , and the timescale, $T(d)$ (or $T(R)$), become independent of d (or R). Therefore, eq. (19) (or eq. (20)) does not depend on the behavior of the separation once

it becomes much larger than L . This is confirmed by the numerical solutions of eqs. (19) and (20). For convenience, we keep using the Richardson’s law even after d exceeds L .

The separation behavior discussed above is based on the simulation results of Bec et al. (2010) for particles in the inertial range. For simplicity, we will use the same behavior for all particles, although its validity is questionable for small ($\tau_p \lesssim \tau_\eta$) and large ($\tau_p \gtrsim T_L$) particles. For small particles with $St \lesssim 1$, a ballistic phase is not clearly observed in the d^2 vs. time plots shown in Fig. 5 of Bec et al. (2010). We expect that a short ballistic phase is likely to exist if one plots $(d^2 - r^2)$ (instead of d^2) vs. time (see Fig. 17 in Appendix A for the $(d^2 - r^2)$ vs. time plot for tracer particle pairs). But the connection of this short ballistic phase to the Richardson behavior appears to be less clear than in the case of larger particles (Fig. 5 of Bec et al. 2010). Fortunately, the relative velocity of $St \ll 1$ particles is mainly contributed by the local flow velocity and does not have a strong dependence on the backward separation. With the assumed behavior, our model does give acceptable prediction for small particles.

The problem of using the assumed behavior for particles with $\tau_p \gg T_L$ is that the Richardson phase does not exit. The velocities of these large particles are uncorrelated even at small distances (§3.1). Therefore, at timescales larger than τ_p , the separation is likely diffusive, i.e., $d(\tau) \propto |\tau|$. Realistically, one needs to connect the ballistic phase to a diffusive behavior rather than a Richardson law at $|\tau| \sim \tau_p$. However, it turns out that, at the end of the ballistic phase of these particles, the separation is already $\gtrsim L$. As discussed earlier, once the separation exceeds L , the exact separation behavior would not significantly affect the model prediction. This justifies using a combined separation behavior with a ballistic and a Richardson phase also for $\tau_p \gg T_L$ particles.

So far, in our assumption the initial distance, r , just provides a floor value for the separation d (eq. (28)). It is, however, possible that the value of r has additional effects on the separation behavior. Bec et al. (2010) only explored initial distances r above the Kolmogorov scale, and it is not clear whether the separation behavior has a qualitative difference if $r \lesssim \eta$. In our model for the particle collision speed, we are interested in the backward separation with $r \lesssim \eta$, and it would thus be helpful to systematically investigate whether and how the separation behavior changes as r decreases below η . We defer such a study to a later work. In this paper, we assume that the two-phase behavior discussed above applies for any r .

To constrain g in the Richardson phase, in Appendix A we measure g for the backward dispersion of tracer particle pairs in our simulated flow, which is used as a reference for inertial particles. The measured g for tracers in our flow at a limited resolution shows a dependence on r , suggesting that the Richardson constant for inertial particles may also depend on r . When comparing our model prediction to the simulation data for the particle relative velocity at different r , we will adjust g to obtain best fits, and examine whether the best-fit values are consistent with the range of g measured from tracer particles. The Richardson constant for inertial particles

may also have a dependence on τ_p (or St), which will be ignored for simplicity.

3.2.4. Qualitative Behavior of Our Model Prediction

Our model for the particle structure tensor, S_{pij} , is now complete. Here we discuss the qualitative behavior of our model prediction for the particle relative velocity. We start by considering the 3D variance, $\langle w^2 \rangle$. The contraction of eq. (19) gives,

$$\langle w^2 \rangle = \int_{-\infty}^0 \frac{d\tau}{\tau_p} \int_{-\infty}^0 \frac{d\tau'}{\tau_p} [S_{ll}(R) + 2S_{nn}(R)] \times \Phi_2(\tau' - \tau, R) \exp\left(\frac{\tau}{\tau_p}\right) \exp\left(\frac{\tau'}{\tau_p}\right), \quad (30)$$

which is an implicit equation of $\langle w^2 \rangle$ because R depends on $\langle w^2 \rangle$ in the ballistic separation phase. In §6.1, we solve the equation numerically using an iteration method.

The qualitative behavior of the model prediction for $\langle w^2 \rangle$ can be obtained by analyzing the integrand in eq. (30). In the S-T limit ($\tau_p \rightarrow 0$), the exponential cutoff terms, $\frac{1}{\tau_p} \exp(\tau/\tau_p)$ and $\frac{1}{\tau_p} \exp(\tau'/\tau_p)$, in the integrand can be viewed as delta functions at $\tau = 0$ and $\tau' = 0$, respectively. This suggests that $\langle w^2 \rangle$ is approximately given by $\simeq (S_{ll} + 2S_{nn})$ at $R(0, 0)$. Since $R(0, 0) = r$, we have $\langle w^2 \rangle = \frac{\epsilon}{3\nu} r^2$ for r in the dissipation rate, which is consistent with the 3D variance of the relative velocity from the S-T formula, eq. (11).

The analysis of eq. (30) for larger particles is more complicated. We first note that $S_{ll}(R)$, $S_{nn}(R)$, and the timescale $T(R)$ in the correlation function Φ_2 are all increasing functions of R . Since R increases backward in time, the first factor in the integrand of eq. (30) increases with increasing $|\tau|$ and $|\tau'|$. A larger $T(R)$ also tends to increase the integral because Φ_2 would allow contributions from a broader range of time lag ($\Delta\tau$). Together with the exponential cutoffs, these suggest that the contribution to the integral peaks at $\tau, \tau' \simeq -\tau_p$. We denote the particle separation at $\tau = \tau' = -\tau_p$ as R_p ($\equiv R(-\tau_p, -\tau_p)$), and refer to it as the primary distance. The primary distance provides useful insights to the prediction of our model.

In the extreme limit of large particles with $\tau_p \gg T_L$, R_p is expected to be much larger than the integral scale, L , of the flow. We thus have $S_{ll} = S_{nn} = 2u'^2$, and $T(R_p) = T_L$ at R_p (see eqs. 8, 33 and 23). The exponential cutoff by Φ_2 indicates that only the time pairs (τ and τ') that satisfy the constraint $|\tau' - \tau| \simeq T_L$ give a significant contribution to the integral. Since $T_L \ll \tau_p$, Φ_2 reduces the range of τ and τ' that contributes to the integral by a factor of T_L/τ_p . Assuming the main contribution to the integral is from $R \simeq R_p$ and accounting for the effect of Φ_2 , we find that $\langle w^2 \rangle \simeq 6u'^2 T_L/\tau_p$. This is consistent with eq. (12), meaning that our model correctly reproduces the large particle limit.

We next discuss inertial-range particles with $\tau_\eta \lesssim \tau_p \lesssim T_L$. For these particles, the primary distance, R_p , corresponds to inertial-range scales of the turbulent flow. Using the Kolmogorov scaling gives $S_{ll}, S_{nn} \propto R_p^{2/3}$ and $T(R_p) \propto R_p^{2/3}$. From its definition, R_p is roughly the particle distance at the time when the ballistic phase connects to the Richardson

phase (see §3.2.3). We can thus assume that R_p is determined by a ballistic separation of duration τ_p , i.e., $R_p \simeq \langle w^2 \rangle^{1/2} \tau_p$. The effect of the Φ_2 term depends on how $T(R_p)$ compares to τ_p . If $T(R_p) > \tau_p$, Φ_2 is $\simeq 1$ for all time pairs in the range $-\tau_p \lesssim \tau, \tau' \lesssim 0$. On the other hand, if $T(R_p) < \tau_p$, Φ_2 provides a factor of $T(R_p)/\tau_p$, which follows from the argument used above for the large particle limit. We consider both cases and show that they actually lead to the same scaling of $\langle w^2 \rangle$ with τ_p . In the first case, eq. (30) is approximated by $\langle w^2 \rangle \simeq [S_{ll}(R_p) + S_{nn}(R_p)] \propto R_p^{2/3}$. With $R_p \simeq \langle w^2 \rangle^{1/2} \tau_p$, we obtain $\langle w^2 \rangle^{1/2} \propto \tau_p^{1/2}$. In the second case with $T(R_p) < \tau_p$, we include a factor of $T(R_p)/\tau_p$ and estimate $\langle w^2 \rangle$ as $\simeq [S_{ll}(R_p) + S_{nn}(R_p)] T(R_p)/\tau_p \propto R_p^{4/3}/\tau_p$. It is straightforward to see that setting $R_p \simeq \langle w^2 \rangle^{1/2} \tau_p$ in this estimate gives the same scaling, $\langle w^2 \rangle^{1/2} \propto \tau_p^{1/2}$, as the first case. Therefore, whether $T(R_p)$ is larger or smaller than τ_p , our model predicts a $\tau_p^{1/2}$ (or $St^{1/2}$) scaling for inertial-range particles.

Using a similar argument, PP10 found that if the primary distance is determined by the Richardson's law, $R_p \simeq (g\epsilon\tau_p^3)^{1/2}$, the model also predicts a $St^{1/2}$ scaling for particles in the inertial range. Since both the ballistic and Richardson behaviors yield a $St^{1/2}$ scaling, a combination of a ballistic and a Richardson phase produces the same scaling (PP10). The $St^{1/2}$ scaling has also been predicted by models of Volk et al. (1980), Cuzzi and Hogan (2003), Ormel and Cuzzi (2007), and Zaichik & Alipchenkov (2003). The derivation of the $St^{1/2}$ scaling in all the models assumes a sufficiently broad inertial range in the turbulent flow. The scaling would not exist if the Reynolds number of the flow is low. In fact, the predicted $St^{1/2}$ behavior has never been confirmed by simulations due to the low numerical resolution. PP10 showed that, to see the $St^{1/2}$ scaling, the Taylor Reynolds number of the turbulent flow must be larger than $\simeq 300$. This is higher than in the 512³ simulation used in the present study, and thus the $St^{1/2}$ scaling is not observed. It appears likely that the existence of this scaling can be verified at a twice larger resolution. We will conduct a 1024³ simulation in a future work.

The above analysis for the scaling behavior of $\langle w^2 \rangle$ in different St ranges can be similarly applied to the simplified model, eqs. (20) and (21). The prediction of the simplified model is qualitatively the same as the original PP10 model.

Finally, we examine the model prediction for the radial and tangential components of the relative velocity. The prediction for $\langle w_r^2 \rangle$ and $\langle w_t^2 \rangle$ depends on the angular average of S_{Tij} in eq. (19) (or eq. 20). In §3.3.2, we made two assumptions, eqs. (26) and (27), for the angular average, and we discuss them separately. Inserting the first assumption, eq. (26), into eq. (19) and comparing it with eq. (10), we find,

$$\langle w_r^2 \rangle = \int_{-\infty}^0 \frac{d\tau}{\tau_p} \int_{-\infty}^0 \frac{d\tau'}{\tau_p} \left[\left(\frac{1}{3} + \frac{2r^2}{3R^2} \right) S_{ll}(R) + \left(\frac{2}{3} - \frac{2r^2}{3R^2} \right) S_{nn}(R) \right] \exp\left(\frac{\tau}{\tau_p}\right) \exp\left(\frac{\tau'}{\tau_p}\right),$$

$$\langle w_t^2 \rangle = \int_{-\infty}^0 \frac{d\tau}{\tau_p} \int_{-\infty}^0 \frac{d\tau'}{\tau_p} \left[\left(\frac{1}{3} - \frac{r^2}{3R^2} \right) S_{ll}(R) + \left(\frac{2}{3} + \frac{r^2}{3R^2} \right) S_{nn}(R) \right] \exp\left(\frac{\tau}{\tau_p}\right) \exp\left(\frac{\tau'}{\tau_p}\right). \quad (31)$$

In order to integrate the two equations, one needs to first solve eq. (30) for $\langle w^2 \rangle$ due to the dependence of R on $\langle w^2 \rangle$ in the ballistic phase. It is easy to show that, in the limit $\tau_p \rightarrow 0$, $R \rightarrow r$, and eq. (31) reduces to $\langle w_r^2 \rangle = S_{ll}(r)$ and $\langle w_t^2 \rangle = S_{nn}(r)$, reproducing the Saffman-Turner formula, eq. (11). For larger particles with $\tau_p \gg \tau_\eta$, $R_p \gg r$ and thus eq. (31) predicts that $\langle w_r^2 \rangle = \langle w_t^2 \rangle = \frac{1}{3} \langle w^2 \rangle$. Therefore, both $\langle w_r^2 \rangle$ and $\langle w_t^2 \rangle$ scale as $St^{1/2}$ for inertial-range particles and as $St^{-1/2}$ in the large particle limit.

As discussed in §3.3.2, the second assumption, eq. (27), for the angular average of S_{Tij} predicts that $\langle w_r^2 \rangle = \langle w_t^2 \rangle = \frac{1}{3} \langle w^2 \rangle$ for all particles. In the small particle limit, eq. (30) predicts $\langle w^2 \rangle = \frac{\epsilon}{3\nu} r^2$, and thus $\langle w_r^2 \rangle = \langle w_t^2 \rangle = \frac{\epsilon}{9\nu} r^2$. This means that the prediction for the radial and tangential relative velocity of small particles by the second assumption differs from the S-T formula, although it reproduces the S-T prediction for the 3D rms. We will test the two assumptions against our simulation data.

4. STATISTICS OF THE SIMULATED FLOW

In this section, we describe the numerical method used in our simulation and discuss the statistical properties of the simulated flow. Our simulation was conducted in a periodic 512^3 box with a length of 2π on each side. Using the Pencil code⁵ (Brandenburg & Dobler 2002, Johansen, Andersen, & Brandenburg 2004), we evolved the hydrodynamic equations,

$$\begin{aligned} \frac{\partial \rho}{\partial t} + \frac{\partial}{\partial x_i} (\rho u_i) &= 0, \\ \frac{\partial u_i}{\partial t} + u_j \frac{\partial u_i}{\partial x_j} &= \frac{1}{\rho} \frac{\partial}{\partial x_j} \left[\rho \nu \left(\frac{\partial u_i}{\partial x_j} + \frac{\partial u_j}{\partial x_i} - \frac{2}{3} \delta_{ij} \frac{\partial u_k}{\partial x_k} \right) \right] \\ &\quad - \frac{1}{\rho} \frac{\partial p}{\partial x_i} + f_i, \end{aligned} \quad (32)$$

with an isothermal equation of state, $p = \rho C_s^2$. The sound speed is set to unity, i.e., $C_s = 1$. The kinematic viscosity, ν , is taken to be constant, $\nu = 5 \times 10^{-5}$. A large-scale force, f_i , generated in Fourier space with wave numbers in the range $1 \leq k \leq 2$ is applied to drive and maintain the turbulent flow. The driving length scale, L_f , is thus about 1/2 box size. The balance between the energy input by the driving force and the dissipation by viscosity leads to a statistical steady state with a 1D rms velocity, u' , of 0.05, or a 3D rms of 0.085. This weakly compressible flow is suitable for the application to turbulence in protoplanetary disks. At an rms Mach number of 0.085, the flow statistics is essentially the same as incompressible turbulence (Padoan et al. 2004, Pan & Scannapieco 2011).

The integral length scale, L , in our simulated flow is found to be $\simeq 1$, i.e., about 1/6 box size. It is about 3 times smaller than the driving length scale, L_f . The integral scale, L , represents the (longitudinal) correlation

length of the velocity field, and we computed it from the energy spectrum, $E(k)$, of the flow, using the relation $L = \frac{\pi}{2u'^2} \int k^{-1} E(k) dk$ (Monin & Yaglom 1975). The energy spectrum, $E(k)$, is plot in the inset of Fig. (3). With $L = 1$, the large-eddy turnover time is $T_{\text{eddy}} = L/u' = 20$ in units in which the sound crossing time is 2π .

The average energy dissipation rate per unit volume by the viscosity term is given by $\bar{\epsilon} = \frac{1}{2\bar{\rho}} \langle \rho \nu (\partial_i u_j + \partial_j u_i - \frac{2}{3} \delta_{ij} \partial_k u_k)^2 \rangle$, where $\bar{\rho}$ is the average density. In our weakly compressible flow, the density fluctuations and the velocity divergence can be neglected, and the average dissipation rate can be estimated by $\bar{\epsilon} = \nu \langle \omega^2 \rangle$, where $\langle \omega^2 \rangle$ is the vorticity variance. We find that $\langle \omega^2 \rangle = 0.92$, implying that $\bar{\epsilon} \simeq 4.6 \times 10^{-5}$. We also evaluated the dissipation rate from the 3rd-order longitudinal structure function using Kolmogorov's 4/5 law, $\langle \Delta u_r(\ell)^3 \rangle = -\frac{4}{5} \bar{\epsilon} \ell$, for ℓ in the inertial range. This latter method gives a larger dissipation rate, $\bar{\epsilon} = 5 \times 10^{-5}$, suggesting that a small fraction, $\simeq 8\%$, of kinetic energy is dissipated by numerical diffusion. The effective viscosity is thus larger than the adopted value by the same amount. We take the effective viscosity to be 5.4×10^{-5} and use it in our estimates of the Kolmogorov scales. We compute the Kolmogorov timescale from the vorticity variance as $\tau_\eta = \langle \omega^2 \rangle^{-1/2} = 1.04$. The Kolmogorov length scale is estimated to be $\eta = (\nu^3/\bar{\epsilon})^{1/4} = 0.0075$, which corresponds to $\simeq 0.6$ cell size of the computation grid. The Kolmogorov velocity scale is $u_\eta = (\nu \bar{\epsilon})^{1/4} = 0.0072$ in units of the sound speed.

The Reynolds number of our simulated flow is $Re \equiv u' L / \nu \simeq 1000$. A more commonly-used Reynolds number in turbulence studies is the Taylor Reynolds number, $Re_\lambda \equiv u' \lambda / \nu$, based on the Taylor micro length scale, λ . The Taylor length scale is defined as $\lambda \equiv (15 u'^2 / \langle \omega^2 \rangle)^{1/2}$. We find that $\lambda = 0.2$ in our simulated flow, and thus the Taylor Reynolds number $Re_\lambda \simeq 200$. From their definitions, we have $u' / u_\eta = (Re_\lambda / \sqrt{15})^{1/2}$, which is useful for normalizations.

4.1. The Lagrangian Correlation Function and the Timescales

To study the Lagrangian statistics, we integrated the trajectories of 33.6 million tracer particles with zero inertia in the simulated flow. The total number of tracer particles corresponds to an average number density of 1 particle per 4 computational cells. To obtain the particle velocity inside a cell, we selected the triangular-shaped-cloud interpolation method already implemented in the Pencil code (Johansen and Youdin 2007). We output the particle positions to a data file in each time interval of $0.1\tau_\eta$. The Lagrangian correlation function, $\Phi_L(\Delta\tau)$, is computed as the average of the velocity correlation, $\langle u_i(\mathbf{X}(t), t) u_i(\mathbf{X}(t + \Delta\tau), t + \Delta\tau) \rangle / 3u'^2$, along the trajectories, $\mathbf{X}(t)$, of all particles. We considered both positive and negative time lags $\Delta\tau$, corresponding to Lagrangian trajectories forward and backward in time, respectively. Our data confirmed that Φ_L is an even function of $\Delta\tau$, as expected from statistical stationarity (see §2). We find that the Lagrangian correlation timescale, $T_L (\equiv \int \Phi_L(\Delta\tau) d\Delta\tau)$, is $\simeq 15$, which is about 0.75 eddy turnover time, T_{eddy} . This is consistent with the simula-

⁵ <http://pencil-code.nordita.org>

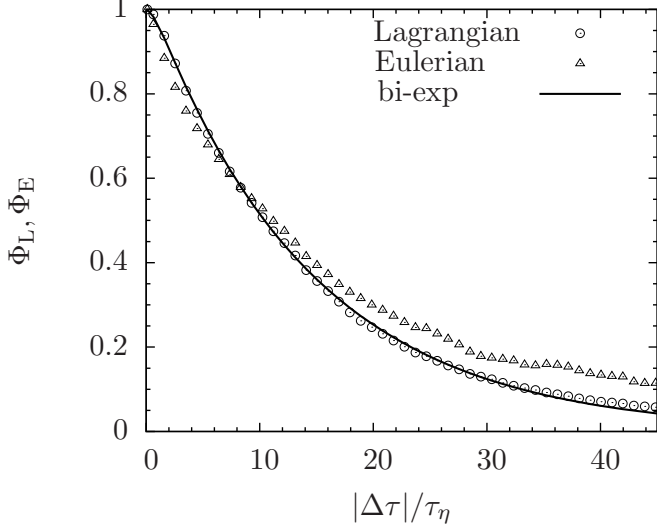


FIG. 2.— Lagrangian (Φ_L ; circles) and Eulerian (Φ_E ; triangles) temporal correlation functions in our simulated flow. The time lag, $\Delta\tau$, is normalized to the Kolmogorov timescale, τ_η . The solid line shows the best fit for Φ_L using the bi-exponential function, eq. (5).

tion result of Yeung et al. (2006). Since $\tau_\eta = 1.04$ in our simulated flow, we have $T_L = 14.4\tau_\eta$.

The Lagrangian correlation, Φ_L , in our flow is plot as circles in Fig. 2, where the time lag, $|\Delta\tau|$, is normalized to the Kolmogorov timescale, τ_η . The solid line shows the bi-exponential function, eq. (5), given in §2. The parameter z is set to 0.3, which suggests that the Taylor micro timescale, τ_T , is $\simeq 4.3\tau_\eta$. This value of τ_T corresponds to an acceleration variance, $a^2 \simeq 5.2(u_\eta/\tau_\eta)^2$. The bi-exponential function matches very well the simulation data. On the other hand, we find that a single exponential function could not give a satisfactory fit to Φ_L .

We also considered the Eulerian temporal correlation function, $\Phi_E(\Delta\tau)$, in the simulated flow. It is computed as the average, $\langle u_i(\mathbf{x}, t)u_i(\mathbf{x}, t + \Delta\tau) \rangle / 3u'^2$, over all grid points \mathbf{x} . The result is plot as triangles in Fig. 2. $\Phi_E(\Delta\tau)$ is also symmetric about $\Delta\tau = 0$. As seen in Fig. 2, Φ_E is smaller than the Lagrangian correlation Φ_L at small time lags, and then becomes larger at $|\Delta\tau| \gtrsim 8\tau_\eta \simeq 0.5T_L$. Due to the slower decrease of Φ_E at large time lags, the Eulerian correlation time, $T_E \equiv \int \Phi_E(\Delta\tau)d\Delta\tau$, is slightly (10%) larger than T_L . We find that $T_E = 15.9\tau_\eta$. The Eulerian correlation function is of interest for large inertial particles with $\tau_p \gg T_L$. Due to their large inertia, these particles have small velocities and thus may stay around as the flow sweeps by. Therefore, unlike small particles, the temporal series of the flow velocity “seen” by the large particles may be better described by the Eulerian velocity. This suggests that, for $\tau_p \gtrsim T_L$, it may be appropriate to replace the Lagrangian correlation used in our model by the Eulerian correlation. However, the Eulerian correlation function and timescale are quite close to the Lagrangian ones, and using the Lagrangian correlation for all particles in our model gives satisfactory predictions for the 1-particle velocity and the 2-particle relative velocity at any value of St (§5 and §6.1).

We give a brief summary of the relevant timescales in the simulated flow. We list them in an increasing or-

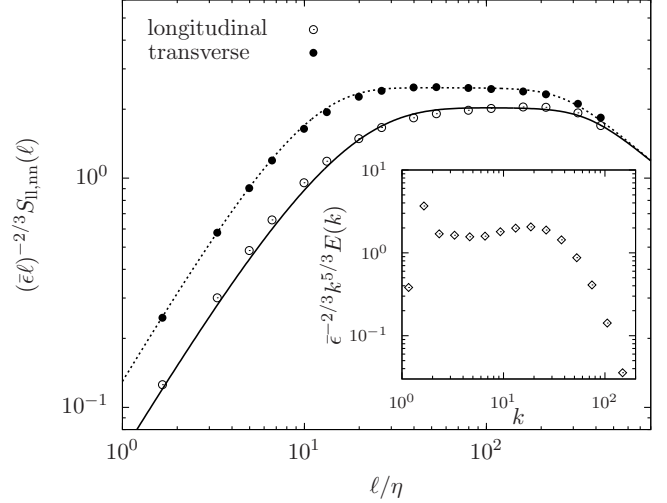


FIG. 3.— Longitudinal (open circles) and transverse (filled circles) structure functions measured in our simulated flow. The structure functions are compensated by the Kolmogorov scaling in the inertial range. The solid and dashed lines are fitting functions, eqs. (8) and (33), for S_{ll} and S_{nn} , respectively. The inset shows the energy spectrum of the simulated flow, compensated by $\epsilon^{2/3}k^{-5/3}$.

der. The smallest timescale is the Kolmogorov timescale τ_η , and we use it as a reference timescale. The Taylor micro scale, τ_T , was found to be $4.3\tau_\eta$ from the bi-exponential fit for the Lagrangian correlation function. The next timescale is the Lagrangian correlation time, T_L , which is $14.4\tau_\eta$. The Eulerian correlation time is slightly larger, $T_E \simeq 15.9\tau_\eta$. The large eddy turnover time, T_{eddy} , was measured to be $\simeq 19.2\tau_\eta$. Another commonly-used timescale is the dynamical time, τ_{dyn} , defined as the forcing length scale, L_f , divided by the 3D rms velocity ($\sqrt{3}u'$). We find that $\tau_{\text{dyn}} = 35\tau_\eta$.

4.2. The Flow Structure Functions and Energy Spectrum

In Fig. 3, we show the longitudinal (S_{ll} ; open circles) and transverse (S_{nn} ; filled circles) structure functions in our simulated flow. The structure functions are measured from the velocity differences along the 3 directions, \mathbf{e}_1 , \mathbf{e}_2 and \mathbf{e}_3 , of the simulation grid. For $S_{ll}(\ell)$, we computed and averaged the variances of $\Delta u_{11}(\ell) (\equiv u_1(\mathbf{x} + \ell\mathbf{e}_1) - u_1(\mathbf{x}))$, $\Delta u_{22}(\ell)$ and $\Delta u_{33}(\ell)$ over all the grid points, \mathbf{x} . Similarly, $S_{nn}(\ell)$ is obtained by averaging the variances of $\Delta u_{12}(\ell) (\equiv u_1(\mathbf{x} + \ell\mathbf{e}_2) - u_1(\mathbf{x}))$, $\Delta u_{13}(\ell)$, $\Delta u_{21}(\ell)$, $\Delta u_{23}(\ell)$, $\Delta u_{31}(\ell)$ and $\Delta u_{32}(\ell)$.

As discussed earlier, Kolmogorov’s similarity theory predicts that $S_{ll}(\ell) \simeq C_K(\bar{\epsilon}\ell)^{2/3}$ for ℓ in the inertial range. We thus compensated the structure functions by $(\bar{\epsilon}\ell)^{2/3}$ in Fig. 3. A limited inertial range is seen in both S_{ll} and S_{nn} . Clearly, the Kolmogorov constant C_K is about 2. In this range, the scaling exponent for S_{ll} is found to be slightly larger than $2/3$, while the slope of S_{nn} is close to $2/3$. The ratio of the two structure functions in the inertial range is about 1.25, slightly smaller than the value, $4/3$, expected from the incompressibility condition (see §3). This is perhaps because our flow is weakly compressible. Another possible reason is that the inertial range is too short to allow an accurate measurement of this ratio. Both structure functions become smooth, i.e., $\propto \ell^2$, as ℓ decreases toward the Kolmogorov

scale, and approach $2u'^2$ in the limit $\ell \gg L$ (§3).

The solid line in Fig. 3 is the connecting formula, eq. (8), for S_{\parallel} (§3). We set C_K to 2 in the formula. The line gives a fairly good fit to the data points. As discussed in §3, with the connecting formula for S_{\parallel} , one may obtain a fitting function for S_{nn} using the incompressibility relation $S_{nn} = S_{\parallel} + \frac{1}{2}\ell dS_{\parallel}/d\ell$. However, the fitting function obtained this way overestimates the data points for S_{nn} in the inertial range, perhaps because the incompressibility condition does not exactly hold in our flow (see above). For a more accurate fitting function, we adopted a separate connecting formula for S_{nn} ,

$$S_{nn} = 2u'^2 \left[1 - \exp \left(-\frac{(\ell/\eta)^{4/3}}{(15C_{Kn}/2)} \right) \right] \times \left[\frac{(\ell/\eta)^4}{(\ell/\eta)^4 + (2u'^2/C_{Kn}u_\eta^2)^6} \right]^{1/6}, \quad (33)$$

where C_{Kn} is the scaling coefficient for S_{nn} in the inertial range. This connecting formula correctly reproduces the scaling behaviors of S_{nn} in different scale ranges. Its form is slightly different from eq. (8) for S_{\parallel} . The dotted line in Fig. 3 corresponds to eq. (33) with $C_{Kn} \simeq 1.25C_K = 2.5$. We will use eqs. (8) and (33) in the computation of our model prediction for the particle relative velocity.

The inset of Fig. 3 show the energy spectrum, $E(k)$, of our flow. The Kolmogorov theory predicts $E(k) = K\epsilon^{2/3}k^{-5/3}$ in the inertial range, and we compensated the spectrum by $\epsilon^{2/3}k^{-5/3}$. The power-law range ($3 \leq k \leq 10$) in the spectrum appears to be shorter than in the structure functions. The constant K is measured to be $\simeq 1.7$, consistent with previous studies (Ishihara et al. 2009). It is also consistent with the relation $K = 0.76C_K$ (Monin & Yaglom 1975), as the Kolmogorov constant, C_K , for S_{\parallel} was found to be $\simeq 2$.

5. ONE-PARTICLE ROOT-MEAN-SQUARE VELOCITY

In our simulation, we included 14 species of inertial particles of different sizes. The friction timescale of the particles spans about four decades from $\simeq 0.1\tau_\eta$ to $54T_L$ ($\simeq 800\tau_\eta$), covering the entire scale range of the simulated flow. The friction timescale is equally spaced, increasing by a factor of two in each successive species. The number of particles contained in each species is 33.6 million, which is the same as the tracer particles used in the study of Lagrangian statistics (§4.1), corresponding to an average particle density of one per 4 computational cells. Similar to the integration of the tracer particle trajectories, when evolving the equation of motion (eq. 1) for inertial particles, we adopted the triangular-shaped-cloud method to interpolate the flow velocity. Our simulation run lasted for about $35T_L$, which is much larger than the friction timescale of all particles except the largest ones with $\tau_p \simeq 27$ and $54T_L$. The dynamics of all particles in the first 12 species ($\tau_p \lesssim 14T_L$) is thus fully relaxed by the end of the simulation, and we measured the statistics of the particle velocity using the last few snapshots covering $5 - 6 T_L$. On the other hand, it is uncertain whether the largest particles from the last two species are well relaxed. From the analysis of our simulation data, we find that the velocity statistics of the largest particles do reach a steady state toward the end of the run, suggesting that these particles may also be

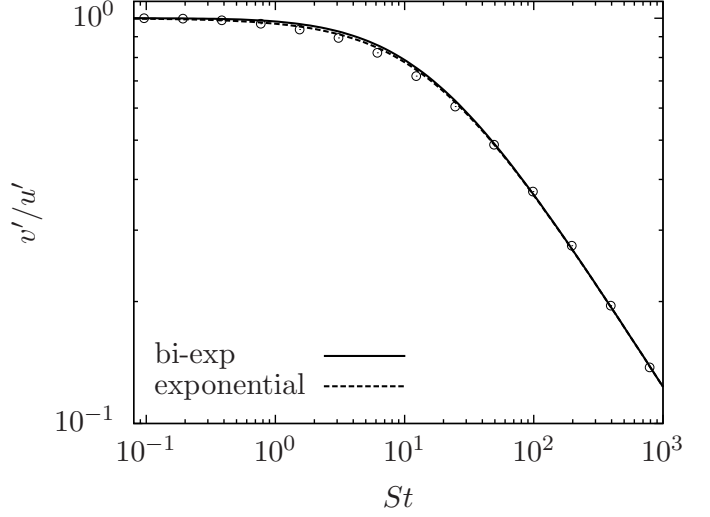


FIG. 4.— One-particle rms velocity, v' , as a function of the Stokes number, St . The data points show the simulation data. The dotted and solid lines are the predictions, eq. (4) and eq. (6), of our model using single- and bi-exponential forms for the temporal correlation function, respectively. In both cases, T_L is set to $15.4\tau_\eta$, and the parameter z in the bi-exponential case is set to 0.3.

dynamically relaxed.

In Fig. 4, we show our simulation result for the 1D rms particle velocity, v' , as a function of the Stokes number, St . We normalized v' by the flow rms velocity, u' . The dotted and solid lines are predictions, eq. (4) and eq. (6), of our model using single- and bi-exponential forms for the temporal correlation function, respectively. As discussed in §2, the model approximates the trajectory correlation function, Φ_1 , by the Lagrangian correlation function, Φ_L . For the bi-exponential case, we set the parameter $z = 0.3$, which best fits Φ_L measured from the Lagrangian trajectories of tracer particles (see §4.1). The two lines almost coincide, indicating that the model prediction for v' is insensitive to the exact form of the correlation function, and depends essentially only on the correlation timescale⁶. In both curves, we set $T_L = 15.4\tau_\eta$, generally consistent with the directly measured value of $14.4\tau_\eta$ (see §4.1).

As discussed in §4.1, the flow velocity “seen” by the large particles with $\tau_p \gtrsim T_L$ may be closer to Eulerian than Lagrangian, and thus using Φ_L for the trajectory correlation Φ_1 is physically not well justified (§2). However, the assumption is validated by our simulation data for all particles. This is because, first, based on our model prediction, v' is controlled mainly by the correlation time, not by the exact shape of the correlation function, and, second, the Eulerian correlation timescale, T_E , is close to T_L . Therefore, whether Φ_1 is better described by the Eulerian correlation function Φ_E or Φ_L , the 1-particle rms velocity would be essentially the same, justifying using Φ_L for all particles. We point out that

⁷ Unlike the case of the 1-particle velocity, the choice of Φ_1 is crucial for predicting the relative velocity between different particles in the S-T limit (PP10). In that case, adopting the bi-exponential form of Φ_L for Φ_1 is needed to reproduce the acceleration contribution to the relative velocity, while a single exponential form cannot correctly capture the effect of the flow acceleration on Φ_L at small time lags.

the best-fit correlation timescale, $15.4\tau_\eta$, in Fig. 4 is actually in between the measured values of T_L ($14.4\tau_\eta$) and T_E ($15.9\tau_\eta$). This suggests that the temporal correlation of the flow velocity “seen” by a large particle is likely in between that along a Lagrangian trajectory and that at a fixed Eulerian point. It is interesting to note that, even though a single-exponential function does not fit well either Φ_E or Φ_L (§4.1), our model prediction with an exponential correlation is in good agreement with the simulation result for the 1-particle rms velocity.

We also computed the probability distribution function of the 1-particle velocity. The velocity of small particles is expected to be Gaussian because it simply samples the 1-point PDF of the flow velocity, which is close to Gaussian. The velocity of large particles with $\tau_p \gg T_L$ would also be Gaussian because their equation of motion is essentially a Langevin equation. We find the 1-particle velocity PDF is actually nearly Gaussian at all St . The far PDF tails are slightly thinner than Gaussian probably due to the sub-Gaussian tails of the flow velocity and/or the insufficient sample size at high tails.

6. THE RELATIVE VELOCITY OF INERTIAL PARTICLES

We finally explore the statistics of the relative velocity of inertial particles in our simulation, focusing on the monodisperse case with identical particles. For each species (St), we measure the relative velocity of particle pairs at three given distances, $r = 1\eta$, 0.5η and 0.25η . A study of smaller values of r is desirable, as the size of dust particles in protoplanetary disks is much smaller than the Kolmogorov scale. However, at smaller r , the number of particle pairs available in our simulation becomes more limited and does not allow accurate statistical analysis. For each St and r , we search the simulation box for all particle pairs in a distance shell from $r - \delta r$ to $r + \delta r$, with δr set to $0.01r$. We decompose the relative velocity, \mathbf{w} , of each selected particle pair into radial and tangential components, and then analyze their statistics separately.

To compute the radial and tangential components, we set up a local coordinate system (\mathbf{e}'_1 , \mathbf{e}'_2 and \mathbf{e}'_3) for each pair. The direction \mathbf{e}'_1 is chosen to coincide with the separation, \mathbf{r} , of the two particles. In terms of the unit base vectors, \mathbf{e}_1 , \mathbf{e}_2 and \mathbf{e}_3 , of the simulation grid, \mathbf{e}'_1 is expressed as $\cos\theta\cos\phi\mathbf{e}_1 + \cos\theta\sin\phi\mathbf{e}_2 + \sin\theta\mathbf{e}_3$, where $\sin\theta = r_3/r$, $\cos\theta = (r_1^2 + r_2^2)^{1/2}/r$, $\cos\phi = r_1/(r_1^2 + r_2^2)^{1/2}$, and $\sin\phi = r_2/(r_1^2 + r_2^2)^{1/2}$. The radial relative velocity is calculated as $w_r = \mathbf{w} \cdot \mathbf{e}'_1$. For the two tangential directions, we set $\mathbf{e}'_2 = -\sin\phi\mathbf{e}_1 + \cos\phi\mathbf{e}_2$ and $\mathbf{e}'_3 = -\sin\theta\cos\phi\mathbf{e}_1 - \sin\theta\sin\phi\mathbf{e}_2 + \cos\theta\mathbf{e}_3$, which are obtained by two consecutive rotations of the original coordinates. The first rotation is about \mathbf{e}_3 by ϕ , which moves \mathbf{e}_2 to \mathbf{e}'_2 , and the second rotation is about \mathbf{e}'_2 by $-\theta$, which further brings the original base vectors \mathbf{e}_1 and \mathbf{e}_3 to \mathbf{e}'_1 and \mathbf{e}'_3 . We calculate the tangential components of the relative velocity \mathbf{w} as $w_{t2} = \mathbf{w} \cdot \mathbf{e}'_2$ and $w_{t3} = \mathbf{w} \cdot \mathbf{e}'_3$. The PDFs of w_{t2} and w_{t3} are found to be almost the same, as expected from the statistical isotropy⁸. We thus take the PDF of a tangential component, w_t , to be the average PDF of w_{t2} and w_{t3} . The

variance of w_t is calculated as $\langle w_t^2 \rangle = \frac{1}{2} (\langle w_{t2}^2 \rangle + \langle w_{t3}^2 \rangle)$. We discuss the measured statistics of w_r , w_t and the 3D amplitude $|\mathbf{w}|$ in the following sections.

6.1. The Root-mean-square Relative Speed

In Fig. 5, we show the simulation result for the 3D rms, $\langle w^2 \rangle^{1/2}$, of the relative velocity as a function of the Stokes number. The data points correspond to the measured relative velocity for particle pairs at a distance of 1η . We normalized the relative speed by the Kolmogorov velocity, u_η . One may easily convert the normalization to the rms flow velocity u' using the relation $u' = (Re_\lambda/\sqrt{15})^{1/2} u_\eta = 7u_\eta$. At small St , the 3D rms relative speed is roughly constant, and its value is consistent with the prediction, $\langle w^2 \rangle^{1/2} = u_\eta/\sqrt{3}$, of the S-T formula. The relative speed starts to rise at $St \simeq 1$, as the contribution from the backward separation of particle pairs becomes important. For the largest particles, we find that $\langle w^2 \rangle^{1/2} \simeq \sqrt{6}u'(T_L/\tau_p)^{1/2}$, with $T_L \simeq 14\tau_\eta$, in agreement with eq. (12) for the large particle limit, $\tau_p \gg T_L$. Like the earlier result for the 1-particle rms velocity, this provides a validation for using the Lagrangian correlation time for the trajectory correlation, Φ_1 , of large particles with $\tau_p \gg T_L$, even though their trajectories may significantly deviate from Lagrangian tracers. The predicted $St^{1/2}$ scaling for inertial-range particles by various models is not observed due to the limited inertial range of the simulated flow.

The solid curve in Fig. (5) is the prediction of the PP10 model, and it is obtained by numerically solving eq. (30) with an iteration method. We computed the trajectory structure tensor, S_{Tij} , using eq. (8) for S_{ij} , eq. (33) for S_{nn} , and eq. (23) for $T(\ell)$, respectively. The parameters used in these equations are $C_K = 2$, $C_{Kn} = 2.5$, $C_T = 0.4$ and $T_L = 14.4\tau_\eta$. A bi-exponential form, eq. (24), is adopted for the temporal correlation Φ_2 . We used a two-phase behavior for the particle separation backward in time (§3.4.3), connecting the ballistic and Richardson phases at $\tau_c = -\tau_p$. We set $d^2(\tau) = r^2 + \langle w^2 \rangle \tau^2$ for $\tau \geq \tau_c$, and then switch to the Richardson’s law, $d^2(\tau) = d^2(\tau_c) + g\bar{\epsilon}(|\tau|^3 - |\tau_c|^3)$, for $\tau < \tau_c$, where $d^2(\tau_c) = r^2 + \langle w^2 \rangle \tau_c^2$. To fit the simulation data, the Richardson constant, g , is set to 1.6. The solid line is in good agreement with the data points, confirming the validity of the physical picture of our model. Adopting a larger value for g could further improve the fitting quality at intermediate St .

In Appendix A, we investigated the backward separation of tracer particles in our simulated flow, and find that g is in the range $0.5 \lesssim g \lesssim 1.2$. Therefore, the g value used in the solid line in Fig. 5 is significantly larger than that for tracer particles. It is possible that the backward separation of inertial particles in the Richardson phase is indeed faster than tracers, which can be tested by a direct numerical study of inertial particle dispersion. Another possibility is that the accuracy of our model for the trajectory structure tensor, S_{Tij} , is inadequate. First, there are uncertainties in our estimate for the correlation timescale, $T(\ell)$, in Φ_2 . We associated the timescale with the eddy turnover time at the typical particle separation, $R(\tau, \tau')$, between τ and τ' . This approximation is likely not of high quantitative accuracy.

⁹ When selecting the local coordinate system, one may also perform a third rotation about \mathbf{e}'_1 by an arbitrary angle. This changes \mathbf{e}'_2 and \mathbf{e}'_3 . However, from the statistical isotropy, w_{t2} and w_{t3} would be statistically invariant with respect to this third rotation.

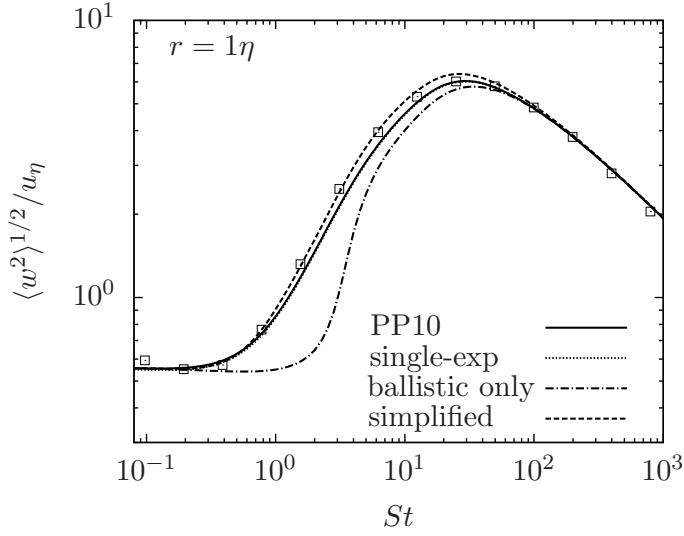


FIG. 5.— The 3D rms relative velocity, $\langle w^2 \rangle^{1/2}$, as a function of the Stokes number, St . The data points show the simulation result. The solid line is the prediction of the PP10 model (eq. 30) using a bi-exponential temporal correlation Φ_2 and a two-phase separation behavior with $g = 1.6$ in the Richardson phase. The dotted line corresponds to the same model but with a single-exponential Φ_2 . The line is barely visible because it almost coincides with the solid line. The dot-dashed line assumes ballistic separation at all times. The dashed line is the prediction of the simplified model, eqs. (20) and (21), using single-exponential Φ_2 and a two-phase separation behavior with $g = 1.0$.

At inertial-range scales, we set $T(\ell) = C_T \bar{\epsilon}^{-1/3} \ell^{2/3}$ with $C_T \simeq 0.4$. There may be an order-of-unity uncertainty in the estimated value of C_T . Our model prediction for intermediate St increases with C_T . If a larger value of C_T were adopted, we would obtain a good fit to the simulation data with a smaller value of g . Another uncertainty in our model for S_{Tij} is that we neglected the correlation between the particle distance, R , and the fluctuations in the flow velocity difference, $\Delta u(R)$, seen by the particle pair (see §3.2). This assumption tends to underestimate the relative velocity. Accounting for the correlation may lead to a better agreement of the model prediction with the data using a smaller value of g . In §6.3, we will show evidence for this correlation from our simulation result for the PDF of the particle relative velocity.

The dotted line in Fig. (5) is the prediction of the same PP10 model, but with a single-exponential form (eq. (22)) for Φ_2 . The dotted line is actually not distinguishable from the solid line, confirming the earlier statement in §3.2.1 that our model prediction for the relative speed is insensitive to the function form of Φ_2 . This leaves us some freedom for the choice of Φ_2 , as long as the correlation timescale is properly evaluated. In particular, it provides a justification for approximating Φ_2 by the same function form, e.g., the form of Φ_L , for all particles, although realistically the form of Φ_2 may have a dependence on the particle inertia.

The dot-dashed curve plots the prediction of the PP10 model assuming that the particle separation is ballistic with $d^2(\tau) = r^2 + \langle w^2 \rangle \tau^2$ at all times. The model is otherwise the same as the solid line. A pure ballistic separation is not realistic, and we show it here just to illustrate whether the Richardson separation phase provides important contribution to the relative velocity. At

$0.5 \lesssim St \lesssim 5$, the dot-dashed line significantly underestimates $\langle w^2 \rangle$, and, from $St \simeq 5$, it becomes close to both the data points and the solid line using a two-phase separation behavior. A possible explanation for this is that, for $0.5 \lesssim St \lesssim 5$, the relative velocity receives a significant contribution from the Richardson phase, even though this phase occurs at times beyond the particle memory timescale, i.e., at $\tau \lesssim -\tau_p$. In that case, accounting for this phase would then be necessary for particles with intermediate St . However, the validity of the above interpretation is subject to future tests. There is the possibility that the discrepancy between the dot-dashed line and the data points is mainly caused by various uncertainties in our model for the trajectory structure tensor, S_{Tij} (see above). It is possible that, with an improved model for S_{Tij} , a pure ballistic separation may give a prediction that better matches the simulation data for St in the range $0.5 \lesssim St \lesssim 5$.

The dashed line is the prediction of the simplified model, eqs. (20) and (25), using a single-exponential Φ_2 . As before, the model with a bi-exponential Φ_2 gives almost the same prediction. The same two-phase separation behavior as in the solid line for the original PP10 model is adopted. For the simplified model, the best-fit value of g is found to be $\simeq 1$, which is close to the g values measured from tracer particles. The simplified model also fits the data better for intermediate St , although the assumption made in the model is physically not better than the original PP10 model. The simplified model may be a preferred choice, as its prediction is easier to compute.

We find that the Stokes number, St_m , at which the rms relative velocity peaks is $\simeq 30$, corresponding to a friction timescale twice larger than T_L . The peak value of the 3D rms relative velocity is $\simeq 6.2u_\eta$, twice smaller than the 3D rms velocity ($\sqrt{3}u'$) of the flow. We give an explanation for the behavior of the peak relative velocity using the qualitative analysis of our model prediction given in §3.2.4. The analysis was based on the primary distance R_p , estimated as $R_p = \langle w^2 \rangle^{1/2} \tau_p$. R_p generally increases with τ_p . Around the peak of the relative velocity, $\tau_p \simeq 30\tau_\eta$ and $\langle w^2 \rangle^{1/2} \simeq 6.2u_\eta$, and thus $R_p \simeq 200\eta$. From eq. (23), the correlation time, $T(\ell)$, at $\ell \simeq 200\eta$ is about $14\tau_\eta$, which is close to T_L . For $St \gtrsim 30$, $T(R_p)$ would be constant and $\simeq T_L$. Consequently, the Φ_2 term in eq. (30) provides a factor of T_L/τ_p for all particles with $St \gtrsim 30$ (see §3.2.4). Using the same analysis as in §3.2.4, one can show that this factor causes the relative speed to decrease with τ_p , even though the structure functions $S_{ll}(R_p)$ and $S_{nn}(R_p)$ are still increasing with R_p for $R_p \simeq 200\eta$ (see Fig. 3). For particles with $St \lesssim 30$, both the structure functions and $T(R_p)$ decrease with decreasing R_p , and thus the relative speed would decrease with decreasing τ_p . Therefore a peak forms at $St_m \simeq 30$. We find that, for particles with $St \simeq 30$, the amplitude of the flow velocity difference at the primary distance ($R_p \simeq 200\eta$) is smaller than $\sqrt{3}u'$, and this is responsible for why the maximum relative velocity is significantly lower than the rms velocity of the flow. The discussion here shows that the relative velocity is the largest for the particles whose primary distance R_p corresponds to the size of turbulent eddies with lifetime $\simeq T_L$. Clearly, the backward particle separation plays an important role in determining the peak Stokes

number, St_m .

We give a brief discussion on the model of Volk et al. (1980) and its later developments and show that it is likely that their prediction does not well match our simulation data. In these models, the predicted relative speed reaches its maximum value when τ_p is equal to a large eddy time, t_L (e.g., Markiewicz, Mizuno & Volk 1991, Cuzzi and Hogan 2003, Ormel & Cuzzi 2007). The definition of t_L in these studies is different from the timescales used in the current work, and it is not clear whether, using parameters appropriate for our simulated flow, the model may correctly produce a peak at $St_m = 30$. One may need to tune the value of t_L in the model such that the peak of the relative speed occurs at the right Stokes number. Another issue is that, in both the original Volk et al. model and its later extensions, the peak relative speed is predicted to be equal or close to the rms velocity of the flow. This means that the model overestimates the relative speed by a factor of 2 around the peak, assuming the peak position, St_m , is correctly produced. A physical problem of the Volk et al. model has been discussed in the Introduction, and the interested reader is referred to PP10 for details. One possibility is that the performance of the Volk et al. (1980) model may improve as the Reynolds number of the flow increases. This will be tested in a future work with higher-resolution simulations.

6.1.1. Dependence on the Particle Distance

Fig. 6 plots the 3D rms relative velocity for particle pairs at different distances, r . The squares, circles and diamonds correspond to $r = 1$, 0.5 and 0.25η , respectively. The relative velocity shows a r -dependence at $St \lesssim 6$, while it is independent of r for $St \gtrsim 6$ particles. In the context of our physical picture, this is because the friction time, τ_p , of $St \gtrsim 6$ particles is long enough that the backward particle separation after a duration of $\simeq \tau_p$ is insensitive to the “initial” value, r . On the other hand, the relative speed of smaller particles relies on the flow velocity difference they saw in the near past, when the particle separation was still dependent on r .

The solid and dotted lines are predictions of the PP10 model with bi-exponential correlation function Φ_2 and the simplified version with single-exponential Φ_2 , respectively. The lines for $r = 1\eta$ have already been shown in Fig. (5), and the Richardson constant, g , was set to 1.6 and 1.0, respectively, in the two models. We find that, at smaller r , the best-fit value of g becomes smaller. For the PP10 model, we adopted $g = 1.3$ and 1.0 for $r = 0.5$ and 0.25η , respectively. The decrease of g with decreasing r is consistent with our result in Appendix A for the pair separation of tracer particles. The backward dispersion of tracer pairs was found to be slower for smaller r . Similarly, the g value used in the simplified model also decreases with decreasing r . In the dashed lines for $r = 1$, 0.5 and 0.25η , the value of g is set to 1, 0.7 and 0.5, respectively.

The relative speed of the smallest particles ($St \simeq 0.1$) in our simulation appears to be larger than the second smallest ones ($St \simeq 0.2$), especially at smaller r . Slight dips are thus seen at $St \simeq 0.2$ (Fig. 6.). This is in contrast to the S-T formula, which predicts the relative speed at a given r is constant at sufficiently small St . These dips are not expected from the physical picture of our

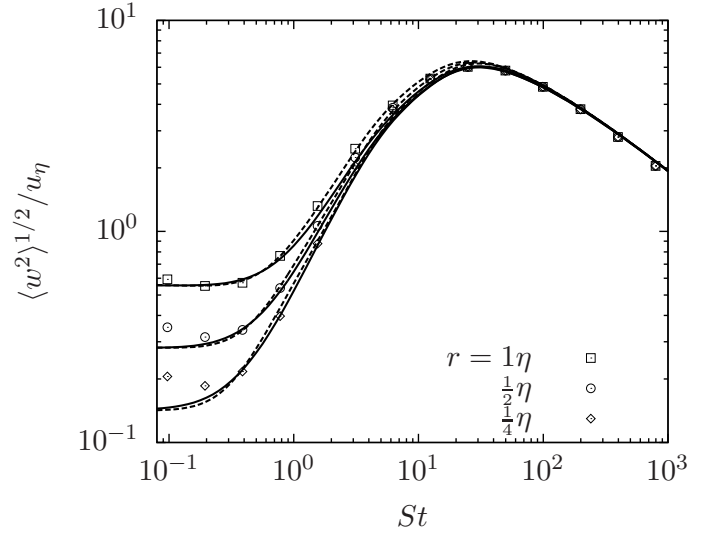


FIG. 6.— The 3D rms relative velocity, $\langle w^2 \rangle^{1/2}$, at $r = 1$ (squares), 0.5 (circles) and 0.25η (diamonds). Solid and dashed lines are predictions of the PP10 model with bi-exponential Φ_2 and the simplified version with single-exponential Φ_2 , respectively. The two-phase separation behavior connecting at $\tau = -\tau_p$ is adopted in both models. In the PP10 model, the Richardson constant g is set to 1.6, 1.3 and 1.0 for solid lines from top to bottom. The corresponding g values used in the simplified model are 1, 0.7 and 0.5, respectively.

model either, and their existence is thus questionable. One possibility is that the rise of the relative speed toward $St \simeq 0.1$ is a numerical artifact. This suspect is based on the consideration that the trajectory integration in our simulation is likely less accurate for smaller particles. The accuracy of the trajectory computation depends on the integration time step relative to the friction timescale, τ_p . The time step is the same for all particles in our simulation, so the accuracy is expected to be lower for smaller particles. Since we are not aware of a convincing physical mechanism that may cause a dip at $St \simeq 0.2$, we tentatively assume the rise of the relative speed at $St \simeq 0.1$ is due to a numerical artifact. This hypothesis will have to be tested with future simulations with a better temporal resolution of the trajectories of small particles.

As mentioned earlier, the 3D rms relative velocity measured in our simulation for small particles at $r = 1\eta$ is consistent with the S-T prediction. The S-T formula also predicts that $\langle w^2 \rangle^{1/2}$ scales linearly with r in the $St \ll 1$ limit. This linear scaling is, however, not confirmed by the data for the smallest particles in the simulation. A rough power fit for the rms relative speed as a function of r gives $\langle w^2 \rangle^{1/2} \propto r^{0.78}$ at $St = 0.1 - 0.2$. This means that, for particles with $St \simeq 0.1 - 0.2$, the S-T formula is already invalid at $r \lesssim 0.5\eta$. At a given St , a critical particle distance is expected, below which the linear scaling does not apply. The physical reason is that, as r decreases, the local flow velocity difference across r becomes smaller, and it is easier for the particle memory of the flow velocity difference in the past to provide a significant contribution, which tends to invalidate the S-T prediction. Equivalently, at a given r , the S-T formula is valid only below a critical St . In Fig. 6, the lines for $r \lesssim 0.5\eta$ show that, as St decreases to $\simeq 0.2$, the relative

speed predicted by our model is not flat yet, suggesting a significant contribution from the particle memory. For $r \lesssim 0.5\eta$, the S-T prediction may be recovered at St much smaller than 0.2, assuming that the rise of the relative speed toward $St \simeq 0.1$ in the data points is indeed a numerical artifact.

Our model does not directly account for the sling effect (Falkovich et al. 2002; Falkovich and Pumir 2007) or the related caustic formation (Wilkinson & Mehlig 2005; Wilkinson et al. 2006; Gustavsson & Mehlig 2011). The effect of slings is usually considered in the context of small particles with $St \lesssim 1$. As mentioned in the Introduction, the effect corresponds to crossing of particle trajectory that occurs at fluid streamlines with high curvature or local flow regions with large velocity gradient. The trajectory crossing contributes to the relative velocity of particles especially at small distances. In our physical picture, the effect of slings or caustics could be viewed as a contribution to the backward particle separation, and, in principle, it may be incorporated in our model by quantifying the frequency and contribution of such events. Based on the model of Wilkinson et al. (2006) and Gustavsson & Mehlig (2011), at a given small St , the effects of caustics would dominate the S-T contribution at a sufficiently small distance, r . Falkovich and Pumir (2007) showed that the sling effect is already significant at $St \simeq 0.2$. In Fig. 6, we see that our model prediction underestimates the relative velocity of $St = 0.2$ particles at $r \lesssim 0.5\eta$. This is a sign of the contribution from slings or caustics. We will discuss the effect of caustics on the particle collision rate in §6.2.

6.1.2. The Radial and Tangential Relative Speeds

In Fig. 7, we show the rms relative speeds in the radial (circles) and tangential (diamonds) directions for particle pairs at $r = 1, 0.5$ and 0.25η . At $St \lesssim 1$, the tangential rms speed, $\langle w_t^2 \rangle^{1/2}$, is slightly larger (by $\simeq 10\%$) than the radial rms, $\langle w_r^2 \rangle^{1/2}$. This difference is significantly smaller than the prediction of the S-T formula, eq. (11), that predicts that in the $St \ll 1$ limit the tangential rms relative speed should be larger than the radial rms by a factor of $\sqrt{2}$. Our data implies that this prediction is not valid at least for particles with $St \gtrsim 0.1$. It remains to be checked whether the factor of $\sqrt{2}$ difference between the radial and tangential rms relative speeds would be recovered at smaller Stokes numbers. At $St \gtrsim 1$, $\langle w_r^2 \rangle^{1/2}$ and $\langle w_t^2 \rangle^{1/2}$ become exactly equal.

The solid lines in Fig. 7 correspond to the prediction of the PP10 model using eq. (27) for the angular average of the trajectory structure tensor, S_{Tij} . The equation assumes that the direction of the particle separation \mathbf{R} at any time is completely random, and predicts that $\langle w_r^2 \rangle = \langle w_t^2 \rangle = \frac{1}{3}\langle w^2 \rangle$ for all particles (§3.2.2). This prediction is in good agreement with our simulation data. The equality of the radial and tangential rms speeds for $St \gtrsim 1$ is expected, because the separation \mathbf{R} of these particles at a friction timescale ago is significantly larger than the initial distance, r , and the direction of \mathbf{R} is expected to be random with respect to \mathbf{r} . On the other hand, the near equality of $\langle w_r^2 \rangle^{1/2}$ and $\langle w_t^2 \rangle^{1/2}$ at $St \sim 0.1 - 0.2$ is somewhat surprising. For $r = 1\eta$, the backward separation of these particles does not con-

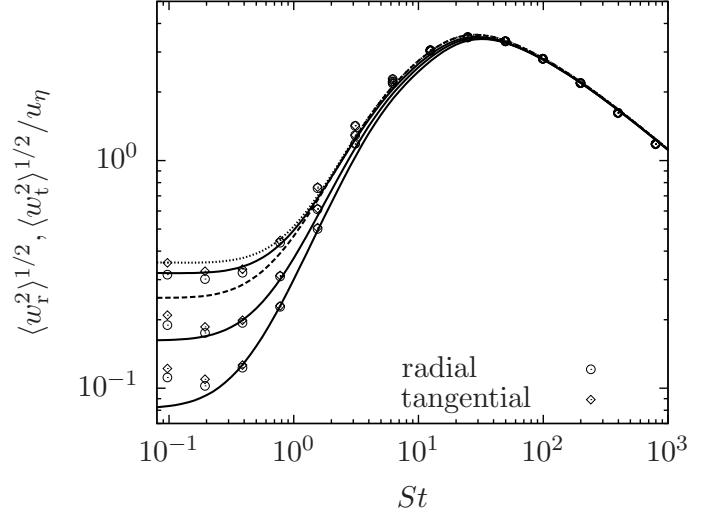


FIG. 7.— The rms relative speeds in the radial ($\langle w_r^2 \rangle^{1/2}$; circles) and tangential ($\langle w_t^2 \rangle^{1/2}$; diamonds) directions. From top to bottom, data points show simulation results for particle pairs at $r = 1, 0.5$, and 0.25η , respectively. Lines are predictions of the PP10 model. The solid lines adopt eq. (27) for the angular average of S_{Tij} , which predicts that $\langle w_r^2 \rangle = \langle w_t^2 \rangle = \frac{1}{3}\langle w^2 \rangle$. The particle separation behavior assumed here is exactly the same as in the solid lines in Fig. 6 for the 3D rms speed. The Richardson constant, g , is set to 1.6, 1.3 and 1.0 for $r = 1, 0.5$, and 0.25η , respectively. The dashed and dotted lines for $r = 1\eta$ are solutions of eq. (31) for the radial and tangential speeds, respectively. The two lines reproduce the Saffman-Turner prediction for $\langle w_r^2 \rangle^{1/2}$ and $\langle w_t^2 \rangle^{1/2}$ at small St .

tribute to make the 3D amplitude, $\langle w^2 \rangle^{1/2}$, of the relative velocity significantly larger than the S-T prediction. This suggests that the near equality of $\langle w_r^2 \rangle^{1/2}$ and $\langle w_t^2 \rangle^{1/2}$ is due to a conversion of the relative velocity from the tangential to the radial direction. The conversion is likely caused by the deviation of the particle trajectories from the fluid elements. Even though the deviation does not give rise to a considerable change for the 3D rms $\langle w^2 \rangle^{1/2}$ at $r = 1\eta$, it could efficiently alter the direction of \mathbf{w} with respect to \mathbf{r} . The trajectory deviation is stochastic, and thus tends to randomize the direction of \mathbf{w} and equalize its radial and tangential components. This reduces the tangential-to-radial ratio below the S-T prediction. The randomization effect is expected to be more efficient in the slings events, where inertial particles are shot out of the streamlines of the flow, and encounter the trajectories of other particles (Falkovich and Pumir 2007). At smaller r , the contribution from the backward separation to the 3D relative speed is larger, and the random direction of the particle separation in the past also tends to equalize the radial and tangential relative speeds.

When computing the solid lines, we used a bi-exponential form for Φ_2 , and the separation behavior adopted here is exactly the same as for the solid lines in Fig. 6 for the 3D rms speed. This means that the solid lines shown here correspond to those in Fig. 6 divided by $\sqrt{3}$. The Richardson constant is set to 1.6, 1.3 and 1.0 in the three lines for $r = 1, 0.5$, and 0.25η , respectively.

The dashed and dotted lines for $r = 1\eta$ are the solutions of eq. (31) for the radial and tangential rms speeds, respectively. Eq. (31) was derived from eq. (26) for

$\langle S_{Tij} \rangle_{\text{ang}}$, which assumes that the direction of the separation change $\Delta \mathbf{R}$ (rather than \mathbf{R} itself) is random. When solving eq. (31), we used the same two-phase separation behavior (with $g = 1.6$) as in the corresponding solid line. At small St , the dashed and solid lines reproduce the S-T prediction that $\langle w_t^2 \rangle = 2\langle w_r^2 \rangle$. The discrepancy between the simulation data and the S-T formula implies that the direction of \mathbf{R} is more random than assumed in eq. (26) for St in the range $0.1 \lesssim St \lesssim 1$.

The dependence of the radial and tangential rms relative speeds on r is similar to that of the 3D rms (see Fig. 6). In an attempt to roughly fit them as power-law functions of r , we find that $\langle w_t^2 \rangle^{1/2}$ and $\langle w_r^2 \rangle^{1/2}$ scale with r as $\propto r^{0.78}$ at $St = 0.1 - 0.2$. Similar to the 3D rms, the slight dips at $St \simeq 0.2$ for both the radial and tangential relative speeds may be due to a numerical artifact.

The simulations of Wang et al. (2000) found that the tangential-to-radial variance ratio, $\langle w_t^2 \rangle / \langle w_r^2 \rangle$, is $\simeq 1.5 - 1.6$ at $St \simeq 0.1 - 0.2$. This is larger than the corresponding value ($1.2 - 1.3$) in our simulation, and closer to the S-T prediction. One possible reason for this difference is that our flow has a much larger Reynolds number. Although Wang et al. (2000) claimed that the ratio is independent of Re_λ based on several simulations with $Re_\lambda \lesssim 75$, it is not clear if this is also true at $Re_\lambda \gg 75$. As speculated above, it is the deviation of the particle trajectories from the flow elements that tends to equalize the radial and tangential relative speeds of small particles. Clearly, the trajectory deviation would be larger in flow regions with larger velocity gradients, where the flow experiences a faster velocity change. The probability of finding large flow velocity gradients and hence large trajectory deviations increases with Re_λ . Therefore, the tangential-to-radial ratio is likely smaller at higher Reynolds numbers. Similarly, the frequency of sling events, which occur in regions with extreme flow velocity gradients, would increase with Re_λ (Falkovich and Pumir 2007), and this also tends to reduce the tangential-to-radial ratio. However, we cannot rule out that the time resolution for the trajectory integration of the smallest particles in our simulation is not sufficient to allow an accurate measurement of $\langle w_t^2 \rangle / \langle w_r^2 \rangle$ at small St .

6.1.3. Approaching and Separating Particle Pairs

So far, our analysis for the particle relative velocity included all particle pairs at given distances. However, not all pairs at a small distance lead to collisions. Particles with a negative radial relative velocity, $w_r < 0$, approach each other and may collide, while particles in pairs with $w_r > 0$ move away from each other. Since the goal of our study is to examine the collision of dust particles, it is appropriate to split the particle pairs at a given distance into two groups: one with $w_r < 0$ and the other with $w_r \geq 0$. We will refer to them as the minus and plus groups, respectively. Although only the first group is relevant for particle collisions, it is theoretically interesting to compare the relative velocity of particle pairs in the two groups.

For the radial component, w_r , of the relative velocity, we denote the variances in the minus and plus groups as $\langle w_r^2 \rangle_-$ and $\langle w_r^2 \rangle_+$, respectively. In terms of the PDF, $P(w_r, St)$, of w_r at a given St , the variances are written as $\langle w_r^2 \rangle_- = \int_{-\infty}^0 w_r^2 P(w_r, St) dw_r / \int_{-\infty}^0 P(w_r, St) dw_r$ and

$\langle w_r^2 \rangle_+ = \int_0^\infty w_r^2 P(w_r, St) dw_r / \int_0^\infty P(w_r, St) dw_r$. We denote the PDFs of the tangential component in the minus and plus groups as conditional PDFs, $P(w_t | w_r < 0, St)$ and $P(w_t | w_r > 0, St)$. The tangential variances in the two groups are then given by $\langle w_t^2 \rangle_\mp = \int_{-\infty}^\infty w_t^2 P(w_t | w_r \leq 0, St) dw_t$. Similarly, for the 3D amplitude, $|\mathbf{w}|$, the minus and plus variances are expressed as $\langle w^2 \rangle_\mp = \int_{-\infty}^\infty w^2 P(|\mathbf{w}| | w_r \leq 0, St) d|\mathbf{w}|$, where $P(|\mathbf{w}| | w_r \leq 0, St)$ are the PDFs of $|\mathbf{w}|$ for approaching and separating pairs. In this subsection, we discuss the rms (or variances) of the particle relative velocity in the two groups, and the PDFs, $P(w_r, St)$, $P(w_t | w_r \leq 0, St)$, and $P(|\mathbf{w}| | w_r \leq 0, St)$, will be studied in §6.3.

The data points in the left panel of Fig. (8) show the radial rms relative speeds of particle pairs at $r = 1\eta$ (squares) and 0.25η (circles). The right panel plots the tangential (squares) and 3D (circles) rms speeds at $r = 1\eta$. In both panels, the filled and open symbols correspond to particle pairs in the minus and plus groups, respectively, and the lines plot the overall rms relative velocities counting all particle pairs at given distances. If the velocity of $St \ll 1$ particles closely follow the flow velocity, we expect that $\langle w_r^2 \rangle_\mp$ are determined by the variances of the longitudinal flow velocity increments, $\langle \Delta u_r^2 \rangle_\mp$, for the negative and positive Δu_r , respectively. The definition of $\langle \Delta u_r^2 \rangle_\mp$ is given in Appendix B, and they correspond to the fluctuation amplitudes in the left and right wings of the PDF of Δu_r . In Appendix B, we find the ratio $\langle \Delta u_r^2 \rangle_- / \langle \Delta u_r^2 \rangle_+$ is 1.47 at the size of the computation cell, suggesting that, in the $St \rightarrow 0$ limit, $\langle w_r^2 \rangle_-^{1/2}$ would be larger than $\langle w_r^2 \rangle_+^{1/2}$ by $\simeq 20\%$. The simulation result is consistent with this expectation. At $St \simeq 0.1$, the ratio of $\langle w_r^2 \rangle_-^{1/2}$ to $\langle w_r^2 \rangle_+^{1/2}$ is $\simeq 25\%$ for both $r = 1$ and 0.25η (see the left panel of Fig. 8). Using a similar analysis to the tangential component gives $\langle w_t^2 \rangle_\mp \simeq \langle \Delta u_t^2 \rangle_\mp$ for $St \ll 1$, where $\langle \Delta u_t^2 \rangle_\mp$ are variances of the transverse flow velocity increment, Δu_t , conditioned on the sign of longitudinal increment Δu_r (see Appendix B). The ratio $\langle w_t^2 \rangle_-^{1/2} / \langle w_t^2 \rangle_+^{1/2}$ is found to be 1.16 at $St = 0.1 - 0.2$, consistent with the ratio of $\langle \Delta u_t^2 \rangle_-$ to $\langle \Delta u_t^2 \rangle_+$ at the cell size (see Appendix B). For the 3D amplitude ($\langle w^2 \rangle_\mp^{1/2}$), the rms ratio between the minus and plus groups is 1.18 at $St \ll 1$.

As St increases, the relative speed for the plus group first decreases slightly and reaches a minimum at $St \simeq 0.4$ in all cases with $r = 1\eta$. This can be explained by considering the effects of the particle memory and the particle separation backward in time. Particle pairs in the plus group with $w_r > 0$ are coming from smaller distances, meaning that the separation of the particles was smaller in the near past. As St increases from 0.1 to 0.4, the contribution from the particle memory of the flow velocity difference becomes relatively more important, and this contribution tends to reduce the relative speed since the particle distance was smaller in the immediate past. However, if we look back further into the past (i.e., at larger $|\tau|$), the two particles may pass each other, and their distance would make a transition from decreasing to increasing as $|\tau|$ keeps increasing. This explains the increase of $\langle w_r^2 \rangle_+$, $\langle w_t^2 \rangle_+$, and $\langle w^2 \rangle_+$ at $St \gtrsim 0.4$. The minimum of $\langle w_r^2 \rangle_+$ for $r = 0.25\eta$ appears at $St = 0.2$

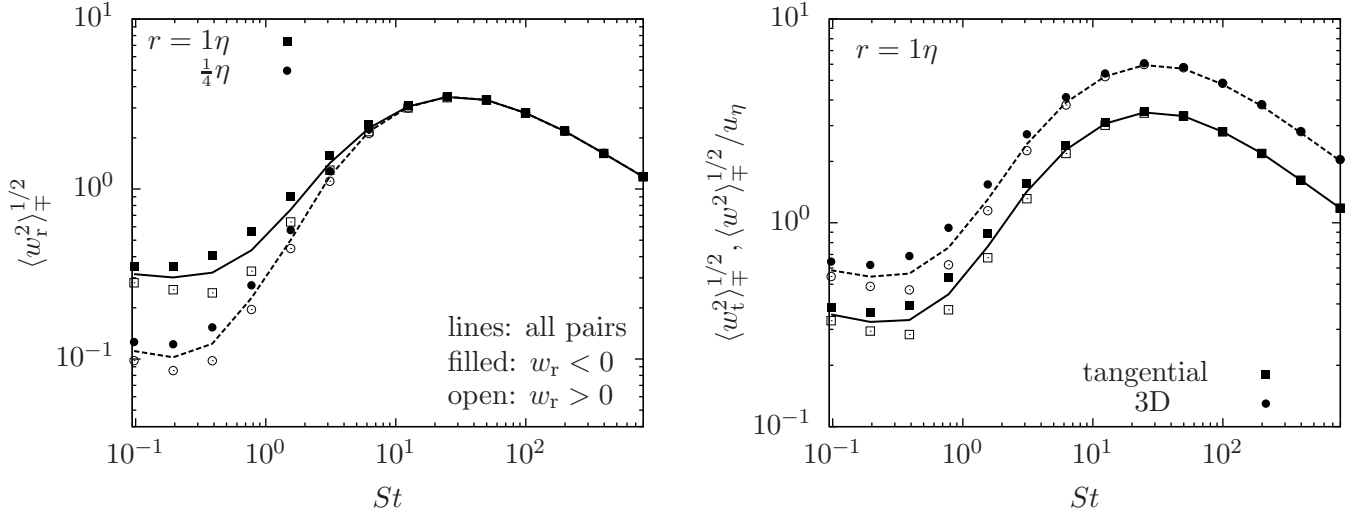


FIG. 8.— The rms relative speeds for particle pairs approaching ($w_r < 0$; filled symbols) or separating ($w_r > 0$; open symbols) from each other. Lines correspond to the overall rms relative speeds counting all particle pairs. Left panel: The radial rms speed $\langle w_r^2 \rangle_{\pm}^{1/2}$ in the minus and plus groups with $r = 1\eta$ (squares) and 0.25η (circles). Right panels: the tangential (squares) and 3D (circles) rms relative speeds for particle pairs at $r = 1\eta$.

instead of $St = 0.4$. This is because, for smaller r , it takes a shorter time for the particle distance in the past to change from decreasing to increasing.

For approaching particles in the minus group, the particle distance would increase monotonically toward the past. Therefore, the relative speed for the minus group is expected to monotonically increase with St for small particles with $\tau_p \lesssim T_L$. This is confirmed by the filled data points in Fig. 8, except the slight dips at $St \simeq 0.2$. These slight dips are not expected, and again may be caused by insufficient numerical accuracy in the trajectory integration for the smallest particles in our simulation (§6.1.1). Fig. 8 shows that approaching particles tend to have a larger relative speed than the separating pairs. The difference between the two groups first increases with St and then starts to decrease at $St \geq 1$. At $St \gtrsim 6.2$, the rms relative speeds in the two groups are close and equal to the overall rms. The reason is that, for these larger particles, the particle separation at a friction timescale ago becomes independent of the “initial” condition at $\tau = 0$.

The rms relative velocity in the minus group is found to be larger than the overall rms for particles $St \lesssim 6$, and an immediate implication is that using the overall rms to calculate the collision energy may lead to an underestimate for these particles. This has not been pointed out by previous studies, which considered the overall rms only. The difference between the 3D rms, $\langle w^2 \rangle_-^{1/2}$, in the minus group and the overall rms $\langle w^2 \rangle^{1/2}$ peaks at $St = 1$, where $\langle w^2 \rangle_-^{1/2}$ is larger by 25%. Therefore, the collision energy may be underestimated by up to 60% if one uses the overall rms relative speed. The prediction of the PP10 model was for the overall rms, and it could be modified to predict the relative velocity specifically for approaching particle pairs. For that purpose, the backward separation behavior of approaching particle pairs must be specified and taken into account. We also find that $\langle w_r^2 \rangle_-^{1/2}$ and $\langle w_t^2 \rangle_-^{1/2}$ almost coincide for all St , meaning each component of the relative velocity

provides equal amount of collision energy. On average, the radial component provides 1/3 collision energy, while the remaining 2/3 is contributed by the two tangential components.

6.2. The Collision Kernel

The prediction of the collision rate is one of the main goals of our study of the particle relative velocity. If the mean number density of inertial particles of a given size is \bar{n}_p , then the collision rate per unit volume between these identical particles is estimated by $\frac{1}{2}\bar{n}_p^2\Gamma$, where Γ is the collisional kernel and the factor 1/2 is used to avoid counting the same pair twice. The collision kernel depends on the particle cross section and the particle relative speed. The collision rate is also affected by the spatial clustering of inertial particles in turbulent flows. Due to their finite inertia, inertial particles do not exactly follow the flow velocity and have been found to exhibit inhomogeneous distribution even in incompressible turbulence. Turbulent clustering of inertial particles has been extensively investigated in the literature (see e.g., Maxey 1987, Sundaram and Collins 1997, Wang et al. 2000, Cuzzi et al. 2001, Hogan & Cuzzi 2001, Balkovsky et al. 2001, Zaichik et al. 2003, Falkovich and Pumir 2004, Cuzzi et al. 2008, Pan et al. 2011). The general physical interpretation for turbulent clustering is that the vortical structures in turbulent flows tend to expel inertial particles. The particles are pushed out of high-vorticity regions by the centrifugal force, leading to the formation of clusters in strain-dominated regions. The degree of turbulent clustering is usually quantified by the so-called radial distribution function (RDF), $g(St, r)$. The RDF is defined such that the number of particles in an infinitesimal volume, dV , located at a distance r from a given particle, is $\bar{n}_p g(St, r) dV$. The RDF is essentially the enhancement factor for the probability of finding a neighboring particle. The contribution of turbulent clustering to the collision kernel (or the collision rate) for identical particles is a factor of $g(St, d_p)$ at a distance of

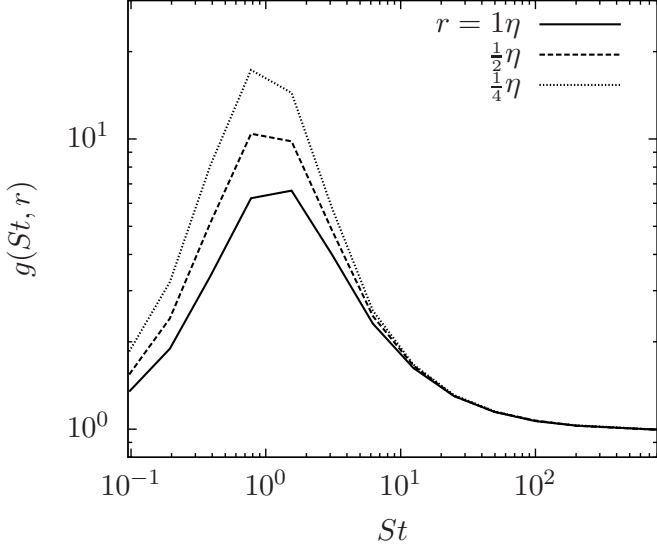


FIG. 9.— The radial distribution function, $g(St, r)$, as a function of the Stokes number at $r = 1$ (solid), 0.5 (dashed) and 0.25η (dotted).

the particle diameter, d_p .

Fig. 9 plots the RDF as a function of St at three distances, $r = 1, 0.5$ and 0.25η . Consistent with previous studies, the RDF is largest for $St \simeq 1$ particles, whose friction timescale couples with the smallest scale of the turbulent flow. For particle distance, r , in the dissipation range, the RDF increases toward smaller r as a power-law, i.e., $g(St, r) \propto r^{-\mu}$. The scaling exponent μ peaks at $St \simeq 1$, and approaches zero in the limits $St \ll 1$ and $St \gg 1$. We measured μ using the values of r shown in Fig. 9, and found that $\mu = 0.73$ for $St = 0.78$, which is consistent with the result of Pan et al. (2011). The interested reader is referred to Pan et al. (2011) for the scaling exponent, μ , as a function of St . Existing coagulation models for the growth of dust particles in protoplanetary disks usually ignore the effect of turbulent clustering. This would underestimate the collision rate, especially for dust particles with $St \simeq 1$. At $r = 0.25\eta$, the RDF is already $\simeq 20$ for $St \simeq 1$. The size, a_p , of dust particles is typically much smaller than the Kolmogorov length scale, η (~ 1 km), of the protoplanetary turbulence. Due to the large separation between η and a_p and the power-law increase of the RDF toward small r , the effect of turbulent clustering would provide a significant contribution to the collision rate. Before discussing the clustering effect in more details, we will first consider the formulation of the collision kernel and the contribution from turbulence-induced collision speed.

Saffman and Turner (1956) presented two formulations for the collision kernel. The formulations were based on spherical and cylindrical geometries, respectively, and were thus named as the spherical and cylindrical formulations by Wang et al. (1998). In the spherical formulation, the collision kernel is written as $\Gamma^{\text{sph}} = 4\pi d_p^2 g(St, d_p) F_r^-$. Here F_r^- represents the radial inward flux from a distance of d_p to a given particle. In terms of the PDF, $P(w_r, St)$, of the radial relative speed, the inward flux is given by $F_r^- = -\int_{-\infty}^0 w_r P(w_r, St) dw_r$. In statisti-

cally isotropic turbulence, as is the case for our simulated flow, the particle statistics is expected to become isotropic when the dynamics is fully relaxed. In that case, the inward flux, F_r^- , is equal to the outward flux $F_r^+ (\equiv \int_0^{\infty} w_r P(w_r, St) dw_r)$, which is confirmed by our simulation data. This is because the average radial velocity $\langle w_r \rangle = 0$ from isotropy and $\langle w_r \rangle = F_r^+ - F_r^-$ by definition. We thus have $F_r^+ = F_r^- = \frac{1}{2} \langle |w_r| \rangle$ where $\langle |w_r| \rangle$ is the ensemble average of the absolute value of the radial relative velocity. The collision kernel can then written as $\Gamma^{\text{sph}} = 2\pi d_p^2 g \langle |w_r| \rangle$.

In the left panel of Fig. (10), we plot the simulation result for $\langle |w_r| \rangle$ at three particle distances $r = 1, 0.5$, and 0.25η . For comparison, we also show the data (circles) for the rms of the radial relative speed at $r = 1\eta$. Qualitatively, $\langle |w_r| \rangle$ as a function of St and r is similar to the rms. It is smaller than the rms, as it corresponds to the 1st-order moment of the PDF, $P(w_r, St)$, of w_r . Most theoretical models, including our own, for the particle relative velocity are based on the computation of the variance (e.g., $\langle w_r^2 \rangle$) of the relative speed, and cannot be directly applied to predict $\langle |w_r| \rangle$. The conversion between $\langle w_r^2 \rangle$ and $\langle |w_r| \rangle$ relies on the PDF of w_r , which is difficult to predict. We thus did not attempt to fit $\langle |w_r| \rangle$ with a model prediction. The simulation result for the PDF, $P(w_r, St)$, as a function of St will be discussed in §6.3.

Similar to the S-T formula (eq. 11) for the variances of the relative velocity, we would predict that $\langle |w_r| \rangle = \langle |\Delta u_r| \rangle$ in the limit $St \ll 1$, where $\langle |\Delta u_r| \rangle$ is the absolute average of the longitudinal flow velocity increment. At $\ell \lesssim \eta$, $\langle |\Delta u_r| \rangle$ is expected to scale linearly with ℓ . We find that, for small particles with $St \lesssim 0.4$, $\langle |w_r| \rangle$ at $r = 1\eta$ is consistent with $\langle |\Delta u_r| \rangle$ at $\ell = 1\eta$, which is $\simeq 0.19u_\eta$ in the simulated flow. At smaller r , $\langle |w_r| \rangle$ is found to scale with r as $\propto r^{0.9}$, which is slightly shallower than the linear scaling. This is likely caused by the contribution from the effect of slings or caustics at small r . The scaling is steeper than $r^{0.78}$ for the radial rms velocity (see §6.1.2), suggesting that $\langle |w_r| \rangle$ reflects the flow velocity scaling better. The behavior of $\langle |\Delta u_r| \rangle$ at small St also appears to be more regular than that of $\langle w_r^2 \rangle^{1/2}$. For all three values of r , the $\langle |w_r| \rangle$ curves become flat at $St \lesssim 0.4$, as expected from the prediction $\langle |w_r| \rangle = \langle |\Delta u_r| \rangle$. The likely reason is that $\langle |w_r| \rangle$ represents statistics at a lower order than the rms, and is thus less affected by the rare and extreme sling events, or by the numerical uncertainty in the particle trajectory computation.

The inset of the left panel shows the ratio of the absolute average to the rms. The ratio depends on the shape of the PDF of w_r , and particularly on the central part of the PDF because both $\langle |w_r| \rangle$ and the rms are lower-order moments. As a reference, if the PDF $P(w_r, St)$ is Gaussian, we have $\langle |w_r| \rangle / \langle w_r^2 \rangle^{1/2} = (2/\pi)^{1/2} = 0.80$, and for an exponential PDF it is equal to $1/\sqrt{2}$. The central part of an exponential PDF is sharper than the Gaussian case. Generally, the ratio decreases as the PDF becomes fatter. As seen in the inset, the ratio changes with both St and r . For $r = 1\eta$, the ratio is $\simeq 0.68$ at $St \simeq 0.1-0.2$. With increasing St , it decreases and reaches a minimum of 0.45 at $St \simeq 1$, indicating a highly non-Gaussian PDF.

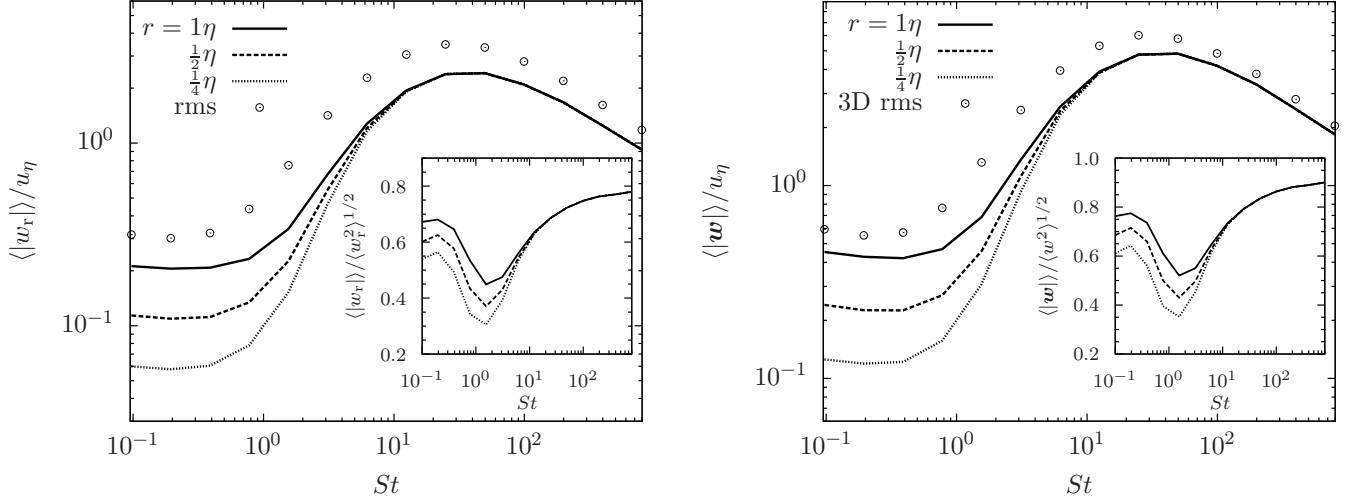


FIG. 10.— Left panel: The average of the absolute value of the radial relative speed, $\langle |w_r| \rangle$, as a function of the Stokes number. Solid, dashed and dotted lines correspond to the particle distance $r = 1, 0.5$ and 0.25η , respectively. For comparison, the circles show the rms, $\langle w_r^2 \rangle^{1/2}$, of the radial relative speed at $r = 1\eta$. The inset plots the ratio, $\langle |w_r| \rangle / \langle w_r^2 \rangle^{1/2}$, at $r = 1$ (solid), 0.5 (dashed) and 0.25η (dotted). Right panel: same as the left panel, but for the 3D amplitude, $\langle |w| \rangle$, and the 3D rms, $\langle w^2 \rangle^{1/2}$, of the relative velocity.

As will be shown in §6.3, as St increases to $\simeq 1$, the fatness of the PDF $P(w_r, St)$ increases: its central part becomes sharper while the tails get broader. As St further increases above 1, the trend for the fatness of the PDF shape is reversed, and the ratio $\langle |w_r| \rangle / \langle w_r^2 \rangle^{1/2}$ increases. At $St \simeq 800$, it reaches 0.78, close to the expected value for a Gaussian PDF. The ratio also decreases with decreasing r for $St \lesssim 6$. This is due to the sharpening of the central part of the PDF with decreasing r (see §6.3.3). At larger St , the PDF shape and hence the ratio $\langle |w_r| \rangle / \langle w_r^2 \rangle^{1/2}$ are independent of r (§6.3.3).

We next discuss the cylindrical formulation, in which the collision kernel is written as $\Gamma^{\text{cyl}} = \pi d_p^2 g \langle |w| \rangle$, with $\langle |w| \rangle$ being the average of the 3D amplitude of the relative velocity. This formula assumes that all particles inside a cylinder of length $\langle |w| \rangle dt$ located at a distance d_p from a given particle will collide with the particle in a time interval dt . Our simulation result for $\langle |w| \rangle$ is shown in the right panel of Fig. (10), which is very similar to the left panel for $\langle |w_r| \rangle$. At small $St \lesssim 0.4$, we find $\langle |w| \rangle$ also scales as $r^{0.9}$ with r . The ratio of $\langle |w| \rangle$ to the rms, $\langle w^2 \rangle^{1/2}$, also shows a dip at $St \simeq 1$ and approaches 0.9 at the largest St . Similarly, this can be understood from the PDF of $|w|$ as a function of St (see §6.3). The value of 0.9 is expected from a 3D Gaussian distribution.

In Fig. 11, we plot the products of the RDF and the absolute average of the relative velocity, $2g(St, r) \langle |w_r| \rangle / u_\eta$ (solid lines) and $g(St, r) \langle |w| \rangle / u_\eta$ (dashed lines), for the spherical and cylindrical formulations of the collision kernel, respectively. The two products correspond to Γ^{sph} and Γ^{cyl} measured at a distance of r and normalized to $\pi d_p^2 u_\eta$. We refer to the products as the normalized kernel or the collision kernel per unit cross section. The lines from bottom to top are measured at $r = 0.25, 0.5$ and 1η , respectively. At each r , the solid and dashed lines almost coincide, meaning that Γ^{sph} and Γ^{cyl} are nearly equal at all St and r . This suggests that $\langle |w_r| \rangle \simeq 0.5 \langle |w| \rangle$ since $\Gamma^{\text{sph}} / \Gamma^{\text{cyl}} = 2 \langle |w_r| \rangle / \langle |w| \rangle$. The two collision kernels have a noticeable difference only at $St = 0.1 - 0.2$, where Γ^{sph}

is smaller than Γ^{cyl} by $\lesssim 5\%$. This is consistent with the result of Wang et al. (2000), who found that the predictions of the two formulations are equal except a difference of $\lesssim 25\%$ in the limit $St \rightarrow 0$. Wang et al. (2000) also showed that the spherical formulation provides an almost exact description for the particle collision rate. The near equality of Γ^{sph} and Γ^{cyl} at all St and r suggests that one can apply either formulation to evaluate the collision rate.

Fig. 11 shows that $2g(St, r) \langle |w_r| \rangle$ and $g(St, r) \langle |w| \rangle$ are independent of r for $St \geq 1$. From Figs. 9 and 10, we see that, with decreasing r , the RDF, $g(St, r)$, increases, while the absolute average of the relative velocity decreases. Interestingly, for $St \geq 1$, the increase of $g(St, r)$ almost exactly compensates the decrease of $\langle |w_r| \rangle$ (or $\langle |w| \rangle$). For example, at $St = 1.55$, we have $g(St, r) \propto r^{-0.55}$, while both $\langle |w_r| \rangle$ and $\langle |w| \rangle$ scale with r as $r^{0.57}$. As a result, their products are independent of r . According to the model of Wilkinson et al. (2006) and Gustavsson & Mehlig (2011), the effect of caustics provides a scale-independent contribution to the normalized collision kernel. At a given St , the caustic contribution would become dominant at sufficiently small r . The r -independence of the normalized kernel for $St \geq 1$ particles in our simulation suggests that the effect of caustics for these particles is already dominant at $r \lesssim \eta$. This independence also implies that, for $St \geq 1$, one can safely apply our result for $2g(St, r) \langle |w_r| \rangle$ (or $g(St, r) \langle |w| \rangle$) at $r \sim \eta$ to estimate the collision kernel at the particle diameter, d_p , even though, in the case of dust grains in protoplanetary disks, d_p is smaller than η by orders of magnitude.

We find that the collision kernel per unit cross section is almost constant for St between 1 and the peak Stokes number, $St_m \simeq 30$. This is because of the opposite trends of the RDF and the relative velocity with St in this range. The products $2g(St, r) \langle |w_r| \rangle$ and $g(St, r) \langle |w| \rangle$ increase only by 50% as St goes from 1 to 30. The kernel starts to decrease at $St \simeq 30$, and finally scales with St as $St^{-1/2}$ in the large particle limit with $\tau_p \gg T_L$. Interestingly,

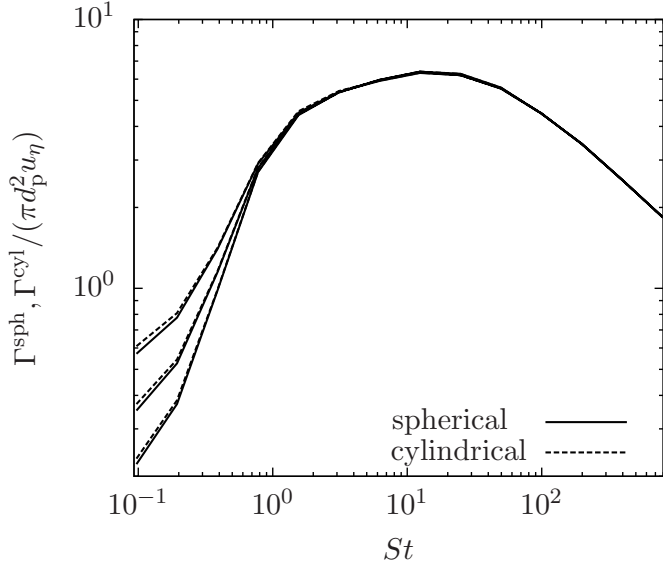


FIG. 11.— The collision kernels normalized to $\pi d_p^2 u_\eta$. The solid lines plot $2g(St, r)\langle|w_r|\rangle/u_\eta$ for the spherical formulation, and the dashed lines show $g(St, r)\langle|\mathbf{w}|\rangle/u_\eta$ for the cylindrical formulation. The lines from bottom to top correspond to normalized kernels measured at $r = 0.25, 0.5$ and 1η , respectively.

in the small particle limit the normalized kernels experience a shape rise as St increase from 0.1 to 1 (see, e.g., Sundaram & Collins 1997), suggesting that the collision frequency greatly accelerates once the particle size grows past $St \sim 0.2$. For $r \gtrsim 0.25\eta$, the rise is mainly contributed by the fast increase of the RDF toward $St \simeq 1$. Based on the model of Wilkinson et al. (2006), the abrupt rise of the normalized kernel corresponds to the rapid formation of caustics, and it was claimed that the effect of caustic formation may be modeled as an activation process. If we fit the normalized kernel by $\exp(-A/St)$ (Wilkinson et al. 2006, Falkovich & Pumir 2007), the activation value, A , is found to be around 0.8.

We give a simple physical explanation for why the sling effect or the caustic formation causes the rapid rise of the normalized kernel at $St \simeq 1$. The sling events occur at places where the flow velocity gradient is larger than τ_p^{-1} (Falkovich et al. 2002). At these locations, the flow velocity changes at a timescale faster than the response of the particle. For small particles with $\tau_p \ll \tau_\eta$, the probability of the sling events corresponds to the high tails of the probability distribution of the flow velocity gradient. With increasing τ_p , the probability becomes larger as it samples toward the inner parts of the flow gradient PDF. Because the rms flow gradient is on the order of τ_η^{-1} , the probability experiences a fast increase as τ_p^{-1} approaches τ_η^{-1} , leading to a sharp rise in the sling frequency and hence in the collision rate at $St \simeq 1$.

At $St \leq 0.8$, the increase of the RDF toward small r is slower than the decrease of the relative speed. Consequently, the normalized kernel decreases with decreasing r , as seen in Fig. 11. This r -dependence needs to be considered when evaluating the collision kernel at $d_p \ll \eta$ for $St \leq 0.8$ particles. A simple approach is to measure the scaling exponent of the normalized kernel with r and then extrapolate the kernel to d_p . For example, the normalized kernel scales with r roughly as $r^{0.68}$ at

$St = 0.1$. However, the validity of this method would finally break down as r keeps decreasing. At smaller r , the contribution of caustics becomes more important. The theoretical result of Gustavsson & Mehlig et al. (2011) indicates that, at a given St , there exists a critical particle distance, r_c , below which the effect of caustics dominates. Since the caustic contribution is r -independent, the normalized kernel would become constant at $r < r_c$. The critical distance r_c is generally a function of St . Our simulation result for the normalized kernel suggests that $r_c \gtrsim 1\eta$ for $St \geq 0.8$ particles (see above), and $r_c \lesssim 0.25\eta$ for $St < 0.8$. If the dependence of r_c on St and the scaling behavior of the normalized kernel above r_c were determined, one could estimate the collision kernel of $St \leq 0.8$ particles for any value of d_p . However, a numerical study to investigate r_c and the caustic contribution as a function of St , for $St \leq 0.8$ particles, is computationally challenging, as it requires a huge number of particles to measure statistics of the RDF and the relative speed at $r \ll \eta$. A possible compromise would be to simulate the turbulent flow at lower resolution in order to allow the computation of a much larger number of particles. We defer such a study to a future work.

In existing coagulation models of dust particle growth in protoplanetary disks, the collision kernel is typically set to $\Gamma^{\text{coa}} = \pi d_p^2 \langle w^2 \rangle^{1/2}$ (e.g., Dullemond and Dominik 2005), which is of the cylindrical type, but different from Γ^{cyl} defined above. It ignores the effect of turbulent clustering and uses the 3D rms instead of the average 3D amplitude, $\langle|\mathbf{w}|\rangle$, of the relative velocity. Clearly, Γ^{cyl} is larger than Γ^{coa} by a factor of $g(St, r_p)\langle|\mathbf{w}|\rangle/\langle w^2 \rangle^{1/2}$. As seen in Figs. 9 and 10, $g(St, r_p)$ is larger than 1, while the second factor $\langle w^2 \rangle^{1/2}/\langle|\mathbf{w}|\rangle$ is smaller than 1. From our simulation data, we find that $g(St, r_p)\langle|\mathbf{w}|\rangle/\langle w^2 \rangle^{1/2}$ is close to unity for $St \gtrsim 6$ or $St \lesssim 0.2$, and the difference between Γ^{coa} and Γ^{cyl} in this St range is within 50%. The agreement of Γ^{coa} and Γ^{cyl} at $St \ll 1$ is simply a coincidence, where $g(St, r_p)$ happens to compensate the ratio $\langle|\mathbf{w}|\rangle/\langle w^2 \rangle^{1/2}$. On the other hand, for St between 0.2 and 6, Γ^{cyl} is significantly larger than Γ^{coa} due to the large values of $g(St, r_p)$. The difference is largest at $St \simeq 1$. For example, at $St = 0.78$, Γ^{coa} is smaller than Γ^{cyl} by a factor of 3.8 and 6.9 for $r = 1\eta$ and 0.25η , respectively. The difference would be even larger as r further decreases. We thus conclude that the collision kernel commonly used in dust coagulation models applies only for $St \gtrsim 6$ or in the limit $St \rightarrow 0$, and it significantly underestimates the collision rate at $St \simeq 1$.

Besides the imprecise formulation of the collision kernel, coagulation models for dust particles in protoplanetary disks also adopt estimates of the rms collision velocity induced by turbulence that are inaccurate, especially for particles with $St \lesssim 6$. The range $St \lesssim 6$ may include all particle sizes up to chondrules for typical disk parameters at a radius of 1 AU. The commonly-adopted rms collision velocities are based on the model of Volk et al. (1980) (or its later developments, e.g., Ormel and Cuzzi 2007). There are two main problems in using these models to estimate the collision rate. First, as mentioned earlier, the Volk et al. model overestimates the peak relative speed at St_m (§6.1), which would result in overestimating the collision rate by a factor of two or so for inertial-range

particles and/or large particles with $St > St_m$. Second, the model of Volk et al. does not reflect the dependence of the relative speed on the particle distance, r , because it does not keep track of the particle separation (PP10). Therefore, the model does not account for the S-T regime and may be viewed as corresponding to $r \rightarrow 0$. The predicted relative speed by Volk et al.'s model sharply drops to zero at $St = 1$, suggesting the collision kernel is exactly zero at $St \leq 1$. This is clearly not the case from the simulation result. The relative velocity does have a dependence on r for $St \lesssim 6$, which, together with the r -dependence of the RDF, is crucial for determining the collisional kernel for $St \lesssim 6$ particles. The cancellation of the two dependences gives a finite collision kernel around $St \simeq 1$. These features cannot be captured by the Volk et al. model, which is thus likely inapplicable to the estimate of the collision rate for $St \lesssim 6$ particles.

6.3. The PDF of the Particle Relative Velocity

In this section, we explore the probability distribution of the relative velocity of nearby inertial particles. An accurate estimate of the PDF of the particle relative velocity is important for modeling the growth and evolution of dust particles in protoplanetary disks. As mentioned in the Introduction, the outcome of particle collisions depends on the collision velocity, and due to the random nature of the turbulent-induced relative velocity, collisions of particles with exactly the same properties may have different outcomes, and thus using a single value, e.g., the rms, for the collision speed of particles of a given size is insufficient. The probability distribution of the collision velocity is needed to calculate the fractions of collisions resulting in sticking, bouncing or fragmentation.

The physical picture of PP10 shows that the relative velocity of inertial particles depends on the flow velocity difference the particle pair saw within a memory timescale or so. This suggests that the statistics of the velocity difference in the carrier flow is crucial for the understanding of the relative velocity PDF of inertial particles. Therefore, we analyzed the PDFs, $P_u(\Delta u_r, \ell)$ and $P_u(\Delta u_t, \ell)$, of the longitudinal and transverse velocity increments, Δu_r and Δu_t , as functions of the length scale, ℓ , in our simulated flow. The results are discussed in details in Appendix B. The flow velocity PDFs are used in the physical explanation for the PDF of the particle relative velocity as a function of particle inertia in §6.3.2.

6.3.1. The PDFs of the radial and tangential components

In Fig. 12, we show the PDFs, $P(w_r, St)$, of the radial component of the relative velocity as a function of the Stokes number. All the PDFs are measured from particle pairs at a distance of 1η . The relative speed is normalized to the Kolmogorov velocity, u_η , and each PDF is normalized to its value at the central peak. In the left panel, the thin dashed line corresponds to tracer particles ($St = 0$). The shape of this line is found to be identical to the PDF, $P_u(\Delta u_r, \ell)$, of the longitudinal flow velocity increment, Δu_r , at the computational cell size ($\ell = 1.7\eta$; see the top line in the left panel of Fig. 18 in Appendix B). This is expected as the tracer particles exactly follow the flow velocity, and $P_u(\Delta u_r, \ell)$ is independent of ℓ in the dissipation range. The solid

color lines of increasing width show the PDFs of particles with increasing St . This corresponds to the increase of the rms relative speed with St for $St \lesssim 24.9$ (see Figs. 7 and 8). For $St \leq 1.55$, the PDF of w_r has a negative skewness, which is inherited from the flow velocity PDF $P_u(\Delta u_r, \ell)$. The PDF becomes symmetric at $St \gtrsim 3.21$. It is interesting to note that, as St increases, the tails of the PDFs become broader, while the innermost part remains unaffected and equal to the PDF of the tracer particles. As to be shown in §6.3.2, the amplification of the PDF tails for small particles correspond to the effect of slings. Due to the tail amplification, the overall PDF shape becomes fatter as St increases to $\simeq 1.55$.¹⁰ With increasing St , the amplification effect proceeds towards the inner parts of the PDF, leading to a sharp cusp-like shape at the center, especially for $St \gtrsim 3.11$. For particles with $St \gtrsim 3.11$, we see that the slope of the outer parts of the PDF tends to steepen when extending to higher tails, i.e., the PDF shape becomes thinner at larger values of w_r . This thinning trend toward the high tails causes a decrease in the overall fatness of the PDF for St above 3.11.

In the right panel, the PDF becomes narrower as the Stokes number increases above 49.7, corresponding to the decrease of the rms velocity with St in the large particle limit (Figs. 7 and 8). The friction timescale of these particles is larger than the correlation timescale (T_L) of the flow velocity at the largest scales, meaning that the memory time of the flow velocity is shorter than the memory of the particles. This induces a factor of T_L/τ_p in the variance of the relative velocity (§3.2.4), causing a decrease of the PDF width at large St . The dotted line in the right panel is the Gaussian fit to the PDF of the largest particles ($St = 795$) in our simulation. The friction timescale of these particles is 54 times larger than T_L , suggesting that the assumption of a Gaussian relative velocity PDF applies only in the extreme limit $\tau_p \gg T_L$.

Fig. 13 shows the PDF, $P(w_t|w_r < 0, \tau_p)$, of a tangential component of the relative velocity conditioned on $w_r < 0$. The measurement of $P(w_t|w_r < 0, \tau_p)$ only counts particle pairs approaching each other. The figure is plot in the same way as Fig. 12 for the radial component. Again, the thin dashed line in the left panel is for tracer particles ($St = 0$). It corresponds to the PDF of the transverse difference, Δu_t , of the flow velocity conditioned on $\Delta u_r < 0$. Our data confirms that the shape of $P(w_t|w_r < 0, 0)$ for tracer particles at $r = 1\eta$ is close to the dashed line in the right panel of Fig. 18 for $P_u(\Delta u_t|\Delta u_r < 0, \ell)$ at $\ell = 1.7\eta$ (Appendix B). The qualitative behavior of $P(w_t|w_r < 0, St)$ as a functions of St is similar to that of $P(w_r, St)$.

For $St = 0.19$ particles, the tails of the radial PDF are significantly amplified with respect to tracers (Fig. 12), while the conditional PDF of the tangential component almost coincides with the tracer PDF (Fig. 13). From the physical picture for the PDF behavior given in §6.3.2, the effects of the particle memory and the backward separation tend to amplify the PDF tails of $St = 0.19$ particles. However, for the tangential PDF, this amplification effect

¹¹ For definiteness, throughout the paper we use “fat” or “thin” to describe the shape of the PDF. The fatness can be quantified, e.g., by kurtosis. On the other hand, the extension or width of the PDF, corresponding to the rms, is described as “broad” or “narrow”.

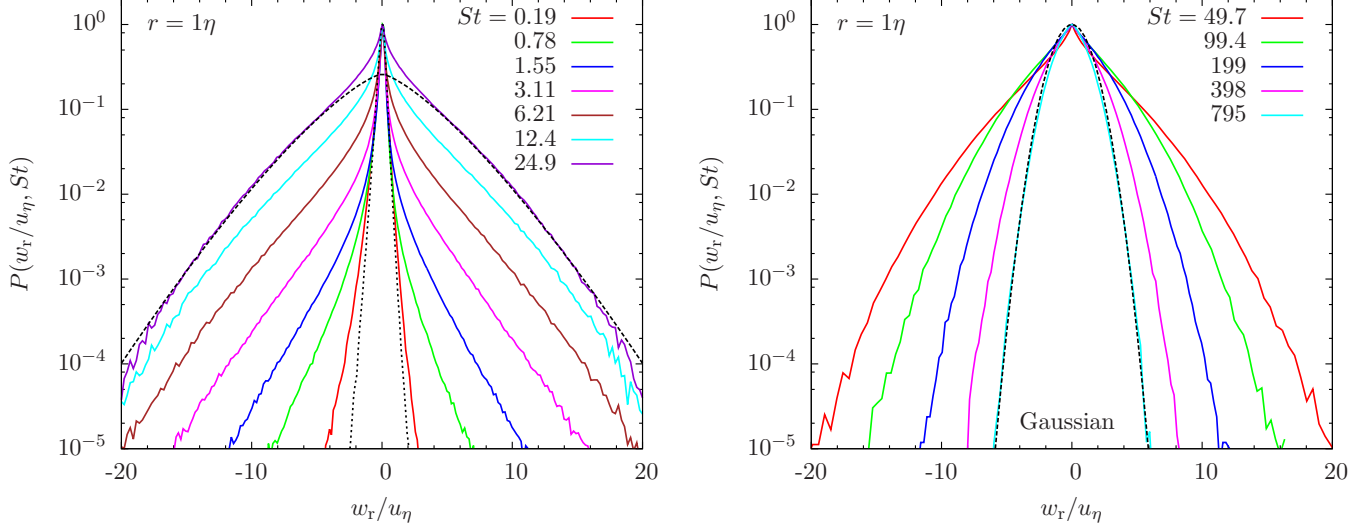


FIG. 12.— The PDF of the radial component (w_r) of the relative velocity at $r = 1\eta$ as a function of the Stokes number. The relative speed is normalized by the Kolmogorov velocity, u_η , and each PDF is normalized to its peak value at $w_r = 0$. The left panel shows the PDFs for particles with $St \leq 24.9$, while the right panel shows results for larger particles with $St \geq 49.7$. The dotted line in the left panel is the PDF of the radial relative speed of tracer particles (i.e., $St = 0$). The dashed line in this panel is the stretched exponential function with $\alpha = 4/3$, which provides a good fit for the PDF tails of $St = 24.9$ particles. In the right panel, the dashed line corresponds to the Gaussian fit to the largest particles in our simulation.

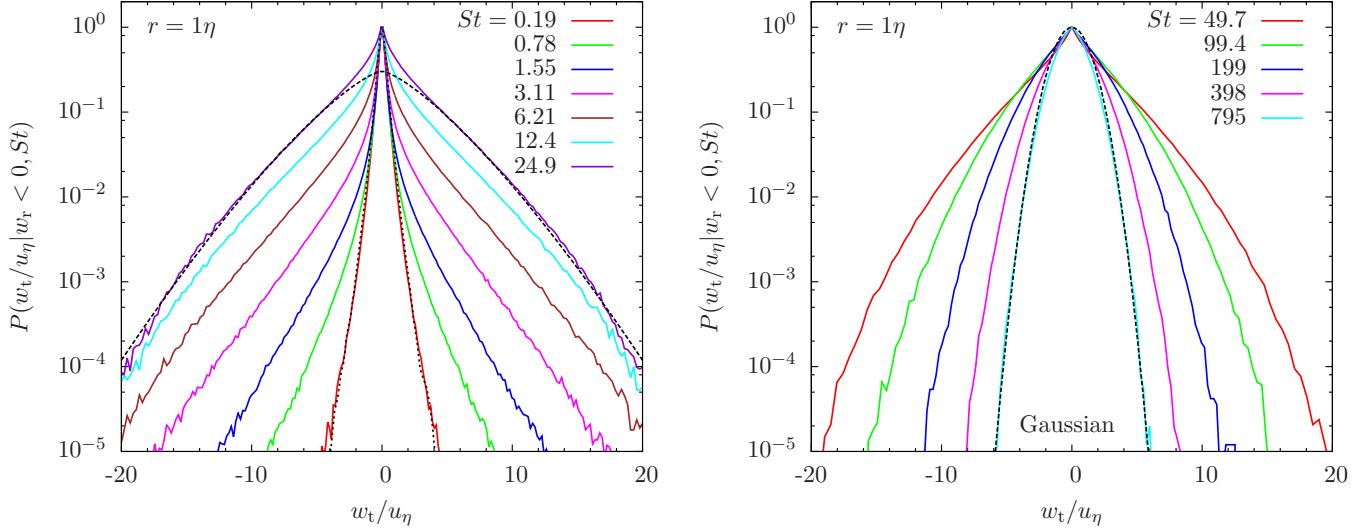


FIG. 13.— The PDFs of the tangential component, w_t , of the relative velocity conditioned on $w_r < 0$. The PDFs are measured from particle pairs approaching each other. The normalization of the PDFs is the same as in Fig. 12. The left and right panels show results for particles with $St \leq 24.9$ and $St \geq 49.7$, respectively. The dotted line in the left panel is the PDF of the tangential relative velocity of tracer particles ($St = 0$) conditioned on $w_r < 0$. The dashed line in this panel is the stretched exponential function with $\alpha = 4/3$. The dashed line in the right panel corresponds to the Gaussian fit for $St = 795$ particles.

is counteracted by the conversion of the relative velocity from the tangential direction to the radial direction, which reduces the PDF width of the tangential component. As discussed in §6.1.2, the conversion is caused by the deviation of inertial particle trajectories from flow elements and the particle memory of the flow velocity in the past, which randomize the direction of the relative velocity relative to the particle separation, \mathbf{r} . The conversion is expected to be especially efficient at the PDF tails, corresponding to the sling events. It appears that the two opposite effects cancel out for the tangential PDF of $St \simeq 0.19$ particles, as it almost coincides with the dotted line for tracers. On the other hand, both effects

broaden the PDF of the radial component, leading to significantly amplified tails with respect to tracers.

Unlike $P(w_r, St)$, which has a negative skewness for $St \leq 1.55$ particles, $P(w_t | w_r < 0, St)$ is symmetric at all St . As mentioned earlier, the symmetry of the PDF in a tangential direction is expected from the statistical isotropy. We find that the left wing of the radial PDF $P(w_r, St)$ almost coincides with that of $P(w_t | w_r < 0, St)$ at all St . This is apparently due to the randomization of the relative velocity direction discussed above. On the other hand, the right wing of $P(w_r, St)$ is narrower than that of $P(w_t | w_r < 0, St)$ until it becomes symmetric at $St \gtrsim 3.11$. For particle collisions, we are mainly inter-

ested in the PDFs for approaching pairs, i.e., the left wing of $P(w_r, St)$ and the entire PDF, $P(w_t|w_r < 0, St)$.

We give a more quantitative description for the shape of $P(w_t|w_r < 0, St)$. The description also applies to the left wing of $P(w_r, St)$, as it coincides with the left wing of $P(w_t|w_r < 0, St)$. We first quantify the fatness of the tangential PDF by computing the kurtosis, defined as $\langle w_t^4 \rangle_- / \langle w_t^2 \rangle_-^2$, for $P(w_t|w_r < 0, \tau_p)$. At $r = 1\eta$, the kurtosis for $St = 0.1$ and 0.19 particles is $\simeq 11$, which is already much larger than 3 for a Gaussian PDF. With increasing St , the kurtosis first increases due to the tail amplification. It reaches a maximum value of 36 at $St = 0.78$, indicating extremely high non-Gaussianity. The kurtosis decreases slightly to 32 at $St = 1.55$, and then drops rapidly and approaches $\simeq 3$ at the largest $St (= 795)$ in our simulation. This decrease corresponds to the thinning trend of the high PDF tails for these large particles. We also measured the kurtosis for the PDFs at smaller r , and found that it increases with decreasing r for $St \lesssim 6.2$. The PDFs are fatter at smaller r because the effect of the tail amplification on the PDF shape is relatively stronger (see discussions in §6.3.3). Also for a smaller r , the maximum kurtosis occurs at smaller St .

Following Sundaram & Collions (1997) and Wang et al. (2000), we attempted to fit $P(w_t|w_r < 0, \tau_p)$ with stretched exponential distributions. The generic stretched exponential function is defined as,

$$P_{se}(x) = \frac{\alpha}{2\beta\Gamma(1/\alpha)} \exp \left[- \left(\frac{|x|}{\beta} \right)^\alpha \right], \quad (34)$$

where Γ is the Gamma function. The variance of P_{se} is given by $\beta^2\Gamma(3/\alpha)/\Gamma(1/\alpha)$. Thus, to fit a given PDF by eq. (34) with a chosen value of α , β can be fixed by the variance of the PDF. The index α controls the shape of the PDF, and smaller α corresponds to fatter tails. The PDFs for $St = 0.1$ and 0.19 at $r = 1\eta$ almost have the same shape, and both can be fit by a stretched exponential function with $\alpha = 0.67$. This value of α is consistent with that (0.7) used to fit the PDF tails of the flow velocity difference at $\ell = 1.7$ (see Appendix B and Fig. 18). At $St = 0.39, 0.78$ and 1.55 , the best-fit values of α are 0.52, 0.48, and 0.49, respectively. The decrease of α in the St range from 0.1 to 0.78 also indicates increasing fatness of the PDF. The PDF shape at $St = 1.55$ is very close to that for $St = 0.78$ particles.

For particles with $3.11 \leq St \leq 49.7$, the PDF cannot be well fit by a single stretched exponential function. The PDFs of these particles are more complicated, due to the existence of sharp cusps at the center and the steepening trend of the PDF slope toward to the far tails. These features cannot be captured simultaneously by a single stretched exponential. It is, however, possible to fit these PDFs with a combination of two different stretched functions for the cusp and the tails respectively. We postpone a detailed study of the fitting functions for these intermediate particles to a future paper with simulations at a higher resolution. To give a quantitative idea for the PDF shape of these particles, here we simply list the best-fit α for the far tails without accounting for the central cusp. At $St = 3.11, 6.21, 12.4, 24.9$ and 49.7 , α for the PDF tails is found to be 1, 1.1, 1.3, 1.33, and 1.45, respectively. The stretched exponential fits for the PDF tails of $St = 24.9$ particles are shown as dotted lines in

Fig. 12 and 13, where the index α is set to 4/3. Such a 4/3 stretched exponential PDF was predicted by Gustavsson et al. (2008) assuming an exact Gaussian flow velocity field with Kolmogorov scaling and a rapid temporal decorrelation. An alternative derivation for the 4/3 stretched exponential is given in §6.3.2 using the physical picture of the PP10 model. Our derivation does not assume a short temporal correlation for the flow velocity, and is thus more general than that of Gustavsson et al. (2008).

Starting from $St = 99$, the central cusp becomes sufficiently small, leading to simpler PDF shapes. This allows the entire PDF to be satisfactorily fit by a single stretched exponential again. The measured α values for $St = 99, 199, 397$ and 795 are 1.5, 1.65, 1.75 and 1.9, respectively. Note that the PDF for $St = 795$ is close to Gaussian, but the best-fit value for α is actually 1.9 instead of 2. A similar trend of the PDF fatness and the best-fit α as a function of St was found in previous studies with low-resolution simulations (Sundaram & Collions 1997; Wang et al. 2000).

6.3.2. Physical picture for the PDF behavior

We give a detailed explanation for the behavior of the relative velocity PDF based on the physical picture of the PP10 model. The picture was illustrated in Fig. 1. We first consider particles with $\tau_p \lesssim T_L$. In §3.2.4, we showed that the 3D variance of the relative velocity of these particles may be roughly estimated by $\langle w^2 \rangle \simeq S_{ii}(R_p)$, where S_{ij} is the flow structure tensor and R_p is the primary distance. For simplicity, we have neglected the effect of the temporal correlation function, Φ_2 , which may provide a factor $(T(R_p)/\tau_p)$ of order of unity for particles with $\tau_p \lesssim T_L$. R_p was estimated by $R_p^2 = r^2 + \langle w^2 \rangle \tau_p^2$, assuming a ballistic backward separation within a friction timescale.

This picture for the rms relative velocity can be easily generalized to understand the behavior of the full PDF as a function of St . Consider a pair of particles at a distance r at time 0, and suppose their relative velocity is w . Applying the above physical picture to this particular particle pair, the relative speed, w , is estimated as $w \simeq \Delta u(r_p)$, where Δu is the flow velocity difference the two particles “saw” at $\tau = -\tau_p$ and r_p is the primary distance of this particle pair. We have used w and Δu to represent either the radial or tangential component. The generalized picture suggests that the particle relative velocity samples the PDF of the flow velocity difference in a certain way. An immediate implication of this picture is that the relative velocity would inherit intermittency of the turbulent flow. Assuming a ballistic separation again, r_p is estimated by $(r^2 + \zeta w^2 \tau_p^2)^{1/2}$, where $\zeta \simeq 3$ corresponds to the difference between the 3D separation velocity of the particle pair and the radial or tangential component. We point out that, for particles with $0.8 \lesssim St \lesssim 6.2$, it may not be valid to assume the contribution to the particle relative speed is dominated by the ballistic separation phase. As discussed in §6.1, the Richardson phase may provide a crucial contribution for these particles (see Fig. 5). However, using the ballistic assumption to estimate r_p would be sufficient for a qualitative understanding of the relative velocity PDF.

The above argument provides a satisfactory explanation

tion for our simulation results for the relative speed PDF, $P(w, \tau_p)$, of particles with $\tau_p \lesssim T_L$. At $St \ll 1$, the primary distance $r_p = (r^2 + \zeta w^2 \tau_p^2)^{1/2}$ for particle pairs at the inner part of the PDF (i.e., $w \simeq 0$) would be close to r . As a result, the central PDF follows the PDF, $P_u(\Delta u, \ell)$, of the flow velocity difference at $\ell = r$, as observed in the left panels of Figs. 12 and 13. At the tails of $P(w, \tau_p)$, r_p is larger, and w samples the flow velocity PDF $P_u(\Delta u, \ell)$ at larger ℓ . This implies that higher tails broaden faster because $P_u(\Delta u, \ell)$ is wider at larger ℓ . The effect may be viewed as a “self-amplification” of the PDF tails. The tail amplification makes the overall shape of $P(w, \tau_p, St)$ at $St \lesssim 1$ considerably fatter than the PDF of tracers. As St increases, r_p becomes larger at the same value of w , and the “amplification” proceeds toward the inner part of the PDF, as seen in the left panels of Figs. 12 and 13. The overall PDF broadening appears to be driven by the tail amplification. The amplification in the far PDF tails of $St \lesssim 1$ particles actually corresponds to the effects of slings or caustic formation. This is because the tail of $P(w, \tau_p)$ is associated with local flow regions with large velocity gradients, which are indeed where the slings or caustics are expected to occur. The tail amplification thus corresponds to the caustic contribution to the particle collision rate in the model of Wilkinson et al. (2006). On the other hand, the central part of the PDF represents the continuous (or S-T) contribution (Wilkinson et al. 2006).

As St increases above 1, the range of the central PDF that follows $P_u(\Delta u, \ell)$ becomes narrower, and the outer parts continue to get more extended. As discussed in §6.3.1, for $St \simeq 3.11$, the PDF tails show slope changes as they extend to high values of $|w|$. This is because different parts of the relative velocity PDF samples the flow PDF, $P_u(\Delta u, \ell)$, at different length scales. As the fatness of $P_u(\Delta u, \ell)$ decreases with increasing ℓ (see Appendix B and Fig. 18), the shape of $P(w, \tau_p)$ at higher tails becomes thinner. This thinning trend occurs at smaller values of $|w|$ for particles with larger τ_p . The trend explains why the overall shape of the PDF becomes less fat as St increases above $\simeq 1$. Note that the central cusp for $3.11 \lesssim St \lesssim 24.9$ keeps a sharp shape, corresponding to $P_u(\Delta u, \ell)$ at small ℓ .

The fact that the broadening of the PDF starts from the tail amplification is not captured by the PP10 model for the rms relative velocity in §3.2. The model only considers the 2nd-order moments of the flow velocity increment, the particle separation and the particle relative velocity, and thus implicitly assumes that the PDF shape does not change significantly with St , or the change occurs primarily at central part of the PDF. This gives rise to uncertainties in the prediction for the rms relative velocity because the PDF $P(w, St)$ is found to be very fat especially for $St \simeq 1$. Even the far tails give considerable contribution to the variance. The tail amplification also provides evidence for a positive correlation between the fluctuations of the flow velocity increment and the particle separation. The tails of $P(w, \tau_p)$ correspond to the PDF tails of both the flow velocity difference, Δu , and the primary distance, r_p . In other words, in flow regions with Δu larger than its rms value, the backward separation of particles is also faster than the rms separation rate. As discussed in §3.2 and §6.1, the PP10 model

neglects this correlation, and thus tends to underestimate the rms relative speed, particularly at intermediate St . The effect of the PDF tail amplification on the variance of the relative speed may be incorporated in the PP10 model if the correlation between Δu and r_p are properly accounted for.

In principle, if the PDF, $P_u(\Delta u, \ell)$, of the flow velocity increment as a function of the length scale ℓ is provided, one can derive the PDF of the relative velocity as a function of the particle size. For illustration, we consider a simple example, where the flow velocity is assumed to be exactly Gaussian. In that case, $P_u(\Delta u, \ell)$ is written as,

$$P_u(\Delta u, \ell) = \frac{1}{\sqrt{2\pi S(\ell)}} \exp\left(-\frac{\Delta u^2}{2S(\ell)}\right), \quad (35)$$

where $S(\ell)$ is the structure function or the variance of Δu at ℓ . To estimate the PDF, $P(w, \tau_p)$, of the particle relative speed w , we ask the question what the probability is for two nearby particles to see a flow velocity difference of w at time $\tau \simeq -\tau_p$. The probability is roughly estimated by $\propto P_u(w, r_p)$. Using eq. (35) for P_u and a ballistic particle separation for r_p , we have,

$$P(w, \tau_p) \propto \exp\left[-\frac{w^2}{2\xi S((r^2 + \zeta w^2 \tau_p^2)^{1/2})}\right], \quad (36)$$

where it is assumed all the uncertainties in the rough estimate can be absorbed in a parameter ξ . If r_p is in the inertial range of the flow, we may apply the Kolmogorov scaling for $S(\ell)$, i.e., $S(\ell) \propto \ell^{2/3}$. Further assuming that ξ is independent of w , we find that eq. (36) corresponds to a stretched exponential with $\alpha = 4/3$ (see eq. (34)) at $w \gg r/\tau_p$. This suggests that the relative speed of inertial-range particles would be non-Gaussian even if the flow statistics were exactly Gaussian. This non-Gaussianity originates purely from the particle dynamics, and is thus distinct from the non-Gaussianity inherited from the intermittency of the turbulent flow. In other words, we identified two sources, namely, the flow intermittency and the particle dynamics, that contribute to the non-Gaussianity of the particle relative velocity.

The predicted stretched exponential with $\alpha = 4/3$ was found to satisfactorily fit the PDF tails of $St = 24.9$ particles (see dashed lines in the left panels of Figs. 12 and 13). In this particular case, the two assumptions made in the derivation, i.e., Gaussianity and Kolmogorov scaling of the flow velocity, are both satisfied. However, we note that these assumptions are strong, and the validity of the 4/3 stretched exponential is quite limited. In fact, the prediction applies only to particles around the peak Stokes number, $St_m \simeq 30$. As discussed in §6.1, for particles with $St \simeq St_m$ in our simulation, the typical primary distance is around 200η . From Fig. 18, we see that, above this length scale, the PDF of the flow velocity increment is close to Gaussian. Therefore, the Gaussian assumption made in eq. (36) is valid for $St \gtrsim St_m$. Also, Fig. 3 shows that 200η is toward the end of but still within the inertial range of the flow, meaning that, only for particles with $St \lesssim St_m$, can one apply the Kolmogorov scaling around the primary distance, r_p . These suggest that the two assumptions are simultaneously met only at $St \simeq St_m$. Our finding that the 4/3 stretched exponential fits the PDF tails of $St = 24.9$ particles confirms

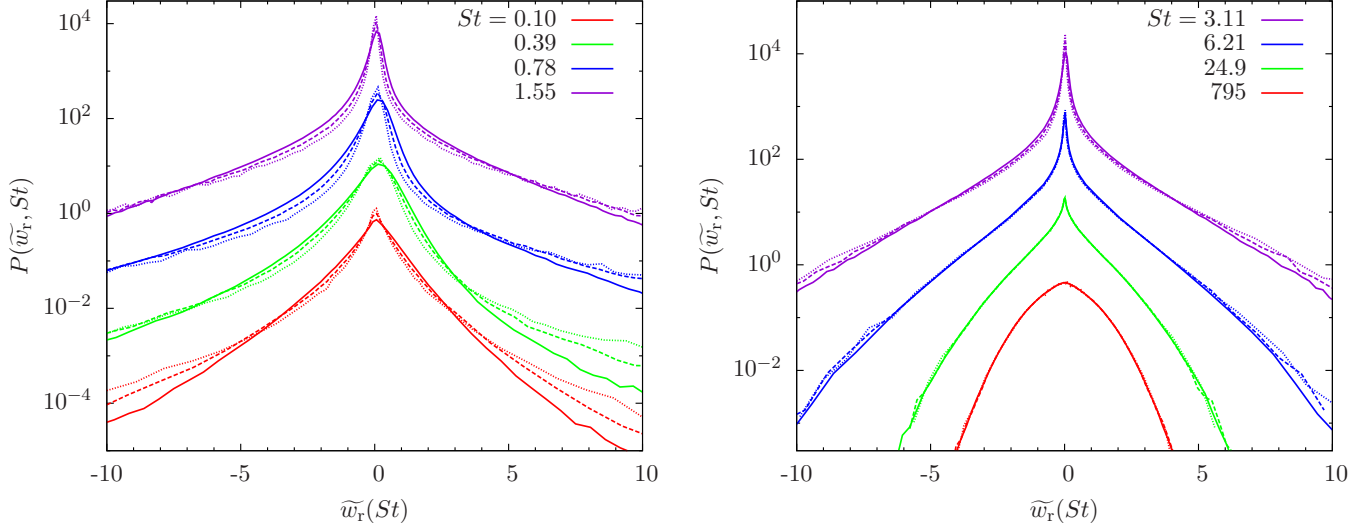


FIG. 14.— The normalized PDF of the radial relative velocity, w_r , as a function of the Stokes number St and the particle distance, r . All PDFs are normalized to have unit variance. The normalized relative speed is defined as $\tilde{w}_r = w_r / \langle w_r^2 \rangle^{1/2}$. The solid, dashed and dotted lines correspond to particle distance $r = 1, 0.5$ and 0.25η , respectively. The left panel plots the PDFs for particles with $St \leq 1.55$, while the right panel shows the results for larger particles with $St \geq 3.11$. In each panel, the bottom lines (i.e., $St = 0.1$ and $St = 795$) show the actual PDF values, and, for clarity, the upper lines for each larger St are shifted upward by a factor of 16.

the validity of our physical picture. But this stretched exponential form does not apply to the central part of the PDF, where both assumptions break down. We find that the $4/3$ stretched exponential can also acceptably fit the PDF tails for $St = 12.4$ particles, but not for other particles.

We next consider large particles with $St \gtrsim St_m$. The friction time of these particles is much larger than T_L , and, accounting for the effect of the memory time of the flow velocity, the relative velocity of a given particle pair is roughly estimated by $w \simeq \Delta u(r_p)(T_L/\tau_p)^{1/2}$ (see §3.2.4). Due to the large friction time, r_p is typically comparable to or even larger than the integral length scale, L , of the turbulent flow, meaning that $P_u(\Delta u, \ell)$ at $\ell \simeq r_p$ is close to Gaussian. Since the flow velocity PDF “seen” by $St \gtrsim St_m$ particles is typically Gaussian, the PDF shape for their relative velocity appears to be simpler than particles with intermediate τ_p (see Fig. 12 and 13). Using eq. (35) and the same analysis that led to eq. (36), we find $P(w, \tau_p) \propto \exp(-(w^2\tau_p)/(2\xi S(r_p)T_L))$ for $St \gtrsim St_m$. As τ_p increases, r_p increases, and $S(r_p)$ becomes less dependent on r_p or w . As a consequence, the shape of the relative velocity PDF becomes less fat. In the limit $\tau_p \rightarrow \infty$, $S(r_p)$ would become a constant, $2u^2$, and $P(w, \tau_p)$ finally approaches a Gaussian PDF with variance $\propto u^2 T_L/\tau_p$. As observed in Figs. 12 and 13, a nearly Gaussian PDF is indeed observed for the largest particles in our simulation.

6.3.3. The normalized PDF of the radial component

To see the shape of the PDF more clearly, we show in Fig. 14 the PDF of the radial component normalized to have unit variance. The radial relative speed is normalized to its rms value, $\langle w_r^2 \rangle^{1/2}$. The solid, dashed and dotted lines are normalized PDFs at $r = 1\eta, 0.5$ and 0.25η , respectively, and curves of different colors correspond to different St . The bottom curves in the left and right panels plot the actual PDF values for $St = 0.1$ and

$St = 795$, respectively. For clarity, we shifted the PDF curves upward by a factor of 16 for each larger St in the left panel or each smaller St in the right panel. The asymmetry of the PDFs at $St \lesssim 1.55$ is clearly seen.

As St increases from 0.1 to 1.55, the central part of the normalized PDF $P(\tilde{w}_r, St)$ becomes sharper. Note that, before normalization, the innermost part of the PDF is essentially the same for all particles in the range $0.1 \leq St \leq 1.55$ (see Fig. 12). Since the rms of w_r increases with St , normalizing w_r by its rms tends to make the central part of the PDF sharper. This sharpening explains the decreases of the ratio $\langle |w_r| \rangle / \langle w_r^2 \rangle^{1/2}$ with increasing St for $St \lesssim 1.55$, as shown in the inset of the left panel in Fig. 10. At $St \geq 3.11$, the central cusp in the normalized PDF becomes so narrow that both the 1st and 2nd order moments of the PDF are dominated by the outer parts of the PDF. Because the outer parts are less fat with increasing St , the ratio $\langle |w_r| \rangle / \langle w_r^2 \rangle^{1/2}$ starts to increase at $St \gtrsim 3.11$ (see Fig. 10). The behavior of $\langle |w_r| \rangle / \langle w_r^2 \rangle^{1/2}$ with St is consistent with the overall fatness of the PDF, i.e., it is smaller for fatter PDFs.

It is interesting to note that, as St increases from 0.1 to 0.39, the PDF, $P(\tilde{w}_r, St)$, at small to intermediate \tilde{w}_r in the right wing decreases. This corresponds to the decrease of $\langle w_r^2 \rangle_+^{1/2}$ in the St range from 0.1 to 0.39 (see the left panel of Fig. 8). The physical reason is that the right wing corresponds to separating particle pairs, and the particle distance decreases toward the near past. This leads to a decrease in the primary distance, r_p , for separating pairs with small to intermediate \tilde{w}_r , as St increases from 0.1 to 0.39. For the far right tail with large w_r , the particle pairs may quickly move past each other, and their distance starts to increase within a friction time in the past. This explains why the far right tail of $St = 0.39$ becomes slightly broader than that of $St = 0.1$ particles. As St increases to 0.78, the PDF at immediate to large \tilde{w}_r in the right wing is significantly amplified, while the effect of the “initial” decrease of the particle distance

is still visible at small positive \widetilde{w}_r . For $St > 0.78$, the particle memory is longer, and the “initial” separation phase does not cause a significant difference in the primary distance r_p for separating and approaching particle pairs. The two wings become symmetric at $St \gtrsim 1.55$.

For particles with $St \lesssim 3.11$, the normalized PDF has a dependence on r . As r decreases, the central part of the normalized PDF becomes sharper, and the outer parts become slightly broader, leading to a fatter PDF shape at smaller r . This can be understood as follows. Before the normalization, the central part of the PDF follows the flow velocity difference at r , and its width thus decreases linearly with r . On the other hand, the dependence of the tails on r is weaker because the primary distance, r_p , for particle pairs in the outer parts of the PDF has a larger contribution from backward separation. Also, as r decreases, the contribution from the outer parts to the variance increases. Consequently, normalizing the PDF to unit variance gives a sharper central part and broader tails at smaller r . At $St \gtrsim 6.21$, the PDF is essentially independent of r . For these larger particles, r_p is mainly contributed by the backward separation even for pairs lying close to the central part of the PDF, and thus the PDF is independent of r for w_r in any range. The r -dependence of the normalized PDF shape for $St \lesssim 6.21$ explains the decrease of the ratio $\langle |w_r| \rangle / \langle w_r^2 \rangle^{1/2}$ with decreasing r , as seen in the inset of the left panel of Fig. 10 (see §6.2).

6.3.4. The tangential PDFs for approaching and separating particle pairs

In Fig. 15, we compare the PDFs of the tangential component of the relative velocity for approaching ($P(w_t|w_r < 0, St)$) and separating ($P(w_t|w_r > 0, St)$) particle pairs. For $St \lesssim 6.2$, the PDF of approaching particles is broader than the separating ones, consistent with our earlier results for the rms relative speeds, $\langle w_t^2 \rangle_{\mp}^{1/2}$, shown in the left panel of Fig. 8. Again, this is because, for a given “initial” value r , the distance of approaching particles was larger in the near past than the separating ones. Therefore, the PDF of the relative velocity for approaching pairs samples the PDF, $P_u(\Delta u, \ell)$, of the flow difference at larger ℓ . Since the width of $P_u(\Delta u, \ell)$ increases with ℓ , $P(w_t|w_r < 0, St)$ is expected to be broader than $P(w_t|w_r > 0, St)$. At $St \gtrsim 12.4$, the PDFs for approaching and separating pairs are almost equal. For these larger particles, the primary distance at $\tau \simeq -\tau_p$ becomes insensitive to the initial conditions at $\tau = 0$. Although $P(w_t|w_r > 0, St)$ for separating particle pairs is not relevant for particle collisions, a comparison of $P(w_t|w_r < 0, St)$ with $P(w_t|w_r > 0, St)$ provides an interesting illustration for the role of the backward separation of particle pairs in determining their relative velocity.

6.3.5. The normalized PDF of the 3D amplitude

Fig. 16 plots the PDF of the 3D amplitude, $|\mathbf{w}|$, of the relative velocity for approaching particle pairs at $r = 1\eta$. For each St , the amplitude $|\mathbf{w}|$ is normalized to the rms value $\langle w^2 \rangle_-^{1/2}$, i.e., $\widetilde{|\mathbf{w}|} = |\mathbf{w}| / \langle w^2 \rangle_-^{1/2}$, so that all the PDFs shown here have unit variance. The rms of the 3D amplitude, $\langle w^2 \rangle_-^{1/2}$, for approaching pairs has been shown in Fig. 8. For a particle pair colliding with a rel-

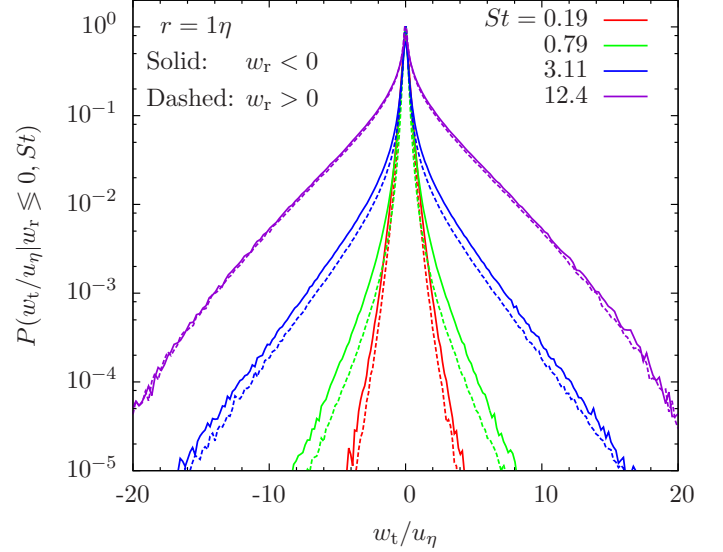


FIG. 15.— The PDF of the tangential relative speed for approaching ($w_r < 0$; solid) and separating ($w_r > 0$; dashed) particle pairs. At $St < 12.4$, the PDF, $P(w_t|w_r < 0, St)$, for approaching pairs is wider than that for separating pairs with $w_r > 0$. Above $St = 12.4$, the two conditional PDFs almost coincide.

ative velocity \mathbf{w} , the total collision energy in the center-of-mass frame is $\frac{1}{2}m_\mu|\mathbf{w}|^2$ where m_μ is the reduced mass. Therefore, the PDF of the 3D amplitude can be easily converted to the PDF of the collisional energy. As mentioned earlier, for particles of a given size, the PDF of $|\mathbf{w}|$ determines the fractions of collisions that result in sticking, bouncing or fragmentation.

The left and right panels of Fig. 16 show simulation results for small ($St \lesssim 1.55$) and large ($St \gtrsim 3.11$) particles, respectively. The thin dashed line in the left panel corresponds to approaching tracer particles ($St = 0$), while the dashed line in right panel is the normalized PDF of a Gaussian vector with three independent components of equal variance. The PDF for tracer particles in the left panel is already highly non-Gaussian, as can be seen from a comparison with the dashed line in the right panel. In the left panel, we see that the degree of non-Gaussianity increases as St increases from 0 to $\simeq 1$. At larger St , the PDF peaks at smaller $|\mathbf{w}|$, indicating a larger probability of collisions with lower collision energy. The PDF around the rms value (i.e., $|\mathbf{w}| \simeq 1$) decreases with increasing St , and more probability is distributed toward smaller and larger values of $|\mathbf{w}|$. This corresponds to the sharpening of $P(w_r, St)$ and $P(w_t|w_r < 0, St)$ in the central part and the broadening of the tail parts in this St range (see Figs. 12, 13 and 14).

The trend is reversed as St increases further above $St \simeq 3.11$. The peak of the PDF moves back to around the rms value, $|\mathbf{w}| \simeq 1$, at $St \gtrsim 49.7$. The PDF eventually approaches Gaussian in the limit $\tau_p \gg T_L$. However, note that, even for $St = 795$ particles, the PDF shows a significant difference from the Gaussian distribution at small collision speeds. The strong non-Gaussianity in the amplitude of the collision velocity has interesting implications for the growth and evolution of dust particles in planetary disks. The shape of the PDFs shown in Fig. 16 suggests that there are more collisions with extremely

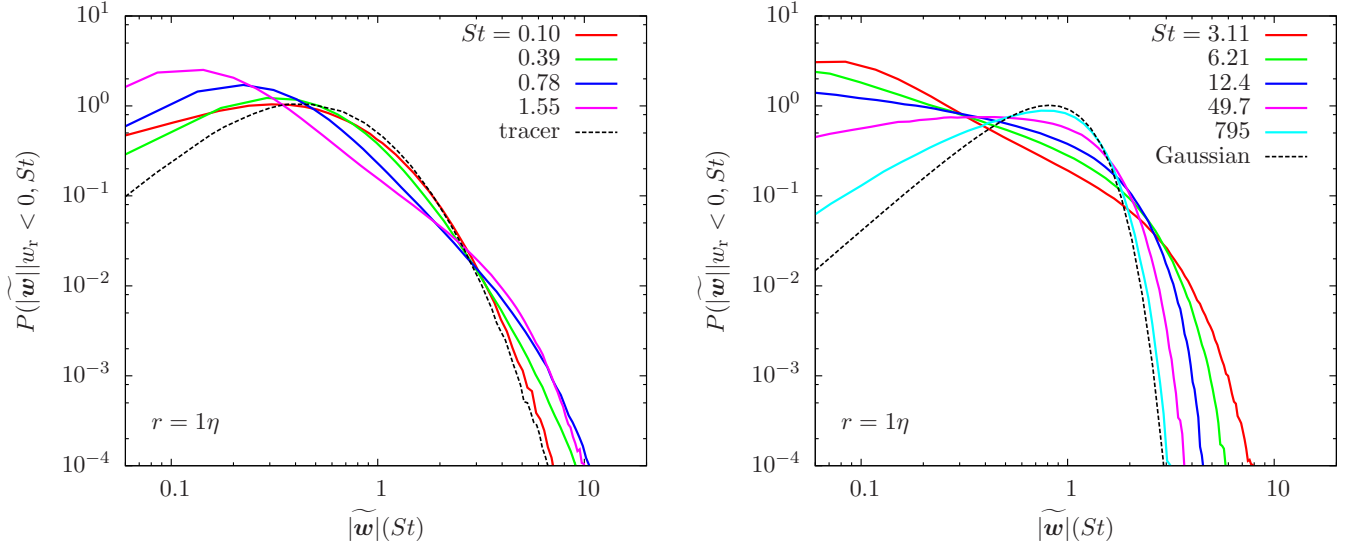


FIG. 16.— The PDF of the 3D amplitude, $|\mathbf{w}|$, of the relative velocity for approaching particle pairs with $w_r < 0$. For each St , the amplitude, $|\mathbf{w}|$, is normalized to its rms value, and the PDF is normalized to have unit variance. In the left panel, the solid lines show results for $St \leq 1.55$, and the dashed line corresponds to the PDF for tracer particles ($St = 0$). The right panel plots PDFs for $St \geq 3.11$. The dashed line in this panel is the normalized PDF, $\sqrt{\frac{54}{\pi}} |\mathbf{w}|^2 \exp(-3|\mathbf{w}|^2/2)$, with unit variance for the amplitude of a Gaussian vector.

large ($|\mathbf{w}| \gg 1$) or small ($|\mathbf{w}| \ll 1$) relative speeds than estimated from a Gaussian distribution. This may induce interesting and complicated effects to the modeling of the collision process. The high probability for collisions with small relative speed would favor sticking, while there are also more collisions that would result in fragmentations. The competition of the two opposite effects would determine whether the non-Gaussian PDF of the collision velocity accelerates or slows down the particle growth. A coagulation model incorporating the non-Gaussian statistics of the collision speed would give a more realistic prediction for the evolution of the size distribution of dust particles in protoplanetary disks.

We find that, for St in the range from 0.78 to 6.22, the PDF shows an extended power-law range at intermediate values of $|\mathbf{w}|$. For example, at $St = 0.78$, the PDF goes like $|\mathbf{w}|^{-2.4}$ in the range $0.5 \leq |\mathbf{w}| \leq 4$. The slope of the PDF in the power-law range becomes shallower with increasing St . For $St = 1.55$, $St = 3.11$ and $St = 6.22$, the power-law exponent of the PDF in the intermediate range is -1.8 , -1.3 , and -0.8 , respectively.

The PDF of the amplitude $|\mathbf{w}|$ can be easily computed from the PDFs of the radial and tangential components, if the three components are completely independent. In that case, one may obtain fitting functions for $P(|\mathbf{w}|)$ using the fitting functions discussed earlier for the PDFs $P(w_r, St)$ and $P(w_t | w_r < 0, St)$, of colliding particle pairs. Alternatively, one could directly fit the PDF of $|\mathbf{w}|$ with simple function forms or tabulate it as a function of St . We defer this to a later paper using simulations at a higher resolution.

7. CONCLUSIONS

We investigated the turbulence-induced relative velocity of inertial particles using both theoretical modeling and numerical simulations. We conducted a 512^3 simulation of a weakly compressible turbulent flow with an rms Mach number of 0.1, and evolved 14 species of inertial particles with friction timescales, τ_p , covering the

entire scale range of the flow. The Stokes number, St , of the particles spans about 4 order of magnitudes, ranging from 0.1 to 800. We used the simulation to test the theoretical model for the rms velocity of inertial particles by Pan & Padoan (2010), in the case of identical particles (equal friction times). We also examined the particle collision kernel and the probability distribution of the relative velocity as a function of St . In the following, we summarize the main results of this work.

1. We introduced the formulation for the particle relative velocity by Pan & Padoan (2010), which reveals an insightful physical picture. The relative velocity of two nearby identical particles is determined by the memory of the flow velocity difference along their trajectories in the past, and hence depends on the separation behavior of particle pairs backward in time. We adopted a two-phase separation behavior consisting of a ballistic and a Richardson phase, and showed that the model predicts a $St^{1/2}$ scaling for inertial-range particles in turbulent flows with an extended inertial range. The model can correctly reproduce the expected behaviors in the extreme limits of large and small particles. We found that the model prediction for the rms relative velocity is in good agreement with the simulation results. The physical picture also provides a successful explanation for the behavior of the probability distribution function of the relative velocity as a function of St .
2. To improve the understanding of the inertial particle statistics, we analyzed both Lagrangian and Eulerian temporal correlation functions in the simulated flow. While the flow velocity along the trajectory of a small particle is close to Lagrangian, the velocity seen by a large particle may be better approximated by Eulerian. The Eulerian and Lagrangian correlation timescales, T_E and T_L , were found to be close to each other, with T_E slightly

larger (by 10%). Our model predictions for both 1-particle rms velocity and the rms relative speed between two identical particles depend mainly on the correlation timescale and are insensitive to the function form of the temporal correlation. This provides a validation for using the Lagrangian correlation function form for all particles.

3. Our simulation shows that, in the small particle limit ($St \ll 1$), the 3D rms relative velocity of particle pairs at a distance $r = \eta$ is constant, $\simeq u_\eta/\sqrt{3}$, consistent with the Saffman-Turner prediction. It starts to rise at $St \gtrsim 1$, and peaks for particles with $\tau_p \simeq 2T_L$, corresponding to $St = St_m \simeq 30$ in our simulated flow. As expected, the relative velocity scales with St as $St^{-1/2}$ in the limit $\tau_p \gg T_L$ (or $St \gg St_m$). The PP10 model with reasonable parameters provides an excellent fit to the simulation data for the 3D rms. The maximum relative speed at St_m is twice smaller than the rms velocity of the turbulent flow, indicating a factor of $\simeq 2$ overestimate by the commonly-used models of Volk et al. (1980) and its later developments (e.g., Markiewicz et al. 1991; Cuzzi & Hogan 2003; Ormel & Cuzzi 2007).

The rms relative speed of small particles ($St \lesssim 6$) has a dependence on r . The dependence for the smallest particles ($St = 0.1 - 0.2$) in our simulated flow at $r < \eta$ was found to be slower than the linear scaling predicted by the Saffman-Turner formula, suggesting considerable contributions from the sling events or caustic formation. In the context of the PP10 model, these events provide a contribution to the backward particle separation. For larger particles with $St \gtrsim 6$, the backward separation at a friction timescale ago becomes insensitive to the initial distance r , and the rms relative speed is thus independent of r .

The rms relative speeds in the radial and tangential directions are nearly equal for all $St \gtrsim 0.1$ particles at $r \lesssim 1\eta$. For $St \ll 1$ particles, this is in contrast to the Saffman-Turner formula, which predicts the tangential rms is larger than the radial rms by $\sqrt{2}$. This near equality suggests the direction of the relative velocity is almost completely randomized with respect to the particle separation \mathbf{r} . The randomization is caused by the derivation of particle trajectories from the fluid elements and/or the stochastic backward separation of particle pairs.

For $St \lesssim 6$ particles, approaching pairs that may lead to collisions were found to have a larger relative speed than separating ones. The physical reason is that the distance between approaching particles is larger than separating ones in the near past. This implies that the collision speed of $St \lesssim 6$ particles is larger than the overall relative velocity estimated from all particle pairs at a given distance.

4. We computed the particle collision kernel from the simulation data using both spherical and cylindrical formulations. In particular, we accounted for the effect of turbulent clustering. It was found that the two formulations give nearly equal predictions

for all particles. The collision kernel per unit cross section shows an abrupt rise as St increases toward 1, which may be viewed as an activation process corresponding to the formation of caustics. As St increases from $\simeq 1$ to St_m , the normalized collision kernel is roughly constant, increasing only slightly by 50%. It finally decreases as $St^{-1/2}$ for large particles with $\tau_p \gg T_L$. The normalized kernel is independent of the particle distance, r , for $St \gtrsim 1$, due to the cancellation of the scalings of the radial distribution function and the collision velocity with r . On the other hand, for $St \lesssim 1$ particles, the kernel shows a dependence on r , which needs to be accurately evaluated for applications to protoplanetary disks, where the dust grains are much smaller than the Kolmogorov scale. At sufficiently small r , the effect of caustics may provide a dominant and r -independent contribution. Existing coagulation models for dust particle growth do not capture these important features. We will provide fitting functions for the collision kernel as a function of St in a separate study.

5. The probability distribution function for the particle relative velocity is highly non-Gaussian, exhibiting extremely fat tails. For small particles with $St \lesssim 1$, the effects of the particle memory and the backward separation lead to a self-amplification starting at the far tails, which corresponds to slings or caustic formation. As St increases, the amplification becomes stronger and proceeds toward the inner part of the PDF, causing an increase in the fatness of the overall PDF shape. On the other hand, as St increases above $\simeq 1$, the PDF shape becomes less fat. For these larger particles, the relative velocity samples the PDF, $P_u(\Delta u, \ell)$, of the flow velocity increment, Δu , at larger scales, ℓ . Since the fatness of P_u decreases with increasing ℓ , the PDF of the particle relative velocity keeps thinning with increasing St . At a particle distance of $r = 1\eta$, the PDF shape is fattest at $St \simeq 1$, with a kurtosis of $\simeq 30$. For $St \lesssim 6$, the PDF shape also depends on r and becomes even fatter at $r \lesssim 1\eta$.

Using the physical picture of the PP10 model, we identified two sources of non-Gaussianity for the particle relative velocity: the inheritance of intermittency from the turbulent flow and an intrinsic contribution from the particle dynamics. We also predicted a 4/3 stretch exponential PDF, $\propto \exp(-(|w|/\beta)^{4/3})$, for inertial-range particles in an exactly Gaussian velocity field with Kolmogorov scaling. This 4/3 stretched exponential is actually observed in the PDF tails for particles with $St \simeq St_m$ (or $\tau_p \simeq 2T_L$), confirming the validity of our physical picture.

The PDF of the particle collision velocity is expected to play a crucial role in the growth of dust particles in protoplanetary turbulence, as it determines the fractions of collisions resulting in sticking, bouncing and fragmentation. The PDF of the 3D amplitude of the relative velocity shows much higher probabilities of extremely small and large collision speeds than estimated from a Gaussian

PDF. Only for particles with $\tau_p \gtrsim 50T_L$ does the PDF approach Gaussian. The highly non-Gaussian nature of the collision velocity needs to be incorporated into dust coagulation models for protoplanetary disks.

In this work, we have focused on the monodisperse case with identical particles. A systematic analysis for the relative velocity of different particles will be conducted in a follow-up paper. Future simulations at higher resolutions will further improve our understanding of the problem.

For example, a 1024^3 simulation would help verify the existence of the predicted $St^{1/2}$ scaling for inertial-range particles by various models, which is not yet confirmed numerically. A computationally more demanding simulation with a much larger number of inertial particles would allow us to examine the particle statistics at small scales, $r \ll \eta$, and to quantify the r -dependence of the collision kernel and the caustic contribution for $St \lesssim 1$ particles. The results of these future studies will significantly improve the formulation of coagulation models to compute the evolution of dust particles in protoplanetary disks.

APPENDIX

A SEPARATION OF TRACER PARTICLE PAIRS

Our model for the relative velocity of inertial particles depends on the particle pair dispersion backward in time (§3.2.3). We adopted a two-phase behavior, consisting of a ballistic and a Richardson phase. To constrain the Richardson constant, g , in the latter phase, we study the dispersion of tracer particles in our simulated flow, and take the measured value of g as a reference for inertial particles.

In Fig. 17, the three solid lines from bottom to top show the backward-in-time separation of tracer particle pairs with “initial” distance $r = 1\eta$, 2η and 4η , respectively. We subtracted r^2 from the separation variance, $d^2(\tau)$. The “initial” time is set to 0, and τ is negative for the backward separation. As seen in Fig. 17, the particle separation at small $|\tau|$ shows a ballistic behavior with $d^2(\tau) - r^2$ increasing as τ^2 . The physical origin of the ballistic behavior is that the velocity at which two tracer particles separate is determined by the flow velocity difference across the particle distance and thus remains roughly constant before the particle distance becomes significantly larger than the initial value. This ballistic phase of the tracer particles is physically different from that of inertial particles discussed in §3.2.3. For inertial particles, the duration and the separation speed of the ballistic phase depend on the particles’ memory timescale. But for tracer particles, the ballistic phase is determined purely by the initial particle distance. For $r \lesssim 4\eta$, the ballistic phase lasts for a few Kolmogorov timescales.

The Richardson separation behavior (the $|\tau|^3$ scaling) is observed at large $|\tau|$ after the particle separation enters the inertial range of the flow. In the bottom solid curve for $r = 1\eta$, a $|\tau|^3$ scaling exists in a very limited range. A rough estimate of the Richardson constant in that range gives $g \simeq 0.5$. Consistent with previous studies (e.g., Sawford et al. 2008), the time range that exhibits the Richardson scaling becomes broader as r increases to 4η . This allows a more accurate estimate of g , and we find $g \simeq 1.2$ for $r = 4\eta$, consistent with the experimental results of Berg et al. (2006). Similar to Sawford et al. (2008), the measured g has a dependence on r . If the inertial range of the flow is considerably

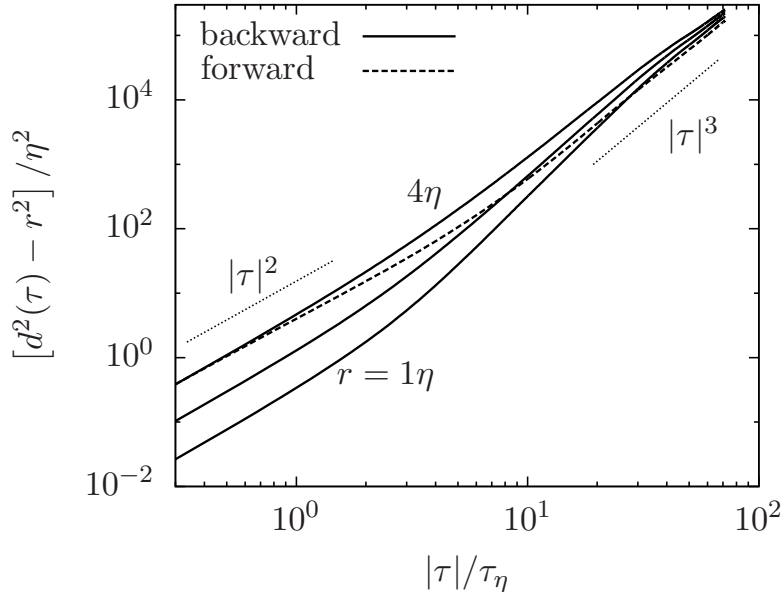


FIG. 17.— Separation of tracer particle pairs in our simulated flow. The time lag and the particle separation are normalized to the Kolmogorov time and length scales. Solid lines from top to bottom correspond to the backward separation of particle pairs with “initial” distance $r = 1, 2$ and 4η , respectively. The dashed line plots the forward separation with $r = 4\eta$. The initial time is set to 0, and τ is negative (positive) for the backward (forward) separation. The separation shows a ballistic phase and a Richardson behavior at small and large $|\tau|$, respectively.

broadener and the Richardson separation behavior exists in a larger time range, then the curves for different initial distances are expected to converge at sufficiently large time lags, with g eventually approaching a universal value.

The dashed line in Fig. 17 plots the forward-in-time pair dispersion of tracer particles at $r = 4\eta$. A comparison with the top solid line shows that the forward separation is slower than the backward separation. For $r = 4\eta$, g is estimated to be 0.5 in the forward separation, about twice smaller than the value (1.2) for the corresponding backward separation. This is consistent with the result of Berg et al. (2006). A similar trend is also found for $r = 1\eta$ and 2η . The faster backward separation will be explained in Appendix B based on the PDF of the longitudinal difference, Δu_r , of the flow velocity. In our model for the relative velocity of inertial particles, it is the backward separation that is relevant, and the purpose of showing an example for the forward separation in Fig. 17 is to illustrate the difference between the forward and backward separations.

The Richardson constant, g , in the tracer-like phase of inertial particle separation may be different from tracers. However, it is reasonable to assume that g for the backward separation of inertial particles lies in a similar range. Like tracers, the value of g for inertial particles may also depend on the initial distance, r . In §6.1, we adjusted value of g in our model to obtain best fits to the simulation data for the particle relative velocity at different r .

B THE PDFS OF THE TURBULENT VELOCITY FIELD

In this Appendix, we analyze the probability distribution functions (PDF) of the flow velocity increments at different length scales. As discussed in §6.3, the statistics of the flow velocity increment leaves a signature in the PDF of the relative velocity of inertial particles. We measured the PDFs, $P_u(\Delta u_r, \ell)$ and $P_u(\Delta u_t, \ell)$, of the longitudinal and transverse increments as a function of the length scale, ℓ . Similar to the computation of the structure functions in §4.2, the PDF measurement also uses the velocity differences along the three directions of the simulation grid. The variances of $P_u(\Delta u_r, \ell)$ and $P_u(\Delta u_t, \ell)$ correspond to the longitudinal ($S_{ll}(\ell)$) and transverse ($S_{nn}(\ell)$) structure functions, which have been shown in Fig. 3 (see §4.2). Clearly, the PDFs are wider at larger scales as the structure functions increase with ℓ . Furthermore, $P_u(\Delta u_t, \ell)$ is wider than $P_u(\Delta u_r, \ell)$ because $S_{nn}(\ell) \geq S_{ll}(\ell)$ at all ℓ (see Fig. 3).

To better see the PDF *shape* as a function of ℓ , we normalized the PDFs at each scale to have unit variance. The radial and transverse velocity increments are normalized to their rms values, i.e., $\widetilde{\Delta u_r}(\ell) \equiv \Delta u_r(\ell)/S_{ll}^{1/2}(\ell)$ and $\widetilde{\Delta u_t}(\ell) \equiv \Delta u_t(\ell)/S_{nn}^{1/2}(\ell)$. The left panel of Fig. 18 shows the normalized PDF, $P_u(\widetilde{\Delta u_r}, \ell)$, of the radial increment. Except at the largest scales, the PDF is negatively skewed. For inertial-range scales, this can be understood from Kolmogorov's 4/5 law, $\langle \Delta u_r(\ell)^3 \rangle = -\frac{4}{5}\bar{\epsilon}\ell$, which indicates a negative skewness for the PDF of Δu_r . The connection of the 3rd order moment of Δu_r to the energy dissipation rate suggests that the skewness originates from the dissipative nature of turbulence. The skewness of the PDF of Δu_r also provides an explanation for the faster backward separation found in Appendix A. The left and right tails of $P_u(\widetilde{\Delta u_r}, \ell)$ correspond to tracer pairs receding from each other backward and forward in time, respectively. The broader left tail of the PDF thus suggests that the backward separation of tracer particles is faster than the forward case. The argument also implies that the time-asymmetry (or irreversibility) of the tracer pair separation is related to the dissipative nature of a turbulence system. Unlike $P_u(\widetilde{\Delta u_r}, \ell)$, the PDF,

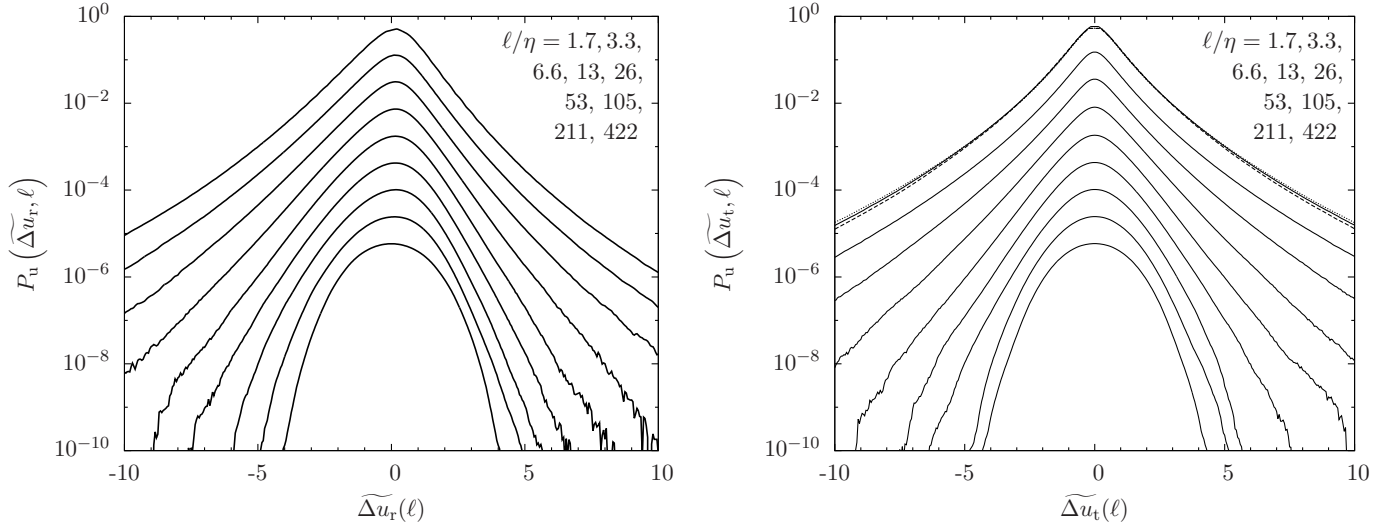


FIG. 18.— The normalized PDFs of the flow velocity increment in the radial (left panel) and transverse (right panel) directions as a function of length scale, ℓ . The normalized velocity increments are defined as $\widetilde{\Delta u_r}(\ell) \equiv \Delta u_r(\ell)/S_{ll}^{1/2}(\ell)$ and $\widetilde{\Delta u_t}(\ell) \equiv \Delta u_t(\ell)/S_{nn}^{1/2}(\ell)$. The top line in each panel plots the exact PDF at $\ell = 1.7\eta$ (the cell size), and, for clarity, the PDF at each larger ℓ is shifted downward by a factor of 4. Except at the largest scales, the PDF, $P_u(\widetilde{\Delta u_r}, \ell)$, of the radial increment has a negative skewness, whereas $P_u(\widetilde{\Delta u_t}, \ell)$ for the transverse increment is symmetric at all scales. The PDF tails are highly non-Gaussian or intermittent at small scales. With increasing ℓ , the PDFs become less fat and approach Gaussian at the largest scales. In the right panel, the dashed and dotted lines for $\ell = 1.7\eta$ are the normalized PDFs of the transverse increment conditioned on $\Delta u_r < 0$ and $\Delta u_r > 0$, respectively.

$P_u(\widetilde{\Delta u_t}, \ell)$, of the transverse increment in the right panel is symmetric about the origin, $\Delta u_t = 0$, at all ℓ , as expected from statistical isotropy.

Both $P_u(\widetilde{\Delta u_r}, \ell)$ and $P_u(\widetilde{\Delta u_t}, \ell)$ are close to Gaussian at the largest scales, $\ell = 211\eta$ (1/4 box size) and 422η (1/2 box size), of the simulated flow. This is consistent with the Gaussian 1-point statistics in fully developed turbulence. At smaller ℓ , the PDFs become non-Gaussian, and the tails keep getting fatter with decreasing ℓ , a phenomenon known as intermittency in turbulence theory (Frisch 1995). As mentioned in the text, we use the word “fat” (or “thin”) specifically for the shape of the PDF, while “broad” (or “narrow”) refers to the extension or width of the PDF. The smallest scale, 1.7η , in the figure corresponds to the size, Δx , of the computational cell. The shape of the normalized PDF is expected to remain unchanged once ℓ becomes smaller than $\sim \eta$. Physically, the viscosity acts to smooth the velocity field and makes it differentiable in the dissipation range, and consequently the velocity increment across any scale $\ell \lesssim \eta$ is proportional to the local velocity gradient, whose PDF is fixed. In our simulation, the velocity field inside a computation cell is obtained by interpolation, and thus the PDF of the velocity difference below the cell size is controlled by the velocity gradient PDF at Δx . In §6.3, we showed that the trend of the PDF shape of the flow velocity difference with ℓ has interesting effects on the PDF of the relative velocity of inertial particles as a function of the particle inertia.

The tails of $P_u(\widetilde{\Delta u_t}, \ell)$ for the transverse increment can be approximately described by stretched exponentials, P_{se} (see eq. (34) in §6.3). At largest scales, $P_u(\widetilde{\Delta u_t}, \ell)$ are nearly Gaussian, and $\alpha = 2$. With decreasing ℓ , α decreases, corresponding to fatter tails. For example, the best-fit α for $P_u(\widetilde{\Delta u_t})$ at $\ell = 26\eta$ is $\simeq 1$, and it further decreases to $\simeq 0.72$ at $\ell = 1.7\eta$. Due to the asymmetry of the radial PDF, $P_u(\widetilde{\Delta u_r}, \ell)$, one needs to obtain the fits separately for the left and right wings. Comparing the left wing of $P(\widetilde{\Delta u_r}, \ell)$ with $P_u(\widetilde{\Delta u_t}, \ell)$, we see that their shape has a similar level of fatness at the same scale ℓ . In fact, the best-fit α for the left tail of $P_u(\widetilde{\Delta u_r}, \ell)$ is very close to that for $P_u(\widetilde{\Delta u_t}, \ell)$. We also find that the best-fit values of α for the left and right tails of $P_u(\widetilde{\Delta u_r}, \ell)$ are close to each other, indicating that the two tails have a similar shape and differ only in the amplitude of fluctuations.

To quantify the fluctuation amplitudes in the left and right wings of $P_u(\Delta u_r, \ell)$, we define the variances in the two wings as $\langle \Delta u_r^2 \rangle_- = \int_{-\infty}^0 \Delta u_r^2 P_u(\Delta u_r, \ell) d\Delta u_r / \int_{-\infty}^0 P_u(\Delta u_r, \ell) d\Delta u_r$ and $\langle \Delta u_r^2 \rangle_+ = \int_0^{\infty} \Delta u_r^2 P_u(\Delta u_r, \ell) d\Delta u_r / \int_0^{\infty} P_u(\Delta u_r, \ell) d\Delta u_r$. The definition of $\langle \Delta u_r^2 \rangle_{\mp}$ is similar to $\langle w_r^2 \rangle_{\mp}$ for the relative velocity of inertial particles (§6.1.3.) We find that the ratio of $\langle \Delta u_r^2 \rangle_-$ to $\langle \Delta u_r^2 \rangle_+$ is $\simeq 1.47$ at $\ell = 1.7\eta$. This ratio decreases with increasing ℓ , and reaches unity at the largest scales. The variances of the left and right wings of $P_u(\Delta u_r, \ell)$ was used in the discussion on the relative velocity of approaching and separating particle pairs in the $St \ll 1$ limit (see §6.1.3). We also considered the PDF of Δu_t conditioned on the sign of Δu_r . We denote two conditional PDFs as $P_u(\Delta u_t | \Delta u_r \leq 0, \ell)$ and their variances as $\langle \Delta u_t^2 \rangle_{\mp} \equiv \int_{-\infty}^{\infty} \Delta u_t^2 P_u(\Delta u_t | \Delta u_r \leq 0, \ell) d\Delta u_t$. At $\ell = 1.7\eta$, $\langle \Delta u_t^2 \rangle_-$ is found to be larger than $\langle \Delta u_t^2 \rangle_+$ by 28%. In the right panel of Fig. 18, the dashed and dotted lines show the normalized conditional PDFs, $P_u(\widetilde{\Delta u_t} | \Delta u_r < 0, \ell)$ and $P_u(\widetilde{\Delta u_t} | \Delta u_r > 0, \ell)$, at $\ell = 1.7\eta$. The shapes of the two conditional PDFs are close to that of the overall PDF, $P_u(\widetilde{\Delta u_t}, \ell)$. Again, the conditional variances and PDFs of Δu_t are useful to understand the differences in the relative velocity of approaching and separating inertial particle pairs with $St \ll 1$ (§6.1.3 and 6.3.4).

REFERENCES

- Abrahamson, J. 1975, *Chem. Eng. Sci.* 30, 1371
 Ayala, O., Rosa, B. & Wang, L.-P. 2008, *New J. Physics*, 10, 075016
 Balkovsky, E., Falkovich, G., & Fouxon, A. 2001, *Phys. Rev. Lett.*, 86, 2790
 Bec, J., Biferale, L., Cencini, M., Lanotte, A. S., & Toschi, F. 2009, arXiv: 0905.1192v1 [physics.flu-dyn]
 Bec, J., Biferale, L., Lanotte, A. S., Scagliarini, A., & Toschi, F. 2010, *J. Fluid Mech.*, 645, 497
 Berg, J., Luthi, B., Mann, J. & Ott, S. 2006, *Phys. Rev. E.*, 74, 016304
 Birnstiel, T., Ormel, C. W., & Dullemond, C. P. 2011, *A&A*, 525, 11
 Blum, J. & Wurm, G. 2008, *ARAA*, 46, 21
 Brandenburg, A. & Dobler, W. 2002, *Computer Physics Communications*, 147, 471
 Chambers, J. E. 2010, *Icarus*, 208, 505
 Chiang, E. 2008, *ApJ*, 675, 1549
 Cuzzi, J. N. & Hogan R. C. 2003, *Icarus*, 164, 127
 Cuzzi, J. N., Hogan, R. C., & Bottke, W. F. 2010, *Icarus*, 208, 518
 Cuzzi, J. N., Hogan, R. C., Paque, J. M., & Dobrovolskis, A. R. 2001, *ApJ*, 546, 496
 Cuzzi, J. N., Hogan, R. C. & Shariff, K. 2008, *ApJ*, 687, 1432
 de Jong J., Salazar, J. P. L. C., Woodward, S. H., Collins, L. R., & Meng, H. 2010, *Int. J. Multiphase Flow*, 36, 324
 Dullemond, C. P. & Dominik, C. 2005, *A&A*, 434, 971
 Falkovich, G., Fouxon, A., & Stepanov, M. G. 2002, *Nature*, 419, 151
 Falkovich, G., & Pumir, A. 2004, *Physics of Fluids*, 16, L47
 Falkovich, G. & Pumir, A. 2007, *J. Atmos. Sci.* 64, 4497
 Freytag, B., Allard, F., Ludwig, H.-G., Homeier, D., & Steffen, M. 2010, *A&A*, 513, A19
 Frisch, U. 1995, *Turbulence. The Legacy of AN Kolmogorov* (Cambridge University Press, Cambridge)
 Girimaji, S. S. & Pope, S. B. 1990, *J. Fluid. Mech.*, 220, 427
 Goldreich, P., & Ward, W. R. 1973, *ApJ*, 183, 1051
 Gustavsson, K. & Mehlig, B. 2011, *Phys. Rev. E*, 84, 045304(R)
 Gustavsson, K., Mehlig, B., Wilkinson, M. & Uski, V. 2008, *Phys. Rev. Lett.*, 101, 174503
 Gustavsson, K., Meneguz, E., Reeks, M. & Mehlig, B. 2012, *New J. Physics*, 14, 115017
 Guttler, C., Blum, J., Zsom, A., Ormel, C. W., & Dullemond, C. P. 2010, *A&A*, 513, A56
 Helling, Ch., Jardine, M. & Mokler, F. 2011, *ApJ*, 737, 38
 Hogan, R. C., & Cuzzi, J. N. 2001, *Phys. Fluids*, 13, 2938
 Hubbard, A. 2012, 426, 784
 Ishihara, T., Gotoh, T. & Kaneda, Y. 2009, *Annu. Rev. Fluid Mech.*, 41, 165
 Johansen, A., Andersen, A. C., & Brandenburg, A. 2004, *A&A*, 417, 361
 Johansen, A., Klahr, H., & Henning, Th. 2011, *A&A*, 529, A62

- Johansen, A., Oishi, J. S., Low, M.-M. M., et al. 2007, *Nature*, 448, 1022
- Johansen, A. & Youdin, A. N. 2007, *ApJ*, 662, 627
- Johansen, A., Youdin, A., & Mac Low, M.-M. 2009, *ApJ*, 704, L75
- Kolmogorov, A. N. 1962, *J. Fluid. Mech.*, 13, 82
- Kruis, F. E. & Kusters, K. A. 1997, *Chem. Eng. Comm.*, 158, 201
- Lee, A. T., Chiang, E., Asay-Davis, X., & Barranco, J. 2010, *ApJ*, 725, 1938
- Lundgren, T. S. 1981, *J. Fluid Mech.* 111, 27
- Markiewicz, W. J., Mizuno, H. & Voelk, H. J. 1991, *A&A*, 242, 286
- Maxey, M. R. 1987, *J. Fluid Mech.*, 174, 441
- Monin, A. S. & Yaglom, A. M. 1975, *Statistical Fluid Mechanics: Mechanics of Turbulence*, vol. 2. MIT press.
- Ormel, C. W., & Cuzzi, J. N. 2007, *A&A*, 466, 413
- Ormel, C. W., Paszun, D., Dominik, C., & Tielens, A. G. G. M. 2009, *A&A*, 502, 845
- Padoan, P., Jimenez, R., Nordlund, A. & Boldyrev, S., 2004, *Phys. Rev. Lett.* 92, 191102
- Pan, L. & Padoan, P. 2010, *J. of Fluid Mech.*, 661, 73 (PP10)
- Pan, L., Padoan, P., Scalo, J., Kritsuk, A. G., & Norman, M. L. 2011, *ApJ*, 740, 21
- Pan, L. & Scannapieco, E. 2011, *Phys. Rev. E*, 2011, 83, 045302(R)
- Pinsky, M. B. & Khain, A. P. 1997, *J. Aerosol Sci.* 28, 1177
- Pruppacher, H. R., & Klett, J. D. 1997, *Microphysics of Clouds and Precipitation*(Dordrecht: Kluwer)
- Rossow, W.B., 1978, *Icarus*, 36, 1
- Saffman, P. G. & Turner, J. S. 1956 *J. Fluid Mech.*, 1, 16
- Sawford, B. L. 1991, *Phys. Fluids*, 3, 1577
- Sawford, B. L. & Hackl, J. F. 2008, *Phys. Fluids*, 20, 065111
- Shaw, R. A. 2003, *Annu. Rev. Fluid Mech.*, 35, 183
- Squires, K. D., & Eaton, J. K. 1991, *Phys. Fluids*, 3, 1169
- Sundaram, S., & Collins, L. R. 1997, *J. of Fluid Mech.*, 335, 75
- Volk, H. J., Jones, F. C., Morfill, G. E. & Roeser, S. 1980, *A&A*, 85, 316–325
- Wang, L.-P., Wexler, A. S., & Zhou, Y. 1998, *Phys. Fluids*, 10, 2467
- Wang, L.-P., Wexler, A. S., & Zhou, Y. 2000, *J. of Fluid Mech.*, 415, 117
- Weidenschilling, S. J. 1980, *Icarus*, 44, 172
- Wilkinson, M. & Mehlig, B. 2005, *Europhys. Lett.*, 71, 186
- Wilkinson, M. Mehlig, B., & Bezuglyy, V. 2006, *Phys. Rev. Lett.*, 97, 048501
- Williams, J. J. E. & Crane, R. I. 1983, *Int. J. Multiphase Flow*, 9, 421
- Yeung, P. K., Pope, S. B. & Sawford, B. L. 2006, *J. Turbulence*, 7, 58
- Youdin, A. N. 2011, *ApJ*, 742, 38
- Yuu, S. 1984, *AIChE J.*, 30, 802
- Zaichik, L. I., & Alipchenkov, V. M. 2003, *Phys. Fluids*, 15, 1776
- Zaichik, L. I. & Alipchenkov, V. M. 2009, *New J. Phys.*, 11, 103018
- Zaichik, L. I., Simonin, O. & Alipchenkov, V. M. 2003, *Phys. Fluids*, 15, 2995
- Zaichik, L. I., Simonin, O. & Alipchenkov, V. M. 2006, *Phys. Fluids*, 18, 035110
- Zhou, Y., Wexler, A. S., & Wang, L.-P. 2001, *J. Fluid Mech.*, 433, 77
- Zsom, A., Ormel, C. W., Dullemond, C. P., & Henning, T. 2011, *A&A*, 534, A73
- Zsom, A., Ormel, C. W., Güttler, C., Blum, J., & Dullemond, C. P. 2010, *A&A*, 513, A57